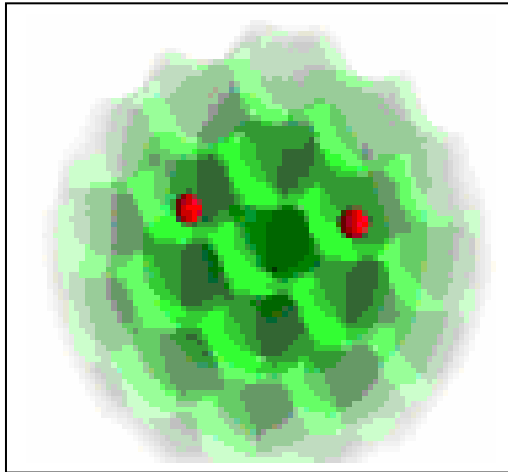PhD Thesis

Ultracold atoms in optical lattices with long-range interactions and periodic driving.

Olivier TIELEMAN

Advisor: Prof. Maciej LEWENSTEIN
Co-advisor: Dr. André ECKARDT

Friday March 8, 2013.
ICFO Auditorium

Contents

Chapter 1

Introduction

The research presented in this thesis is theoretical in nature, and focusses on topics from the field of ultracold atoms in optical lattices (see Refs. [1] and [2] for recent overviews). More specifically, it focusses on long-range interactions in such systems, where long-range is taken to mean 'beyond nearest neighbour (NN)', and periodic driving of the lattice potential. An overview of the research is presented in section 1.4. Below, we present a discussion of the context against which the following chapters must be seen.

1.1   Ultracold atomic gases in optical lattices

Soon after the achievement of Bose-Einstein condensation (BEC) in 1995 (see Refs. [3, 4, 5]) and the experimental realisation of a degenerate Fermi gas a few years later (Ref. [6]), the field of ultracold atomic gases in optical lattices began to emerge. Optical lattices are traditionally generated by counterpropagating laser beams, whose interference pattern is experienced as a conservative potential by the atoms, via the AC-Stark shift (a well-written introductory treatment can be found in *e.g.* Ref. [7]). By appropriately choosing the set-up and intensities of the laser beams, many different geometries, dimensionalities, and tunnelling rates between nearby lattice sites can be achieved. The most common lattices are one-dimensional,

square, or cubic (see *e.g.* Ref. [8]), but recent advances have led to the re-alisation of hexagonal [9], triangular [10], and kagomé [11] geometries. A very promising new technique makes use of a split laser beam, where a so-called holographic mask is imprinted on one of the two split beams before they are brought back together; the interference between the imprinted and unaltered beams can then generate almost arbitrary potentials [12].

In most theoretical descriptions, the atoms are treated as simple, struc-tureless quantum particles (see section 2.1 for more details on the type of theoretical description that will be relevant for this thesis). That does not mean that their internal structure is irrelevant: there are many proposals and experimental studies that rely to a lesser or greater extent on the num-ber and energetic separation of the internal states available to the atoms. However, once a species of atoms has successfully been loaded into a lattice, the role that is given to the internal structure is to a large extent a choice of the experimentor, and it is possible to create a set-up that allows us to ignore it altogether. In each of the projects presented below, only one species of atoms is considered, described by a single quantum field.

There are many suggested applications of this type of system, two prominent examples being quantum simulation (see Ref. [2] for a recent introduction and overview) and quantum information processing. The in-terest of the field can be said to derive from being at the forefront of the effort to push the limit of human control over quantum behaviour. The research presented below is of the exploratory type: we investigate var-ious new set-ups in order to find out which types of collective quantum behaviour could be observed.

In the context of quantum simulation, one could, in principle, consider the experimental set-ups that would realise the models discussed in this thesis as quantum simulators of those models. However, since the results in this thesis were obtained by means of classical computational methods, such simulations would not add much to our understanding. Instead, the results presented here can be used to confirm that within the treated parameter regime, the set-ups discussed are indeed described by the models we wish to test. This confirmation then plays a role in justifying the use of the same set-ups, with other parameter values, as quantum simulators of those

models in parameter regimes where classical computations are beyond our reach.

1.2 Periodically driven optical lattices

The question of what happens when an optical lattice is shaken periodically has received much attention in recent years; see [13] for a recent introduction. In the parameter range on which we focus here, an effective time-independent theory can be derived, which describes the system as if the atoms were placed in an unshaken lattice, with different parameters than the shaken one. Hence, periodically shaken lattices turn out to provide a fascinating manipulation technique for ultracold atomic gases. Specifically, the inter-site tunnelling processes can be modified extensively, *e.g.* generating kinetic frustration [14] or mimicking gauge fields [15, 16].

In order to obtain the effective theory mentioned above, the periodically driven theory needs to have a separation of energy scales. If the Hamiltonian is composed of two parts that depend on time with very different frequencies, an effective Hamiltonian may be obtained by integrating out the quickly oscillating part. This argument only applies if the other energy scales in the slowly varying part of the Hamiltonian also correspond to frequencies much lower than the ones being integrated out. A well-written, if condensed, discussion is offered in Ref. [17], which we partially reproduce in section 2.2. Another calculational route to the same result is presented in Ref. [18].

The term 'shaken lattice' should sometimes be taken quite literally: the retroreflecting mirrors that make up the lattice can be moved periodically in space, i.e. shaken. Alternatively, a frequency difference between the two counterpropagating laser beams can be induced by means of acousto-optical modulators (AOMs), as was done in the pioneering study presented in Ref. [19]. The lattice potential is then no longer static, but becomes time-dependent: $V(\mathbf{r}) \to V(\mathbf{r}, t)$.

In the effective theory, density-density interaction terms are not renormalised. However, the tunnelling term can be renormalised in many differ-

ent ways: the parameter J from Eq. (2.1) is replaced by $J_{\text{eff}} = JG(A, \Omega)$, where G is a function of the driving amplitude A and frequency Ω, usually a Bessel function of $maA\Omega/\hbar$ where m is the mass of the tunnelling atom and a the lattice spacing.

1.2.1   Context: some selected references

Periodic driving of quantum systems has been studied since the 1960s [20, 21]. The idea to apply it to an optical lattice containing an ultracold atomic gas was first suggested in 1997 by Drese and Holthaus (Ref. [22]), and extended to the regime of interacting particles in 2005 by Eckardt *et al.* in Ref. [17]. By tuning J_{eff} to zero, the paradigmatic superfluid-Mott insulator phase transition (cf. Refs. [23, 24, 8]) was predicted to occur (Ref. [17]). The first experimental observation came in 2007 in the pioneering work of Lignier *et al.* (Ref. [19]), which found that certain values of the shaking parameters led to a complete disappearance of the otherwise robust phase coherent lattice BEC. Since then, numerous advances have been made in both the theoretical and the expermental domain.

The one-dimensional set-up used in Ref. [19] has been generalised to a cubic lattice (Ref. [25]), also finding the superfluid-Mott insulator transition. A wider variety of time-reversal symmetric driving functions has been explored theoretically and tested experimentally for the one-dimensional system (see Ref. [26]). The Bessel function that multiplies the static hopping matrix element is specific to sinusoidal driving. The driving has also been shown to overcome the tunnelling inhibition induced by a lattice tilt (Ref. [27]).

Since square and cubic lattices are separable (*i.e.* the lattice potential $V(x, y, z)$ can be decomposed into $V_x(x) + V_y(y) + V_z(z)$, in the cubic case), the experiments reported in Ref. [25] can be seen as many simultaneous and coupled repetitions of the 1D version. More recently, other lattice geometries and potential functions have been proposed in Refs. [14] (triangular lattice) and [28] (square lattice with non-separable potential), where the lattice potential is not separable and the system is truly two-dimensional. In these cases, it turns out that the minimum of the single-particle spec-

trum can be moved continuously from the center to the edge of the Brillouin zone, enabling the creation of BECs with macroscopic wavefunctions featuring arbitrary quasimomenta.

Different types of driving are also under consideration. One interesting example is the 'microrotor' scheme proposed by Hemmerich *et al.*, which is predicted to lead to an artificial staggered Abelian gauge field in a square lattice (see Refs. [15, 29, 30]). The driving is not the same for every site: it moves the potential minima around the elementary plaquettes of the static lattice. The most recent development is the generation of a staggered gauge field in a triangular lattice, with a uniform driving function. Struck *et al.* used uniform periodic driving functions that break time-reversal symmetry (see Ref. [31]). Both approaches render the hopping matrix element J complex, corresponding to broken time-reversal symmetry. When engineered appropriately, such time-reversal symmetry broken Hamiltonians can be used to mimic the effects of a magnetic field. Another recent proposal combined superlattices and species-specific potentials with periodic driving, leading to non-Abelian gauge fields, quantum spin Hall physics, and strong artificial gauge fields that vary over many lattice sites [16].

1.3 Long-range interactions

Since atoms are electrically neutral, they do not have the Coulomb repulsion that electrons do. Most of the atomic species being used in cold gas experiments are alkali atoms, such as ^{87}Rb (most frequently), ^{85}Rb, ^{40}K, ^{39}K, ^{23}Na, ^{7}Li, and ^{6}Li, and in fact only have significant short-ranged interactions, which render all terms except the on-site ones neglegible [1]. In the ultracold collision regime, where only the lowest relative angular momentum collisions play a role (for typical atomic masses, this regime is characterised by temperatures below 1 mK), the Van der Waals interactions are effectively determined by the so-called scattering length. The range of these interactions happens to be on the order of the scattering length itself, usually a few nanometers [1]. The lattice spacing itself is usually a few hundred nanometers, justifying the on-site approximation.

While on-site interactions are responsible for many fascinating effects (see *e.g.* [1]), there has been an increasing interest in longer-ranged interactions over the last few years. One promising method to overcome the short range of the interactions between neutral atoms is to use different atomic species, or biatomic molecules, which have significant dipole moments (e.g. Cr has a magnetic dipole moment of $6\mu_B$, compared to roughly $1\mu_B$ for the alkali atoms, where μ_B is the Bohr magneton). The species of dipolar atoms presently under study are mostly bosonic (see Ref. [32] for an overview of bosonic dipolar gases, or Ref. [33] for one focused on optical lattices), although a recent counterexample is given in Ref. [34]. Most investigated heteronuclear molecules are fermionic (see *e.g.* Ref. [35]). Atoms where one or more electrons have a very high principal quantum number, so-called Rydberg atoms, have long decay periods and are characterised by large electric dipole moments [36]. Other ways to obtain significant interactions with longer than on-site range include the use of superexchange effects (see *e.g.* Ref. [37]), mediation by other atomic species present in the lattice (see Refs. [38, 39]), or the study of collective excitations with effective long-range interactions (see Ref. [40]).

Dipolar interactions are often studied in a two-dimensional context, where the orientation of a polarising external field is a control knob for the anisotropy in the long-range interaction within the plane. Three-dimensional set-ups have also been considered, mostly in bulk, but also for on-site interactions, as described in *e.g.* Ref. [41]. Exchange-induced (Ref. [37]) or mediated (Refs. [38, 39]) long-range interactions are completely isotropic, in contrast to their fundamentally anisotropic dipolar counterparts.

Predicted effects of long-range interactions which will be addressed in this thesis include bosonic (chapter 6) and fermionic (chapter 4) density waves, bosonic supersolids (chapter 5), and spontaneous time-reversal symmetry breaking (chapter 4). Other effects, which will not be addressed in this thesis, include interaction-generated hopping terms (see *e.g.* Ref. [41]) and higher-orbital occupation (cf. Ref. [42]).

A density wave is a modulation of the density, which breaks spatial symmetry. In lattices, density waves are defined as phases where the lattice

symmetry is broken by the density. The simplest example of a density wave in a lattice is the so-called checkerboard, which occurs in a square lattice for repulsive nearest-neighbour interactions. More intricate density patterns have been predicted when the full dipolar interaction is taken into account, as described in Ref. [43], since dipolar interactions go beyond nearest-neighbour.

A supersolid is a phase that combines the properties of a superfluid and a density wave (the 'solid' refers to the density modulation of a lattice of atoms or ions). Whether such a phase could occur has been investigated for decades (see *e.g.* Ref. [44]). The question has recently received much attention in the context of ultracold atomic gases in optical lattices.

1.3.1 Context: some selected references

In the domain of long-range interactions, the divide between theoretical and experimental developments is larger than in the case of periodically driven lattices. The reason for this difference is that the effects of periodic driving are primarily visible at single-particle level, whereas the effects of long-range interactions, like any interactions, are much less straightforward to describe theoretically. Furthermore, periodic driving happened to be fairly easy to implement within the already existing experimental set-ups, whereas long-range interactions require either the trapping and cooling of new atomic species (see Refs. [45, 46]), the in-trap or in-lattice creation and cooling of biatomic molecules (Refs. [35, 47] show recent work of two groups on this topic), or working with multi-species mixtures, as described theoretically in Refs. [37, 39].

Experiments on heteronuclear polar fermionic molecules are close to quantum degeneracy (see Ref. [35]). Homonuclear biatomic molecular gases have also been created, both in bulk (Ref. [48]) and in the presence of an optical lattice (Ref. [47]). Gases of dipolar atoms have reached quantum degeneracy, as reported in Refs. [45, 46, 34] and been loaded into optical lattices (see Refs. [49, 50, 51, 52]). The anisotropy of the dipole-dipole interaction has successfully been manipulated [51]. Higher-band effects have been detected and reported in Ref. [50], and the dipolar interaction has been

shown to stabilise an attractive *s*-wave interaction in Refs. [49, 52]. Multi-species atomic gases have been loaded into optical lattices (cf. Refs. [53, 54]).

Theoretical work on the subject of long-range interactions in lattices has largely been focused on the expected density wave, as for example in Refs. [55, 56, 57]. The simplest case has been predicted for a single bosonic (see Ref. [55]) or fermionic (Ref. [58]) species. More intricate density-wave states are predicted for multiple layers connected only by the interlayer attractive interaction (Ref. [59]). Various supersolids have been predicted, for bosons with long-range interactions (see again *e.g.* Ref. [55]), Bose-Fermi mixtures with a nested fermi surface like the ones discussed in Ref. [60], and spin-$\frac{1}{2}$ fermions with long-range interactions (see Refs. [58, 43]). Theoretical calculations on effective long-range interactions in multi-species mixtures can be found in Refs. [38, 37, 39].

1.4   Thesis overview

This thesis is based on four different projects, two of which combine periodic driving with long-range interactions (chapters 4 and 5). The other two investigate new set-ups or effects with either periodic driving (chapter 3) or effective long-range interactions (chapter 6). The general objectives are expand and deepen the existing understanding of periodic driving and long-range interactions in optical lattices, and where possible to predict novel quantum phases or point out hitherto unknown effects occurring in such set-ups.

1.4.1   Shaken lattices and finite-momentum BECs

*Publication: M. di Liberto, O. Tieleman, V. Branchina, and C. Morais Smith, Phys. Rev. A **84**, 013607 (2011), Ref. [28].*

For this project [28], we consider ultracold bosons in a 2D square optical lattice with an external time-dependent sinusoidal force which shakes the lattice [17] along one of the diagonals. Taking hopping terms beyond

nearest-neighbour into account, we find that they are renormalized differently by the shaking, and introduce both anisotropy and frustration into the problem. The competition between the different hopping terms leads to finite-momentum condensates, with a momentum that may be tuned via the strength of the shaking. We calculate the boundaries between the Mott-insulator and the different superfluid phases, and present the time-of-flight images expected to be observed experimentally.

The standard square lattice potential is separable: $V(x, y) = \cos(x/a) + \cos(y/a)$. A consequence of this separability is the absence of first-order diagonal hopping terms. We consider a different, non-separable potential, where the diagonal hopping terms do not vanish. With suitable signs for the various hopping terms, frustration may now be introduced into the system, leading to the appearance of multiple kinetic ground states. In the presence of on-site interactions, the ground state degeneracy of the BEC is reduced to two and time-reversal symmetry breaking is energetically favourable. A similar situation is investigated in Ref. [14], where the naturally frustrated triangular lattice is considered.

The effective Hamiltonian will be calculated using the same Floquet-based formalism as in Refs. [17, 18]. Subsequently, the MI-SF phase boundaries will be calculated in the mean-field decoupling approximation that can be found in *e.g.* [24]. The predicted time-of-flight images are generated based on the assumption of condensation in one quasimomentum state. We use a Gaussian envelope to qualitatively convey the effect of the on-site Wannier function.

1.4.2 Frustrated kinetics, long-range interactions, and spontaneous symmetry breaking

Publication: O. Tieleman, O. Dutta, M. Lewenstein, and A. Eckardt, arXiv:1210.4338, Ref. [61].

Here, we study spontaneous symmetry breaking in a system of kinetically frustrated spin-polarised fermions in a triangular lattice with long-range interactions. We show that frustrated kinetics combined with non-uniform

long-range interactions (*e.g.* dipole-dipole) induce spontaneous breaking of time-reversal symmetry. Furthermore, we investigate spatial symmetry breaking due to the long-range interactions. The symmetry-broken phases that we discuss include a density wave (cf. Ref. [60]), a staggered current phase (cf. Ref. [14, 10]), and a phase where a chirally uniform current pattern appears, confined to an effective kagomé sublattice.

The staggered currents are similar to the ones found in Ref. [14], but the way they come about is different. We find that for weak interactions, a very generic repulsive long-range interaction that falls off with distance leads to an effective attractive interaction in momentum space. At filling factors near 1/4, the Fermi surface exhibits nesting, and a density wave is favoured. Thus, the interaction that leads to spatial symmetry breaking also leads to the appearance of staggered currents, in marked contrast to Ref. [14], where the staggered currents appear due to an interaction term that favours spatial homogeneity.

The phase boundary calculations are performed in a mean-field approximation where the quartic interaction term is decoupled into an effective quadratic term. Exact diagonalisations are performed to support the predictions of the staggered currents and tendency towards density waves.

1.4.3   Long-range interacting bosons in an artificial staggered Abelian gauge-field

Here, we calculate the theoretical mean-field zero-temperature phase diagram of a BEC with dipolar interactions loaded into an optical lattice with a staggered flux. Apart from uniform superfluid, checkerboard supersolid and striped supersolid phases, we identify several supersolid phases with staggered vortices, which can be seen as combinations of supersolid phases found in earlier work on dipolar BECs [56] and a staggered-vortex phase found for bosons in optical lattices with staggered flux [29, 30]. By allowing for different phases and densities on each of the four sites of the elementary

plaquette, more complex phase patterns are found.

The simultaneous presence of a supersolid and a pattern of currents in the system produces interesting novel phases where the current densities break spatial homogeneity in response to the density wave. A consideration from the continuity equation shows that maintaining the a homogeneous current density would lead to charge build-up and depletion, ultimately destroying the density modulation. Since the currents are induced by the hopping terms and are independent of the interactions, they do not change the nature of the density modulation, but instead adapt to it. Numerous metastable states are also identified.

The calculations are performed in the Bogolyubov approximation. A stability analysis based on the Bogolyubov mean-field effective single-particle spectrum is included, leading to the discovery of a phase-separation region. Time-of-flight predictions are calculated based on the Fourier transform of the mean-field BEC wavefunction.

1.4.4 One-dimensional strongly interacting commensurability-driven density wave

*Publication: A. Lazarides, O. Tieleman, and C. Morais Smith, Phys. Rev. A **84**, 023620 (2011), Ref. [40].*

Motivated by recent experiments [62], we investigate quantum phase transitions occurring in a system of strongly interacting ultracold bosons in a 1D optical lattice. Starting from the common field theory including a fourth-order interaction term, we apply Haldane's transformation [63] to arrive at the sine-Gordon model [64]. After discussing the commensurate-incommensurate transition described by the Pokrovsky-Talapov model [65], we focus on the phases appearing at incommensurate filling. There, the state of the system is determined by an effective field theory describing interacting solitons or kinks [66], which correspond to excess particles or holes over commensurate filling. We derive the interaction between the kinks by means of a renormalisation group calculation, finding that it falls off as $1/x^2$. The resulting phase diagram features superfluid, supersolid and solid

(kink-lattice) phases. Supersolids generally appear in theoretical studies of systems with long-range interactions; our results break this paradigm and show that they may also emerge in models including only short-range (contact) interactions, provided that quantum fluctuations are properly taken into account.

Chapter 2

Ultracold atoms in optical lattices: some technical aspects

In this chapter, we present some more technical results that are relevant for the remainder of the thesis. Section 2.1 introduces the family of Hubbard models, section 2.2 briefly reviews Floquet's theorem for periodic systems, and section 2.3 offers some details on dipolar interactions.

2.1 Hubbard model

Most theoretical many-body studies of ultracold atomic gases in deep optical lattices ('deep' usually means $V_0 \geq 5E_r$; see below) correspond to some variation of the Hubbard model. It describes quantum particles, either bosons or fermions, in a deep lattice. The traditional form features NN hopping and on-site interactions. For bosons, the model traditionally describes one species (see e.g. Refs. [23, 67]):

$$H = -J \sum_{\langle \mathbf{r},\mathbf{r}' \rangle} a_{\mathbf{r}}^{\dagger} a_{\mathbf{r}'} + \frac{U}{2} \sum_{\mathbf{r}} n_{\mathbf{r}}(n_{\mathbf{r}} - 1) - \mu \sum_{\mathbf{r}} n_{\mathbf{r}}, \qquad (2.1)$$

where $\langle,\rangle$ indicates that the sum runs over all oriented pairs of nearest neighbours. The vectors $\mathbf{r}$ and $\mathbf{r}'$ correspond to the lattice sites. The parameters J and U are real and positive in the standard form of the model. The quantity J is usually called the hopping or tunnelling matrix element, since it corresponds to the process of an atom tunnelling from one lattice site to another. The interaction energy U represents the cost due to multiply occupied sites: for every pair of atoms found on a single site, the total energy of the state is increased by U. The chemical potential μ, finally, is often introduced for mathemtical convenience, in order to perform the calculations in the more workable grand canonical ensemble. Note, however, that in experiments, the particle number is fixed, rather than the chemical potential. The operators $a_{\mathbf{r}}^{(\dagger)}$ have the canonical commutation relation $[a_{\mathbf{r}}, a_{\mathbf{r}'}^{\dagger}] = \delta_{\mathbf{r},\mathbf{r}'}$. For fermions, on-site interactions between atoms of the same species are forbidden by the Pauli exclusion principle under the assumption that only one quantum state per site exists (the single-band approximation; see below). Hence, the model usually describes two spin species, labelled (pseudo)spin up and down:

$$H = -J \sum_{\langle \mathbf{r},\mathbf{r}' \rangle} \sum_{\sigma=\uparrow,\downarrow} a_{\sigma,\mathbf{r}}^{\dagger} a_{\sigma,\mathbf{r}'} + U \sum_{\mathbf{r}} n_{\uparrow,\mathbf{r}} n_{\downarrow,\mathbf{r}} - \mu \sum_{\mathbf{r};\sigma=\uparrow,\downarrow} n_{\sigma,\mathbf{r}}. \qquad (2.2)$$

Here, J is still generally real and positive, but U may also be negative without depriving the model of a stable ground state, due to the Pauli exlcusion principle. The operators $a_{\mathbf{r}}^{(\dagger)}$ obey the anticommutation relation $\{a_{\mathbf{r}}, a_{\mathbf{r}'}^{\dagger}\} = \delta_{\mathbf{r},\mathbf{r}'}$.

The Fermi-Hubbard model has been widely studied in solid-state contexts, such as high-T_C superconductivity, where it is considered a candidate theoretical description of a number of as yet unexplained phenomena [68]. Many variations of these models have been studied, and most of the work presented in this thesis is based on one of the two, with some modified and some extra terms. The Bose-Hubbard model presented in Eq. (2.1) exhibits the paradigmatic Mott insulator-superfluid (MI-SF) phase transition at a critical value for the ratio U/J. This transition, which is briefly discussed at the end of this section, was first investigated in Ref. [23], further studied theoretically in e.g. Refs. [67, 24], and observed experimentally

in Refs. [8, 69, 70]. The Hubbard model is characterised by a number of parameters: the dimensionless interaction strength given by the ratio U/J, the dimensionality, the lattice geometry, and the number of different particle types present in the lattice (e.g. the pseudospin up/down states in Eq. (2.2)). As will be discussed below, all of these parameters are tunable in experimental setups consisting of deep optical lattices with ultracold atoms, many of which it describes very well, thus constituting a very rich playground for both theoretical and experimental studies. A limiting factor is the temperature: at the moment, the temperatures required for simulating the candidate mechanisms for high-T_c superconductors have not yet been achieved.

Experimental control over model parameters

As mentioned above, a number of different parameters that characterise the Hubbard model can be controlled in experimental set-ups consisting of ultracold atoms in optical lattices. There are two major aspects that each allow control over a set of parameters: the gas, and the lattice. The preparation of the gas allows for different particle types to be loaded into the lattice, which may perceive the potential differently (see *e.g.* the spin-dependent hexagonal lattice presented in Ref. [9]), as well as mixtures. The optical potential, which is determined by the lasers, controls the dimensionality of the lattice, the geometry, and potential spin-dependent properties. The tunnelling rate and interaction strength depend on both the atomic species being used and the potential. The lattice constant is determined by the wavelength of the laser being used, given by $a = \lambda/2$, and typically takes values around 0.5μm. The tunnelling rate depends on the potential depth, which is proportional to the laser intensity (see *e.g.* Ref. [7] for a detailed derivation of how the potential arises due to the AC-Stark shift). Typical potential depths are up to a few tens of recoil energies, where the recoil energy is given by $E_r = \hbar^2 k^2/2m$, with $k = 2\pi/\lambda$ being the laser wavevector.

2.1.1   Derivation

The Hubbard model is intuitively easy to accept as a description of a gas of interacting atoms in a lattice. It also happens to be easy to derive from a more general interacting field theory with a periodic external potential,

$$
\begin{aligned}
H = \int \mathrm{d}\mathbf{x} &\bigg\{ \psi^\dagger(\mathbf{x})\bigg[-\frac{\nabla^2}{2m} + V(\mathbf{x}) \bigg]\psi(\mathbf{x}) \\
&+ \frac{1}{2}\int \mathrm{d}\mathbf{x}' U(\mathbf{x}-\mathbf{x}')\psi^\dagger(\mathbf{x})\psi^\dagger(\mathbf{x}')\psi(\mathbf{x}')\psi(\mathbf{x}) \bigg\},
\end{aligned}
\tag{2.3}
$$

where $V(\mathbf{x}) = V(\mathbf{x}+\mathbf{e}_j)$ such that $\mathbf{e}_j$ represent the elementary lattice vectors, and $U(\mathbf{x})$ represents the interaction energy for two particles separated by a distance $\mathbf{x}$. To see this derivation, we start from the Bloch waves, which are eigenfunctions of the periodic potential given by

$$
f_{n,\mathbf{k}}(\mathbf{x}) = e^{i\mathbf{k}\cdot\mathbf{r}}u_{n,\mathbf{k}}(\mathbf{x})
\tag{2.4}
$$

such that $u_{n,\mathbf{k}}(\mathbf{x})$ has the periodicity of the lattice: $u_{n,\mathbf{k}}(\mathbf{x}+\mathbf{e}_j) = u_{n,\mathbf{k}}(\mathbf{x})$. The index n labels the different bands of the single-particle spectrum to which the Bloch functions belong, and $\mathbf{k}$ is the quasimomentum. The Bloch functions may now be written in terms of the Wannier functions $w_{n,\mathbf{r}}(\mathbf{x})$ by means of a Fourier transform:

$$
f_{n,\mathbf{k}}(\mathbf{x}) = \sum_{\mathbf{r}} w_{n,\mathbf{r}}(\mathbf{x})e^{-i\mathbf{r}\cdot\mathbf{k}}.
\tag{2.5}
$$

For a detailed discussion of 1D Wannier functions, see Ref. [71]. Note that for separable potentials, *i.e.* of the form $V(\mathbf{x}) = V(x) + V(y) + V(z)$, the different dimensions decouple in the single-particle Hamiltonian, and therefore the 2D- and 3D-problems are also determined by the 1D results. Further, remark that the phases of the Bloch functions can be chosen freely, and that a suitable choice of phases leads to exponentially localised Wannier functions in the 1D case [71]. Expanding the field operator $\psi(\mathbf{x})$ in terms of these localised Wannier functions, one obtains a sum over lattice sites.

Inserting

$$\psi(\mathbf{x}) = \sum_{\mathbf{r},n} a_{\mathbf{r},n} w_n(\mathbf{r} - \mathbf{x}), \tag{2.6}$$

(again, $\mathbf{r}$ runs over all lattice sites) into the field theory's Hamiltonian, and restricting the on-site sum over the Wannier functions to the lowest-energy orbital w_0 (this approximation is justified when the excitation energy to the second band is much higher than the energy scales that govern the lowest band), yields

$$H = -\sum_{\mathbf{r},\mathbf{r}'} J_{\mathbf{r}-\mathbf{r}'} a_{\mathbf{r}}^\dagger a_{\mathbf{r}'} + \sum_{\mathbf{r},\mathbf{r}',\mathbf{r}'',\mathbf{r}'''} U_{\mathbf{r},\mathbf{r}',\mathbf{r}'',\mathbf{r}'''} a_{\mathbf{r}}^\dagger a_{\mathbf{r}'}^\dagger a_{\mathbf{r}''} a_{\mathbf{r}'''},$$

having defined

$$J_{\mathbf{r}-\mathbf{r}'} = -\int d\mathbf{x}\, w^*(\mathbf{r} - \mathbf{x}) \left[-\frac{\nabla^2}{2m} + V(\mathbf{x}) \right] w(\mathbf{r}' - \mathbf{x}) \tag{2.7}$$

$$U_{\mathbf{r},\mathbf{r}',\mathbf{r}'',\mathbf{r}'''} = \int d\mathbf{x}\, d\mathbf{x}'\, U(\mathbf{x} - \mathbf{x}') w^*(\mathbf{r} - \mathbf{x}) w^*(\mathbf{r}' - \mathbf{x}') w(\mathbf{r}'' - \mathbf{x}') w(\mathbf{r}''' - \mathbf{x}),$$

where the lowest-band index $_0$ has been dropped. In sufficiently deep potentials (usually about $5E_r$ or more), the Wannier functions are highly localised, and it is justified to consider only nearest-neighbour tunnelling terms. In certain cases, the nearest-neighbour tunnelling terms vanish, or are very small, in which case longer-distance tunnelling also has to be taken into account. As discussed in the previous chapter, the interactions are often very short-ranged, in which case one may safely approximate them to be limited to on-site processes. With these two approximations, the Hubbard model emerges:

$$H = -\sum_{\mathbf{r},\mathbf{r}'} J_{\mathbf{r}-\mathbf{r}'} a_{\mathbf{r}}^\dagger a_{\mathbf{r}'} \delta_{\mathbf{r},\mathbf{r}'+\mathbf{e}_j} + \sum_{\mathbf{r},\mathbf{r}',\mathbf{r}'',\mathbf{r}'''} U_{\mathbf{r},\mathbf{r}',\mathbf{r}'',\mathbf{r}'''} a_{\mathbf{r}}^\dagger a_{\mathbf{r}'}^\dagger a_{\mathbf{r}''} a_{\mathbf{r}'''} \delta_{\mathbf{r},\mathbf{r}'} \delta_{\mathbf{r},\mathbf{r}''} \delta_{\mathbf{r},\mathbf{r}'''}$$

$$= -\sum_{\mathbf{r},j,\delta=\pm 1} J_j a_{\mathbf{r}}^\dagger a_{\mathbf{r}+\delta \mathbf{e}_j} + \sum_{\mathbf{r}} \frac{U}{2} a_{\mathbf{r}}^\dagger a_{\mathbf{r}}^\dagger a_{\mathbf{r}} a_{\mathbf{r}}, \tag{2.8}$$

where $U/2 = U_{\mathbf{r},\mathbf{r},\mathbf{r},\mathbf{r}}$. Adding the chemical potential term $-\mu \sum_{\mathbf{r}} a_{\mathbf{r}}^{\dagger} a_{\mathbf{r}}$, we obtain Eq. (2.1). A similar derivation for spin-$\frac{1}{2}$ fermions leads to Eq. (2.2). Note that we have neglected all longer-ranged interaction terms, which is well justified when describing typical experiments with *e.g.* ^{87}Rb. In this thesis, however, we will often encounter cases where the interactions are not short-ranged, and nearest-neighbour or longer-distance terms also play a role.

2.1.2   Mott insulator - superfluid phase transition

The Bose-Hubbard model features the paradigmatic Mott insulator - superfluid transition, studied theoretically in Refs. [23, 67] and first observed experimentally in Ref. [8]. Here, we give a brief description.

Treating the chemical potential μ as a knob to tune the particle number, the Hubbard model has two energy scales, J and U. Hence, it is their ratio, J/U, that determines the state of the system. Intuitively, taking U to zero, we can see that the particles gain energy by delocalising: that maximises the expectation value $\langle \mathrm{GS}|a_{\mathbf{r}}^{\dagger} a_{\mathbf{r}+\mathbf{e}_j}|\mathrm{GS}\rangle$, and thus minimises the expectation value of the Hamiltonian. The resulting state, where every particle is in the zero-momentum state, corresponds to a BEC. Going to the other extreme and taking J to zero, it is easy to see that for integer filling fractions, all particles will localise in such a way that the filling factor is uniform; this is the Mott insulator state.

At some intermediate value of U/J, a transition will occur between the two states. In the Mott insulator, a finite tunnelling term will create virtual particle-hole pairs. When the tunnelling term becomes strong enough, these particle-hole pairs will no longer be virtual, but instead become part of the ground state: the atoms will start to delocalise. Alternatively, coming from the superfluid side, a finite interaction term leads to condensate depletion. When the interaction reaches a critical strength, the condensate depletion reaches unity, and the atoms start to localise. Fig. 2.1 shows the phase boundary between the superfluid and Mott insulating states.
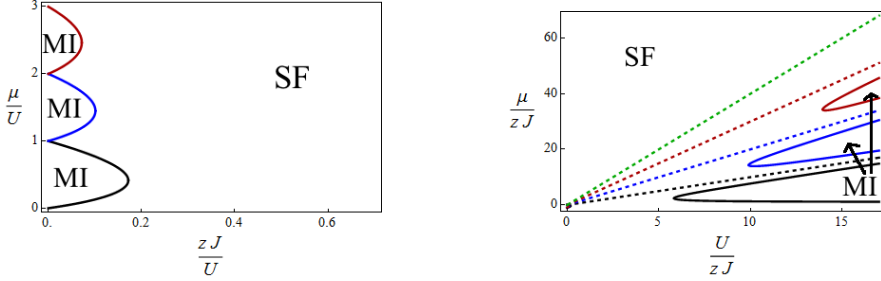
Figure 2.1: The MI-SF phase diagram. Left: for low values of zJ/U (z being the coordination number), the Mott insulating phase is favoured. Higher filling factors reduce the critical hopping strength. Right: the same phase diagram, in different variables. The dashed lines represent constant μ/U ratios, corresponding to the points where the lobes touch the y-axis in the left panel.

2.2 Floquet's theorem: periodic systems

Floquet's theorem

To understand the behaviour of driven quantum systems, we have to turn to Floquet's theorem. Although it was derived long before the advent of quantum mechanics [72], it is relevant for a number of different quantum phenomena. One example is the famous Bloch's theorem, which results from applying Floquet's theorem to spatially periodic systems. Here, we will apply it to temporally periodic systems. The essence is simple: A spatially periodic Hamiltonian leads to eigenstates consisting of a plane wave multiplied by a spatially periodic function, called Bloch waves. Similarly, a temporally periodic Hamiltonian leads to temporally periodic eigenstates, which we will call Floquet states. The theorem, when applied to temporally periodic quantum mechanical systems (as described in *e.g.* Refs. [20, 21, 73]), is as follows: With a Hamiltonian $H(t)$ obeying $H(t + T) = H(t)$ for some

period T, the Schrödinger equation

$$[H(t) - i\hbar\partial_t]\Psi(t) = 0 \tag{2.9}$$

has solutions of the form

$$\Psi_\alpha(t) = \Phi_\alpha(t)e^{-i\epsilon_\alpha t/\hbar}, \tag{2.10}$$

such that $\Phi_\alpha(t+T) = \Phi_\alpha(t)$. The energy ϵ_α is real-valued, and constitutes the analogue of the quasimomentum characterising a Bloch state. Hence, it is called quasienergy. Its eigenvalue equation is given by

$$\underbrace{[H(t) - i\hbar\partial_t]}_{\mathcal{H}(t)}\Phi_\alpha(t) = \epsilon_\alpha\Phi_\alpha(t). \tag{2.11}$$

Note that due to the periodicity in time, there is also a periodicity in energy: if $\Phi_\alpha(t)e^{-i\epsilon_\alpha t/\hbar}$ is a T-periodic eigenfunction of the Floquet Hamiltonian $\mathcal{H}$, so is $\Phi_\alpha(t)e^{-i(\epsilon_\alpha + 2\pi n\hbar/T)t/\hbar}$. (The name 'Floquet Hamiltonian' refers to the fact that the operator $\mathcal{H}$ plays the same role in the quasienergy eigenvalue equation as the normal Hamiltonian does in the time-independent Schrödinger equation.) This periodicity in energy implies that there is a Brillouin-zone-like structure in the energy quantum numbers.

Such problems are easier to handle when described in an extended Hilbert space, which is composed of a Fock space $\mathcal{R}$ and the space of square integrable T-periodic functions $\mathcal{T}$. Any orthonormal basis of states in $\mathcal{R}$, tensor multiplied with any orthonormal basis in $\mathcal{T}$, together form an orthonormal basis in the extended Hilbert space. The scalar product on such a space will be denoted by $\langle\langle\cdot|\cdot\rangle\rangle$, given by

$$\langle\langle\cdot|\cdot\rangle\rangle = \frac{1}{T}\int_0^T dt\,\langle\cdot|\cdot\rangle\,, \tag{2.12}$$

where $\langle\cdot|\cdot\rangle$ denotes the conventional scalar product in $\mathcal{R}$.

2.2.1 Effective Hamiltonian

In deriving the effective Hamiltonian we will be working with, we follow Refs. [17, 18]. Now consider a Hamiltonian $H = H_0 + H_d$ consisting of two parts, an undriven (or weakly driven) part, H_0, and a (strongly) driven part, H_d. Assuming that the driving is fast enough, i.e. much faster than the other timescales in the experiment, the ground state wavefunction will not be time-dependent, but instead correspond to some effective Hamiltonian, where the fast driving has been integrated out.

To obtain the effective Hamiltonian, we start from an orthonormal, stationary basis of the Fock space $\mathcal{R}$. For any time-dependent T-periodic Hermitean operator F, one can define an orthonormal basis of T-periodic states that span all Brillouin zones:

$$|n(t), m\rangle\rangle = e^{-iF + im\Omega t} |n\rangle. \tag{2.13}$$

The matrix elements of the Floquet Hamiltonian $\mathcal{H}$ (see Eq. (2.11)) in the basis $|n(t), m\rangle$ are given by

$$\langle\langle n(t), m| \mathcal{H} |n'(t), m'\rangle\rangle = \frac{1}{T} \int_0^T dt \, \langle n| e^{iF - im\Omega t} \mathcal{H} e^{-iF + im'\Omega t} |n'\rangle$$

$$= \frac{\delta_{m,m'}}{T} \langle n| \int_0^T dt e^{iF} (\mathcal{H} + m\hbar\Omega) e^{-iF} |n'\rangle \quad (2.14)$$

$$+ \frac{1 - \delta_{m,m'}}{T} \int_0^T dt e^{i(m'-m)\Omega t} \langle n| e^{iF} \mathcal{H} e^{-iF} |n'\rangle.$$

Here, we have divided the Hamiltonian into blocks characterised by a combination (m, m'), with special attention for the diagonal blocks. Note that the diagonal blocks are separated from each other by steps of $\hbar\Omega$. This implies that if the elements of the off-diagonal blocks are much smaller than $\hbar\Omega$, we can, in a first perturbative approximation, neglect them, and focus on the $m' = m$ blocks [17]. Doing so allows us to define an effective Hamiltonian:

$$\langle\langle n(t), m| \mathcal{H} |n'(t), m'\rangle\rangle \approx \delta_{m,m'} \langle n| \langle e^{iF} \mathcal{H} e^{-iF} \rangle_T |n'\rangle + m\hbar\Omega\delta_{m,m'}\delta_{n,n'}. \tag{2.15}$$

As long as the energies of the different Brillouin zones do not mix, *i.e.* if the Brillouin zone size $\hbar\Omega$ is much larger than the energy scales present in $\left\langle e^{iF}\mathcal{H}e^{-iF}\right\rangle_T$, we can approximate the spectrum of the time-dependent Hamiltonian in the first Brillouin zone by that of the time-averaged effective Hamiltonian, which is then defined by

$$H_{\text{eff}} = \frac{1}{T}\int_0^T dt\, e^{iF}[H(t) - i\hbar\partial_t]e^{-iF}. \tag{2.16}$$

In the above derivation, the operator F has never been defined. The reason is that in principle, any time-dependent T-periodic operator will do, keeping in mind that the set of basis states in which the effective Hamiltonian is formulated depends on which operator F one uses. The shape of the effective Hamiltonian itself therefore also changes with F. A natural choice for this operator is the primitive of the driven part of the original Hamiltonian: this choice implies that we work with a basis of states in the extended Hilbert space whose time-dependence is generated by H_d. It should be noted that the derivation presented here glosses over a number of very subtle and interesting effects, which we will not touch upon in this thesis. Interested readers are referred to [74].

2.2.2 Periodically driven lattice potentials

Below, the basic steps are executed to obtain the form of the many-particle time-dependent Hamiltonian $H(t)$ to be used for deriving H_{ff} for ultracold atoms in shaken optical lattices. The driving terms used in this thesis will always be superpositions of same-frequency sinusoidal functions along all axes, but the phase and amplitude differences allow for various paths to be traced. Here, we will simply use some function $\mathbf{s}(t)$ such that $\mathbf{s}(t+T) = \mathbf{s}(t)$:

$$H = \frac{|\mathbf{p}|^2}{2m} + V[\mathbf{r} + \mathbf{s}(t)], \tag{2.17}$$

Now, since we are assuming a deep lattice, it makes sense to perform a canonical transformation to the comoving frame of reference:

$$
\begin{aligned}
\mathbf{r}' &= \mathbf{r} + \mathbf{s}(t) \\
\mathbf{p}' &= \mathbf{p} + m\partial_t\mathbf{s}(t) \\
G &= [\mathbf{r} + \mathbf{s}(t)] \cdot [\mathbf{p}' - m\partial_t\mathbf{s}(t)],
\end{aligned}
\tag{2.18}
$$

where G generates the transformation. Hence, the Hamiltonian in the new frame is given by

$$
\begin{aligned}
H' &= \frac{|\mathbf{p}' - m\partial_t\mathbf{s}|^2}{2m} + V(\mathbf{r}') - m\partial_t^2\mathbf{s}\cdot\mathbf{r}' + (\mathbf{p}' - m\partial_t\mathbf{s})\cdot\partial_t\mathbf{s} \\
&= \frac{|\mathbf{p}'|^2}{2m} + V(\mathbf{r}') - m\partial_t^2\mathbf{s}\cdot\mathbf{r}' + \text{const.}
\end{aligned}
\tag{2.19}
$$

Having obtained this comoving frame-Hamiltonian, we will drop the dashes and work with the comoving version from now on. Note the intertial force term that has appeared: this will take the role of H_d in the derivation of the effective Hamiltonian.

Second quantisation

We use the Wannier basis corresponding to the potential $V(\mathbf{r})$. The form of the static part of the Hamiltonian in that basis is well-known:

$$
H_s = -\sum_{i,j} J_{ij} a_i^\dagger a_j,
\tag{2.20}
$$

where

$$
J_{ij} = -\int d\mathbf{r}\, w^*(\mathbf{r} - \mathbf{R}_i)\left[\frac{-\hbar^2\nabla^2}{2m} + V(\mathbf{r})\right] w(\mathbf{r} - \mathbf{R}_j).
\tag{2.21}
$$

The operator $\mathbf{r}$, expressed in terms of $a^\dagger$ and a, is given by

$$
\sum_{i,j} a_i^\dagger a_j \int d\mathbf{r}\, w^*(\mathbf{r} - \mathbf{R}_i)\,\mathbf{r}\, w(\mathbf{r} - \mathbf{R}_j).
\tag{2.22}
$$

For $i = j$, the integral yields $\mathbf{R}_i a_i^\dagger a_i$, since the Wannier function peaks at the origin:

$$
\begin{aligned}
\int d\mathbf{r}\, |w(\mathbf{r} - \mathbf{R})|^2 \mathbf{r} &= \int d\mathbf{r}\, |w(\mathbf{r})|^2 (\mathbf{r} + \mathbf{R}) \\
&= \mathbf{R} \int d\mathbf{r}\, |w(\mathbf{r} - \mathbf{R})|^2 + \int d\mathbf{r}\, |w(\mathbf{r})|^2 \mathbf{r} = \mathbf{R},
\end{aligned}
\tag{2.23}
$$

since the Wannier function can be chosen to be even, and its square is normalised to unity. For $i \neq j$, we can shift the integration variable by $(\mathbf{R}_i - \mathbf{R}_j)/2$ and obtain

$$
\int d\mathbf{r}\, w^*[\mathbf{r} - (\mathbf{R}_i - \mathbf{R}_j)/2]\, \mathbf{r}\, w[\mathbf{r} + (\mathbf{R}_i - \mathbf{R}_j)/2]. \tag{2.24}
$$

This integral vanishes due to symmetry arguments. Hence, we conclude that the effective single-particle Hamiltonian reads

$$
H = -J \sum_{i,j} a_i^\dagger a_j + \sum_i \partial_t^2 \mathbf{s} \cdot \mathbf{R}_i a_i^\dagger a_i. \tag{2.25}
$$

Note that the above derivation does not depend on the statistics of the particles: it works equally well for bosons and fermions. Having obtained this second-quantised form of the Hamiltonian, we can add other terms to the Hamiltonian. As long as they do not contain external potentials, they will not have any influence on the above derivation.

2.3   Dipolar interactions

The Hubbard models shown in Eq. (2.1) and (2.2) feature only on-site interactions. One of the possible extensions is to include density-density interactions between different sites. The resulting model is often called 'extended Hubbard model':

$$
H = -J \sum_{\langle i,j \rangle} a_i^\dagger a_j + \sum_{i,j} \frac{U_{i,j}}{2} a_i^\dagger a_j^\dagger a_j a_i - \mu \sum_i n_i. \tag{2.26}
$$

While it is an extension of the traditional Hubbard model, it is certainly not the only possible one. In the interest of clarity, we will refer to it as the Hubbard model with long-range interactions, 'long-range' denoting anything beyond on-site.

Many studies of dipolar atoms in optical lattices focus on 2D systems, where the dipoles are polarised perpendicularly to the plane of the lattice. The interaction between two identical polarised dipoles displaced by a vector $\mathbf{r}$ is proportional to the dipole moment squared and the inverse cube of the distance:

$$V(\mathbf{r}) \propto d^2 \frac{1 - 3\cos^2 \zeta}{r^3}, \tag{2.27}$$

where ζ is the angle between the direction of polarisation and the displacement vector, d is the dipole moment, and r is the distance between the dipoles. If the displacement vector is perpendicular to the polarisation vector, which is always the case with dipoles in a 2D lattice with perpendicular polarisation, this interaction is repulsive. It can be made attractive, by inclining the polarisation relative to the plane by an angle φ and rotating it at a frequency much higher than the trapping frequency of the particles. In that limit, the particles feel an effective, time-averaged interaction, given by (see Ref. [32])

$$\langle V(\mathbf{r}) \rangle_t = g_{dd} d^2 \frac{1 - 3\cos^2 \zeta}{r^3} \underbrace{\frac{3\cos^2 \varphi - 1}{2}}_{a(\varphi)}. \tag{2.28}$$

With this technique, the interaction can be made attractive even for $\zeta = \pi/2$, by setting $\varphi > \cos^{-1} \sqrt{1/3}$. Another way to obtain attractive dipolar interactions is to orient the dipoles within the plane; however, the interaction will be rendered anisotropic in this case, and always be repulsive along a certain direction. For a more in-depth discussion of how the various off-site interaction coefficients can be arranged, see section 5.2.2.
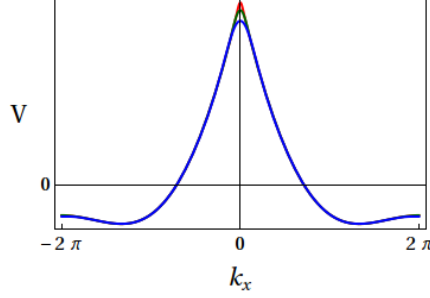
Figure 2.2: The Fourier transform of the isotropic dipolar interaction, at $k_y = 0$. The different plots represent a cut-off of 5 (blue), 10 (green), or 30 (red) lattice spacings.

Momentum space representation

Since many of the effects to be studied in this thesis are easiest to describe and study in momentum space, we are interested in the Fourier transform of the dipolar interaction:

$$
\begin{aligned}
\tilde{V}(\mathbf{k}) &= \frac{1}{N_s} \sum_{\mathbf{r}} e^{-i\mathbf{k}\cdot\mathbf{r}} V(\mathbf{r}) \\
&= d^2 g_{dd} \frac{1}{N_s} \sum_{\mathbf{r}} e^{-i\mathbf{k}\cdot\mathbf{r}} \frac{1 - 3\cos^2\zeta}{r^3}.
\end{aligned}
\tag{2.29}
$$

In the case where $\zeta = \pi/2$ for all (in-plane) displacement vectors, the interaction is repulsive and isotropic, and the expression for $\tilde{V}$ simplifies to

$$
\tilde{V}(\mathbf{k}) = d^2 g_{dd} \frac{1}{N_s} \sum_{\mathbf{r}} \frac{e^{-i\mathbf{k}\cdot\mathbf{r}}}{r^3}.
\tag{2.30}
$$

We can approximate this numerically by cutting off the sum at some 'large' distance. Figure 2.2 shows that apart from small corrections at small momenta, the overall momentum dependence does not change much at cut-

offs of more than 5 or 10 lattice sites. The significance of a momentum-dependent interaction becomes apparent when studying its expectation value in kinetic eigenstates. The statistics, Bose-Einstein or Fermi-Dirac, determine the sign of the exchange term, and thus of the effective interaction, as discussed in section 4.1.2.

Chapter 3

Finite-momentum Bose-Einstein condensates in 2D square optical lattices

Abstract

In this chapter[1], we consider ultracold bosons in a 2D square optical lattice described by the Bose-Hubbard model. In addition, an external time-dependent sinusoidal force is applied to the system, which shakes the lattice along one of the diagonals. The effect of the shaking is to renormalize the nearest-neighbor hopping coefficients, which can be arbitrarily reduced, can vanish, or can even change sign, depending on the shaking parameter. It is therefore necessary to account for longer-distance hopping terms, which are renormalized differently by the shaking, and introduce anisotropy into the problem. We show that the competition between these different hopping terms leads to finite-momentum condensates, with a momentum that may be tuned via the strength of the shaking. We calculate the boundaries be-

---

[1]This chapter is based on the publication *Finite-momentum Bose-Einstein condensates in 2D square optical lattices*, Phys. Rev. A **84**, 013607 (2011) by M. di Liberto, O. Tieleman, V. Branchina, and C. Morais Smith.

tween the Mott-insulator and the different superfluid phases, and present the time-of-flight images expected to be observed experimentally.

3.1 Introduction

Finite-momentum condensates have recently attracted a great deal of attention. In the original two proposals by Fulde, Ferrel, Larkin, and Ovchinnikov, it was argued that finite momentum Cooper pairs would lead to inhomogeneous superconductivity, with the superconducting order parameter varying spatially (the so-called FFLO phase) [75, 76]. Early NMR experiments at high magnetic fields and low temperatures in the heavy-fermion compound $CeCoIn_5$ have shown indications of an FFLO phase [77, 78, 79], although recent data suggest the existence of a more complex phase, where the exotic FFLO superconductivity coexists with an incommensurate spin-density wave [80]. For ultracold fermions with spin imbalance, on the other hand, the observation of the FFLO phase has been recently reported in 1D [81].

Earlier theoretical studies of a square-lattice toy model for a scalar field, where non-trivial hopping beyond nearest neighbors was taken into account, revealed that quantum phases, in which the order parameter is modulated in space, may be generated [82]. Finite-momentum condensates were also experimentally detected for bosons in more complex lattice geometries, such as the triangular lattice under elliptical shaking [10], or for more complex interactions, as e.g. for spinor bosons in a trap in the presence of Zeeman and spin-orbit interactions [83]. With regard to bosons in a square lattice, it was recently shown that changing the sign of the tunnelling matrix element by shaking the lattice, leads to a finite-momentum condensate in the corner of the Brillouin zone [19, 25]; furthermore, a staggered gauge field was predicted to have similar effects on the condensation momentum [29]. In this case, the bosons condense either at zero momentum or in the corner of the Brillouin zone, and a first-order phase transition occurs between these two phases [29].

In this chapter, we propose that finite-momentum condensates can be

realized for bosons in a shaken square lattice and that we may *tune* the momentum of the condensate smoothly from zero to π, by varying the shaking parameter K_0. We consider a 2D square lattice shaken along one diagonal and investigate the effect of next-nearest-neighbor (N3) and next-next-nearest neighbor (N4) hopping in the behavior of a bosonic system. The shaking leads to an effective renormalization of the nearest-neighbor (NN) hopping parameter, which can vanish or even become negative [17]. When this parameter is tuned to be very small, longer-distance hopping terms, which are usually negligible, may become relevant and must therefore be included in the model. Although the N3 hopping coefficients are strictly zero in 2D optical lattices where the x- and y-directions are independent (*i.e.* in separable potentials), they are relevant for non-separable optical lattices. In this chapter, we show that a *tunable* finite-momentum condensate can be realized in a certain range of parameters for a realistic and simple setup, thus providing the possibility of realising and controlling finite-momentum Bose-Einstein condensates (BECs).

The structure of this chapter is as follows: In section 3.2, we introduce an extended Bose-Hubbard model which includes longer-distance hopping coefficients in a non-separable 2D square optical lattice potential, and introduce a sinusoidal shaking force to the system. Next, we show in section 3.3 how the finite-momentum condensate arises, and how the condensation momentum depends on the shaking. We present a 3D phase diagram, with as parameters the Hubbard interaction U, the chemical potential μ, and the shaking parameter K_0, and indicate the parameter regime for the realization of the tunable momentum condensate in section 3.4. Finally, in section 3.5, we calculate the expected outcome of time-of-flight experiments, and present some discussion and conclusions in section 3.6.

3.2   The model

3.2.1   Non-separable potential

Before discussing the generic 2D problem, let us recall the behavior of 1D lattices and 2D separable lattices. A simple calculation shows that in

1D shaken optical lattices of the form $V(x) = (V_0/2)\cos(2kx)$ (V_0 is the potential depth and $k = 2\pi/\lambda$ is the wave vector of the laser beam), N3 hopping coefficients do not change the position of the global minima in the single-particle spectrum but generate metastable states. 2D separable potentials do not introduce new physics from this point of view, leading us to consider non-separable ones. The simplest non-separable potential in 2D is given by [15]

$$V(\mathbf{r}) = -V_0\Big\{ \sin^2[k(x+y)] + \sin^2[k(x-y)]$$
$$+ 2\alpha \sin[k(x+y)]\sin[k(x-y)]\Big\}, \tag{3.1}$$

where we will make the choice $\alpha = 1$ in the remainder of this work. Had we chosen $\alpha = 0$, the potential would have been separable, whereas for $0 < \alpha < 1$ the potential would correspond to a superlattice, with neighboring wells of different depths. The parameter α is tunable by means of the phase difference between the x- and y-laser beams [15, 84, 85]: Given a 2D square lattice generated by the laser electric field

$$\mathbf{E} = \mathbf{E}_x^+ + \mathbf{E}_x^- + \mathbf{E}_y^+ + \mathbf{E}_y^-$$
$$\mathbf{E}_x^\pm = Ae^{\pm ikx}e^{-i\omega t}e^{i\theta/2}\mathbf{p}_1 \tag{3.2}$$
$$\mathbf{E}_y^\pm = Ae^{\pm ikx}e^{-i\omega t}e^{-i\theta/2}\mathbf{p}_2,$$

with k being the inverse lattice constant, ω the frequency of the lasers, $\mathbf{p}_{1,2}$ the polarisation vectors of the two beams, and θ the phase difference between them, the lattice intensity is then given by

$$|\mathbf{E}|^2 = 4A^2\Big[\cos^2(kx) + \cos^2(ky) + 2cos(kx)\cos(ky)\cos(\theta)\mathbf{p}_1 \cdot \mathbf{p}_2\Big]. \tag{3.3}$$

Setting the two polarisation vectors equal, the interference term proportional to $\alpha = \cos\theta$ survives. Setting the phase difference $\theta = 0$ then allows the experimentor to generate the lattice shown in fig. 3.1.
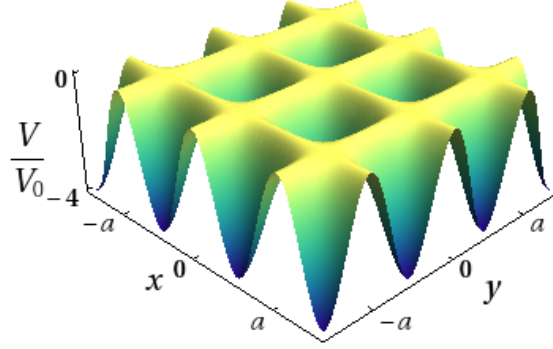
Figure 3.1: The non-separable optical potential $V(x, y)$ given by Eq. (3.1) with $\alpha = 1$.

3.2.2   Hopping coefficients

As shown in e.g. Ref. [1] and briefly discussed in section 2.1, we can calculate the hopping coefficients from the exact band structure

$$E_n(\mathbf{q}) = \sum_{\mathbf{R}} t_n(\mathbf{R}) \, e^{i\mathbf{q}\cdot\mathbf{R}}, \tag{3.4}$$

where n is the band index, $\mathbf{q}$ is the quasimomentum, and $\mathbf{R}$ is a lattice vector. In this notation, $t_n(\mathbf{R})$ is the hopping coefficient between two sites separated by the lattice vector $\mathbf{R}$ in the n-th energy band. The non-separable optical potential generates hopping coefficients along the diagonal of the lattice which were exactly zero for separable potentials. A lattice vector has the form $\mathbf{R} = m_{\mathbf{R}} a \mathbf{e}_1 + n_{\mathbf{R}} a \mathbf{e}_2$, where $a = \lambda/2$ is the lattice spacing, $m_{\mathbf{R}}$ and $n_{\mathbf{R}}$ are integers, and $\mathbf{e}_1$ and $\mathbf{e}_2$ are dimensionless unit vectors in the x- and y-directions. $\mathbf{R}$ is indicated in short notation as $(m_{\mathbf{R}}, n_{\mathbf{R}})$. For the non-separable potential that we have introduced, we expect to find nonzero hopping terms also for pairs of sites separated by dimensionless lattice vectors like $(1, 1)$ or $(2, 1)$, which vanish identically for separable lattices. Table 3.1 shows the most relevant lowest-band hopping coefficients

for shallow lattices. Longer-distance hopping coefficients are neglected, because they are at least an order of magnitude smaller than the N4 terms, and therefore not important, as will become clear afterwards.

V_0/E_r	$(1,0) \leftrightarrow -t$	$(1,1) \leftrightarrow t'$	$(2,0) \leftrightarrow t''$
1.0	-2.45×10^{-2}	-8.89×10^{-4}	8.88×10^{-4}
2.0	-4.52×10^{-3}	-6.65×10^{-5}	2.27×10^{-5}
3.0	-1.06×10^{-3}	-5.89×10^{-6}	1.06×10^{-6}
4.0	-2.97×10^{-4}	-6.74×10^{-7}	7.86×10^{-8}

Table 3.1: Relevant hopping matrix elements (in units of the recoil energy E_r) of the lowest band for shallow lattices. Numbers obtained by Fourier decomposition of numerically calculated approximate band structure. Calculation performed by M. di Liberto as part of his MSc thesis research, which I co-supervised.

3.2.3 Periodic shaking

We will assume that the lowest-orbital Wannier functions are still even and real for this non-separable potential. As shown by Kohn [71], this can be proven for separable potentials; for non-separable ones it is also a reasonable conjecture, supported by numerical simulations, as shown in Ref. [86]. If we apply a driving sinusiodal force like the one studied in Ref. [17], but now along one of the diagonals, the shaking term in the co-moving reference frame that has to be added to the Hamiltonian reads

$$W(\tau) = K \cos(\omega\tau) \sum_{\mathbf{R}} (m_{\mathbf{R}} + n_{\mathbf{R}}) n_{\mathbf{R}}, \qquad (3.5)$$

where ω is the shaking frequency, τ is the real time, and $n_{\mathbf{r}}$ is the density operator at site $\mathbf{r}$. Following the approach discussed in Refs. [17], the non-interacting effective Hamiltonian for the quasienergy spectrum in the

high-frequency limit $\hbar\omega \gg U, t$ (and thus $\hbar\omega \gg t', t''$) is

$$
\begin{aligned}
H_{\text{eff}}^0 = & - t J_0(K_0) \sum_{\mathbf{r}, \nu=1,2} a_{\mathbf{r}}^\dagger a_{\mathbf{r}\pm\mathbf{e}_\nu} + t' J_0(2K_0) \sum_{\mathbf{r}} a_{\mathbf{r}}^\dagger a_{\mathbf{r}\pm(\mathbf{e}_1+\mathbf{e}_2)} \\
& + t' \sum_{\mathbf{r}} a_{\mathbf{r}}^\dagger a_{\mathbf{r}\pm(\mathbf{e}_1-\mathbf{e}_2)} + t'' J_0(2K_0) \sum_{\mathbf{r}, \nu=1,2} a_{\mathbf{r}}^\dagger a_{\mathbf{r}\pm 2\mathbf{e}_\nu},
\end{aligned}
\tag{3.6}
$$

where the shaking parameter is $K_0 = K/\hbar\omega$ (see section 2.2 for more details on the derivation). The Bessel function $J_0(x)$ has a node at $x \simeq 2.405$, but not in the vicinity of $x \approx 4.81$; hence, when the NN hopping coefficient $t_{\text{eff}} = t\, J_0(K_0)$ is negligible, the longer-distance ones are not. The role of N3 tunnelling in the absence of NN tunnelling was also addressed in Ref. [26]. Note that the hopping coefficient along the diagonal perpendicular to the shaking direction is not affected by the shaking, in accordance with Eq. (2.25).

3.3   Tunable finite-momentum condensate

The effective Hamiltonian from Eq. (3.6) is diagonal in reciprocal space and the single-particle spectrum reads

$$
\begin{aligned}
E_{\mathbf{k}} = & - 2t J_0(K_0) \left[\cos(k_1) + \cos(k_2)\right] + 2t' J_0(2K_0) \cos(k_1 + k_2) \\
& + 2t' \cos(k_1 - k_2) + 2t'' J_0(2K_0) \left[\cos(2k_1) + \cos(2k_2)\right],
\end{aligned}
\tag{3.7}
$$

where $k_\nu = \mathbf{k}\cdot\mathbf{e}_\nu$ and we have set the lattice constant to unity. The spectrum has an absolute minimum at the center of the Brillouin zone ($\mathbf{k} = 0$) when K_0 is below a critical value that depends on the lattice depth V_0. In a small interval around $K_0 \approx 2.405$, two symmetric minima develop along one diagonal of the Brillouin zone at $\pm\mathbf{k}_0$, as shown in Fig. 3.2. For higher values of K_0, there is a single minimum in the corner of the Brillouin zone. We may determine the precise position of these two minima by studying the first derivative of the single-particle spectrum for $k = k_1 = k_2$. The non-trivial minima are given by the solution of the equation

$$
\cos(ka) = \frac{J_0(K_0)}{2J_0(2K_0)(t_1 + 2t_2)} \equiv f(K_0),
\tag{3.8}
$$
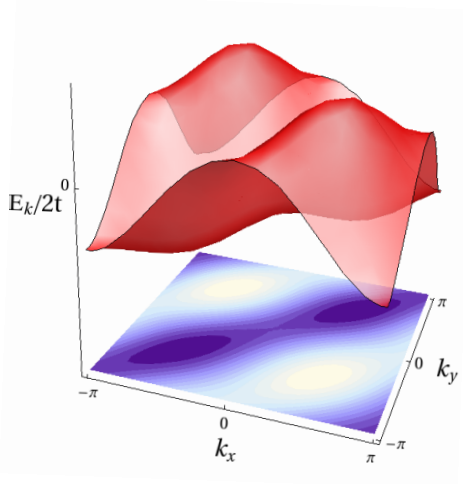
Figure 3.2: Single-particle spectrum at $V_0 = 3E_r$ for $K_0 = 2.4048$ and contour plot.

where $t_1 = t'/t$ and $t_2 = t''/t$. We have found that for $V_0 = 2E_r, 3E_r$, and $4E_r$, the second derivative of the single-particle spectrum shows that Eq. (3.8)) corresponds to a true minimum, while for $V_0 = 1E_r$ it is a maximum. Although these numbers seem low in comparison to the usual rule-of-thumb lattice depth where the single-band approximation is justified ($V_0 \geq 5E_r$ is often used), one must keep in mind that due to the interference term, the potential barrier between two minima is $4V_0$, whereas in a standard separable lattice potential it is given by V_0 itself. Hence, the single-band approximation remains justified in the present case.

The largest interval Σ of the shaking parameter K_0 for which the non-trivial minima appear, has been found to be at lattice depth $V_0 = 2.2E_r$, where the condensation momentum is finite for $2.4003 < K_0 < 2.4093$. Since we expect the bosons to condense at the minimum of the single-particle spectrum, the condensation momentum given by Eq. (3.8)) is a function of the shaking parameter K_0 and smoothly evolves from $\mathbf{k} = \mathbf{0}$ at

the left edge of Σ to $\mathbf{k} = (\pi, \pi)$ at the right edge of Σ, see Fig. 3.3. The two minima in the Σ region are inequivalent because they are not connected by reciprocal lattice vectors, and therefore both have to be taken into account when determining the BEC ground state (see below). The arccosine shape of the evolution curve can be explained by linearising Eq. (3.8) around $K_0 \approx 2.405$, which is a good approximation because $\Sigma \ll 1$. The size of the interval Σ is determined by the ratios t'/t and t''/t, and is consequently small.

In the absence of interactions, the ground state of the tunable-momentum SF phase with momenta $\pm \mathbf{k}_0$ would be highly degenerate, given by

$$
\begin{aligned}
|G\rangle &= \sum_{n=0}^{N} \frac{c_n}{\sqrt{n!(N-n)!}} (a_{\mathbf{k}_0}^\dagger)^n (a_{-\mathbf{k}_0}^\dagger)^{N-n} |0\rangle \\
&= \sum_{n=0}^{N} c_n |n_{\mathbf{k}_0}, (N-n)_{-\mathbf{k}_0}\rangle,
\end{aligned}
\tag{3.9}
$$

where the coefficients c_n can be chosen freely, only constrained by the normalization condition $\sum_n |c_n|^2 = 1$. The ground state is thus $N + 1$-fold degenerate, where N is the number of particles.

3.4   Interactions

Let us now consider an additional term to the Hamiltonian given in Eq. (3.6), which describes the local interactions between the bosons

$$
H_{\text{int}} = \frac{U}{2} \sum_{\mathbf{r}} n_{\mathbf{r}}(n_{\mathbf{r}} - 1).
\tag{3.10}
$$

We will treat the interactions between the atoms in a perturbative way and study their effect on the ground state degeneracy. By applying first-order perturbation theory, we find that the correction to the ground-state energy $N E_{\mathbf{k}_0}$ is given by

$$
\langle m, N - m | H_{\text{int}} | n, N - n \rangle = \frac{U}{2N_s} \left[-2n^2 + 2nN + N(N - 1) \right] \delta_{mn},
\tag{3.11}
$$
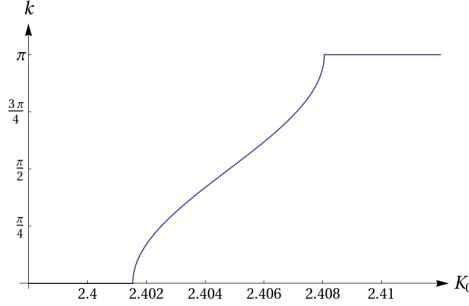
Figure 3.3: Evolution of the minimum in the single-particle spectrum in units of the lattice spacing a as a function of the shaking parameter K_0 at $V_0 = 3E_r$ (only the positive branch is considered).

where N_s is the number of lattice sites. The matrix element is in diagonal form and the eigenvalues are an upside down parabola in n. This means that the minima are at the edge of the interval $n \in [0, N]$ and that they are degenerate. Interactions have partially removed the degeneracy; the perturbative (degenerate) ground state to zeroth order is

$$|G\rangle = \frac{c_+}{\sqrt{N!}}(a_{\mathbf{k}_0}^\dagger)^N |0\rangle + \frac{c_-}{\sqrt{N!}}(a_{-\mathbf{k}_0}^\dagger)^N |0\rangle \tag{3.12}$$

and has energy

$$\langle H \rangle = \langle H_0 \rangle + \langle H_{\text{int}} \rangle = N E_{\mathbf{k}_0} + \frac{U}{2N_s} N(N-1). \tag{3.13}$$

Eq. (3.12) shows that the ground state is a superposition of two degenerate states in which all the particles have momentum $\mathbf{k}_0$ or $-\mathbf{k}_0$. These two states are entangled and behave in a very similar way to the states found by Stanescu *et al.* [87] for condensates with spin-orbit coupling, as well as the time-reversal symmetry breaking BECs studied by Eckardt *et al.* [14].

The superposition described in Eq. 3.12 is a Schrödinger cat state, which can be expected to be very fragile with respect to interactions with the

environment. It is composed of two states which each break time-reversal symmetry (all particles in momentum state $\mathbf{k}_0$ or in $-\mathbf{k}_0$). A collapse of the cat state corresponds to choosing one of the two momenta, similar to the stabilisation of BECs by interactions. In this particular case, it would also involve spontaneous time-reversal symmetry breaking, due to the nature of the two states composoing the Schrödinger cat state.

Aside from the partial lifting of the degeneracy, more intriguing effects can be expected from interactions - even 'simple' on-site ones such as discussed here. Since they induce depletion of the condensate, it is noteworthy that the spectrum is most shallow along the diagonal on which the minima lie. Hence, excitations are likely to be predominantly along that line, possibly inducing quasi-one-dimensional behaviour into the system. The superfluidity associated with the finite-momentum BEC could show anisotropic behaviour: the response to potential differences in different directions would not be the same.

3.4.1   Phase diagram

One can generalize the mean-field approach described in Ref. [24] to calculate the MI-SF phase boundaries, taking into account longer-distance hopping terms. The outcome is

$$
\begin{aligned}
\bar{\mu}_\pm =\;& \frac{\bar{U}}{2}(2N_0 - 1) + \frac{\epsilon_{\mathbf{k}_0}}{2} \\
& \pm \frac{1}{2}\sqrt{\epsilon_{\mathbf{k}_0}^2 + 2(2N_0 + 1)\bar{U}\epsilon_{\mathbf{k}_0} + \bar{U}^2},
\end{aligned}
\tag{3.14}
$$

where $\bar{\mu} = \mu/2t$, $\bar{U} = U/2t$, $\epsilon_{\mathbf{k}_0} = E_{\mathbf{k}_0}/2t$ and $\mathbf{k}_0$ is the condensation momentum, which depends on the shaking parameter K_0. Plotting $\bar{\mu}_\pm$ then gives the phase diagram, which is shown in Figs. 3.4 and 3.5. We note that the condensation momentum is, to leading order, not changed by the interactions (higher-order Bogolyubov theory shows a shift; cf. [14]). This can be seen e.g. by doing first order perturbation theory calculations: in the presence of interactions, the energy per particle is shifted by an amount of $NU/2N_s$, which is momentum independent.
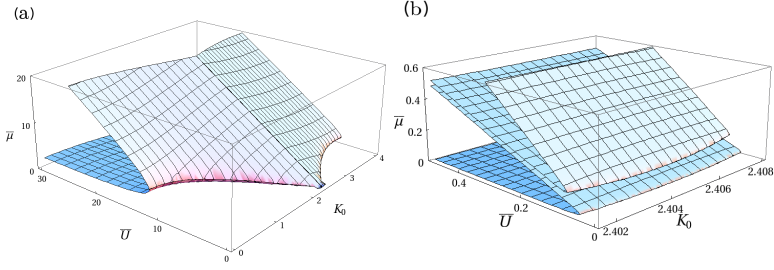
Figure 3.4: Phase boundaries for $V_0 = 3E_r$ where $\bar{\mu} \equiv \mu/2t$ and $\bar{U} \equiv U/2t$: (a) lobe with $N_0 = 1$; (b) lobes with $N_0 = 1, 2$ in the region of the tunable finite-momentum condensate.
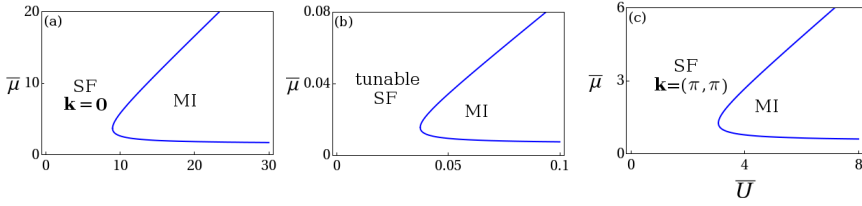
Figure 3.5: Phase boundaries between the Mott-insulator and the superfluid phase for $V_0 = 3E_r$ at fixed K_0 and filling factor $N_0 = 1$: (a) $K_0 = 1$; (b) $K_0 = 2.405$; (c) $K_0 = 3$. Note the different scales for each plot.
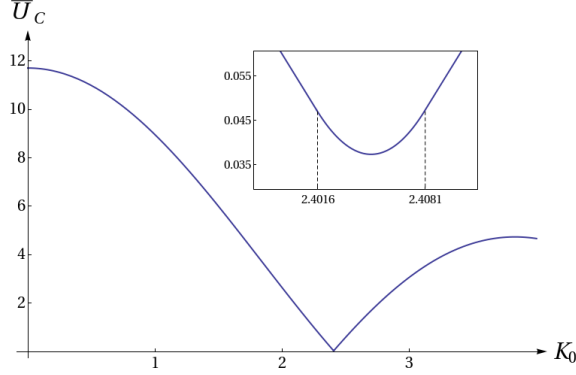
Figure 3.6: Critical value $\bar{U}_c = (U/2t)_c$ at $V_0 = 3E_r$ as a function of the shaking parameter K_0; in the inset, we show the region $2.4016 \leq K_0 \leq 2.4081$ where the tunable finite-momentum condensate is generated. Except in the small region where the finite-momentum condensate is generated, $\bar{U}$ nearly coincides with $\bar{U}_0 J_0(K_0)$, where $\bar{U}_0$ is the value of $\bar{U}$ at $K_0 = 0$. The two lines are indistinguishable in the figure.

3.5   Experimental considerations

The lobe with unit filling $N_0 = 1$ yields a critical value of $\bar{U}$ below which only the SF phase is allowed, see Fig. 3.6. Typical values of U are too large to allow us to probe the tunable-momentum SF with ordinary experimental setups. However, we can decrease U by reducing the s-wave scattering length with Feshbach resonances, which are available for both the commonly used Rubidium isotopes and also for other alkali atoms. We remark that although the range of K_0 in which the condensation momentum is tunable is very small, the required precision should be within experimental control [88]. Another challenges could arise due to the shallow nature of the minima, requiring very low energies to detect the effects discussed here.

The quantum phases discussed above could be experimentally observed by performing the usual time-of-flight experiments. These experiments

measure the momentum-space density distribution

$$n(\mathbf{k}) = \left\langle \psi^\dagger(\mathbf{k})\psi(\mathbf{k}) \right\rangle = N|W(\mathbf{k})|^2 \left(|c_+|^2\delta_{\mathbf{k},\mathbf{k}_0} + |c_-|^2\delta_{\mathbf{k},-\mathbf{k}_0}\right), \qquad (3.15)$$

where $W(\mathbf{k})$ is the Fourier transform of the Wannier function and we adopted the coherent state approximation for the SF ground state. The delta functions select the positions of the peaks in the absorption image and are a clear signal of the presence of such a condensate. Considering the hypothetical situation of an environment-free experiment, the first atom that is measured, has one of the two momenta, and causes the wavefunction to collapse onto the state where all atoms have that momentum, resulting in a single peak. However, interactions with the environment will in realistic experimental situations already have caused such a collapse before the measurement process begins. An array of 2D identical systems would reveal a pattern with both peaks, since either momentum is equally likely to be measured. By studying the envelope function that suppresses the height of the peaks outside the first Brillouin zone, we can investigate the effect of the non-separability of the optical potential on the Wannier functions in reciprocal space.

In Fig. 3.7 we show a qualitative indication of the expected the pattern of the time-of-flight image described by Eq.(3.15). Note that the image is only meant to indicate expected characteristics of the measurement, not quantitatively predict density distributions. The Fourier transform of the Wannier function suppresses the peak heights in higher Brillouin zones, which we have modelled by a Gaussian envelope. In addition, we have qualitatively included the broadening of the peaks due to the external trap by replacing every peak by a highly localised Gaussian.

3.6 Discussion and conclusions

We have explored the possibility to generate finite-momentum condensates in optical lattices under shaking, where the suppression of hopping can be tuned by the shaking. This opens up the possibility to investigate the role
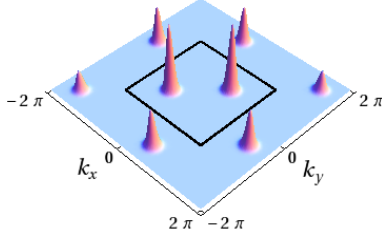
Figure 3.7: Time-of-flight picture expected from experiment as a signal of the finite-momentum-condensate phase. The black square indicates the first Brillouin zone, and the condensation momentum represented in this image is $\mathbf{k}_0 = 2\pi/5a, 2\pi/5a$. The axes are in units of the inverse lattice constant $1/a$.

of longer-distance hopping. We have studied non-separable optical potentials in 2D square lattices, and found that N3 hopping coefficients that vanish identically in separable potentials survive, although they are significantly smaller than their NN counterparts. By applying the shaking along the diagonal of the lattice, we found that in a small region of the shaking parameter, where the NN tunneling rate is suppressed, two kinds of longer-distance hopping coefficients govern the dynamics of the condensate. In this region, we have unveiled an intermediate phase, for which the condensation point shifts continuously from the center to the edge of the Brillouin zone as we the shaking parameter is tuned. There are two minima in the single-particle spectrum and they are symmetric with respect to the center of the Brillouin zone. In addition, we found that in first approximation, small interactions between the particles force the ground state to be a Schrödinger-cat-like superposition of two possible Fock states, both of which spontaneously break time-reversal symmetry: one where all the particles condense in one minimum and the other where all the particles condense in the second minimum. Since such a superposition is a Schrödinger

cat state, it is very sensitive to collapse. More sophisticated calculations would be informative here, e.g. Bogolyubov approximation-based estimates of condensate depletion.

Finally, we note that the tunable-momentum condensate should be experimentally detectable for relatively weak on-site interactions. Although a few challenges (or avenues for further research) are present, the required strengths can in principle be achieved with present state-of-the-art experimental techniques, and we hope that our results can stimulate further experiments in this direction.

Chapter 4

Spontaneous time-reversal symmetry breaking for spinless fermions on a triangular lattice

Abstract

In this chapter[1], we investigate a system of spin-polarised (*i.e.* single-species) fermions in a two-dimensional triangular lattice. The hopping coefficients and filling factor are chosen such that the system is kinetically frustrated. In addition, a nearest-neighbour (NN), or longer-ranged repulsive interaction is considered, since on-site interactions are not allowed due to the Pauli exclusion principle. In order to obtain physical insight into the system, we study it in the weakly interacting regime, at mean-field level. Exact diagonalisations on small systems support the mean-field results. We find that at low filling factors, time-reversal symmetry is broken

---

[1]The publication *Spontaneous time-reversal symmetry breaking for spinless fermions on a triangular lattice*, arXiv:1210.4338, by O. Tieleman, O. Dutta, M. Lewenstein, and A. Eckardt, Ref. [61], is based on the material presented in this chapter.

spontaneously, leading to a pattern of staggered currents running around the elementary lattice plaquettes. Furthermore, a density-wave appears due to the repulsive interactions, as well as an exotic phase which combines the two broken symmetries. Possible realisations of the system are discussed towards the end of the chapter.

4.1 Hamiltonian - basic considerations

4.1.1 Single particle: kinetic frustration

Kinetic frustration affects the low-energy single-particle states, and occurs when not all hopping terms can be simultaneously minimised. The hopping terms of the Hamiltonian are given by

$$H_h = \sum_{j=1}^{3} \sum_{\mathbf{r}} \sum_{\sigma=\pm 1} J_j c_{\mathbf{r}}^{\dagger} c_{\mathbf{r}+\sigma \mathbf{e}_j}, \tag{4.1}$$

where $\mathbf{r}$ runs over all lattice sites, and the lattice is spanned by any two of the three primitive vectors $\mathbf{e}_j$, given by $(1,0)$, $(-1,\sqrt{3})/2$, and $(-1,-\sqrt{3})/2$ in units of the lattice constant (see fig. 4.1, left panel). By choosing either one or three of the hopping coefficients J_j to be negative, a single-particle state can be found that minimises all hopping terms, but not one that maximises all of them. If the number of negative coefficients is even, however, the situation is reversed: no single-particle state can be found that minimises all hopping terms, but they can all be maximised at the same time. In this case, the system is called *frustrated*. The degree of frustration can be measured by the ratio of the lowest achievable energy to the sum of the minimal values of all the different hopping terms. Note that due to the complex nature of the wavefunction, other configurations than those discussed above are also possible, where *e.g.* none of the hopping terms are individually minimised. In the case of the triangular plaquette, the minimal energy state is in fact of this type: the wavefunction phases shift by $2\pi/3$ between neighbouring lattice sites. For the connection between this intersite phase difference and the energy, see Eq. (4.5).

The frustrated situation is illustrated in the right panel of fig. 4.1: The sign of the wavefunction on the three lattice sites of the elementary plaquette shows the frustration. Starting from a positive sign in the lower left corner, it is possible to minimise two of the three hopping terms, e.g. the two non-horizontal bonds, by giving the wavefunction a positive signe everywhere. To minimise the third one, however, the wavefunction has to simultaneously have both a positive and a negative sign in the lower right corner. Such a system can be realised experimentally by periodically shaking the lattice, as was done in Ref. [10], or by considering an unshaken lattice at (fermionic) filling just below unity: in that case, the holes experience kinetic frustration.
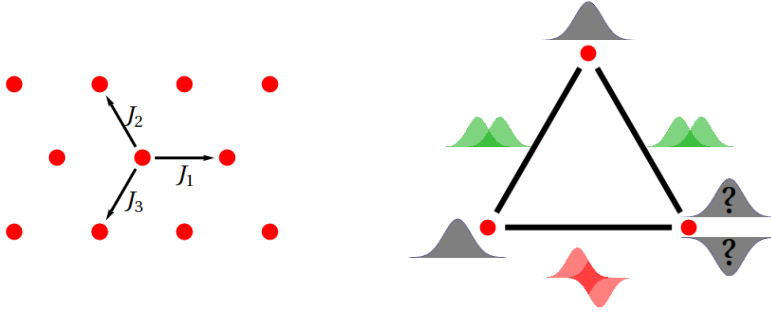
Figure 4.1: Left panel: the triangular lattice, with three different hopping coefficients J_j along the elementary lattice vectors $\mathbf{e}_j$. Right panel: sketch of the frustration due to positive hopping terms (negative terms are coloured green, positive ones red). In this illustration, the frustration appears in the impossibility of finding a wavefunction for the lower left corner that satisfies both hopping terms connected to it.

After Fourier transforming and expressing the hopping term in momentum representation, we obtain the dispersion relation shown in fig. 4.2. The two minima in the single-particle dispersion relation are, in this case, a consequence of the real-space frustration discussed above. A non-frustrated

triangular lattice has a dispersion relation with one unique minimum.
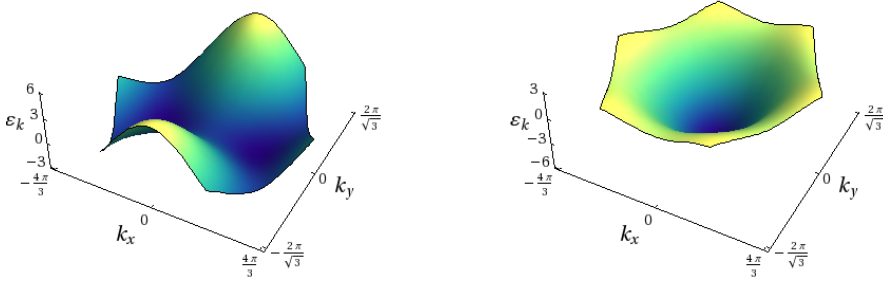
Figure 4.2: Left panel: the frustrated spectrum, with two inequivalent minima at $\mathbf{k} = \pm(2\pi/3a, 0)$. Right panel: the non-frustrated spectrum, where all J_j are negative.

The momentum-space version of H_h is given by

$$H_h = 2 \sum_{\mathbf{k} \in \mathrm{BZ}_1} \underbrace{\sum_{j=1}^{3} J_j \cos(\mathbf{k} \cdot \mathbf{e}_j)}_{\epsilon_{\mathbf{k}}} c_{\mathbf{k}}^{\dagger} c_{\mathbf{k}}. \tag{4.2}$$

(Below, all sums over momenta run over the first Brillouin zone BZ_1, also where this is not indicated.) The two distinct possible dispersion relations $\epsilon_{\mathbf{k}}$, assuming that all three hopping coefficients have equal magnitude, are shown in fig. 4.2. These two realisations can be tuned smoothly into each other by changing the ratios of the hopping coefficients. It is noteworthy that the lowest-energy single-particle states of the frustrated dispersion relation spontaneously break time-reversal symmetry, as can *e.g.* be deduced from the fact that they do not lie at a point of reciprocal lattice symmetry. Another way of seeing this is by observing that hopping terms that are not completely extremised carry currents. Considering the operator for the current from site $\mathbf{r}$ to site $\mathbf{r}'$,

$$\hat{\mathcal{J}}_{\mathbf{r}-\mathbf{r}'} = iJ_{\mathbf{r}-\mathbf{r}'}\left(c_{\mathbf{r}'}^{\dagger}c_{\mathbf{r}} - c_{\mathbf{r}}^{\dagger}c_{\mathbf{r}'}\right), \tag{4.3}$$

we see that its expectation value in a single-particle state is sensitive to the phase difference between the two sites:

$$\langle \text{vac}| \sum_{\mathbf{j}} c_{\mathbf{j}} n_{\mathbf{j}} e^{i\theta_{\mathbf{j}}} \mathcal{J}_{\mathbf{r}-\mathbf{r}'} \sum_{\mathbf{j}'} n_{\mathbf{j}'} e^{-i\theta_{\mathbf{j}'}} c_{\mathbf{j}'}^\dagger |\text{vac}\rangle = 2 J_{\mathbf{r}-\mathbf{r}'} n_{\mathbf{r}} n_{\mathbf{r}'} \sin(\theta_{\mathbf{r}} - \theta_{\mathbf{r}'}). \tag{4.4}$$

Hence, if the phases on the two sites are either equal or separated by π, the current between them vanishes. Since the expectation value of the hopping term between two sites in the same state is given by

$$\begin{aligned}
&\langle \text{vac}| \sum_{\mathbf{j}} c_{\mathbf{j}} n_{\mathbf{j}} e^{i\theta_{\mathbf{j}}} J_{\mathbf{r}-\mathbf{r}'} \left(c_{\mathbf{r}'}^\dagger c_{\mathbf{r}} + c_{\mathbf{r}}^\dagger c_{\mathbf{r}'} \right) \sum_{\mathbf{j}'} n_{\mathbf{j}'} e^{-i\theta_{\mathbf{j}'}} c_{\mathbf{j}'}^\dagger |\text{vac}\rangle \\
&= 2 J_{\mathbf{r}-\mathbf{r}'} n_{\mathbf{r}} n_{\mathbf{r}'} \cos(\theta_{\mathbf{r}} - \theta_{\mathbf{r}'}),
\end{aligned} \tag{4.5}$$

which is extremised when the phases are equal or separated by π, we conclude that partially frustrated hopping terms carry current, and therefore break time-reversal symmetry. Further discussion of this point is presented in section 4.1.2. Ref. [14] provides a discussion of the various lowest-energy single-particle states in such a lattice, in the context of a many-particle bosonic system.

Many particles: Fermi surfaces

Since we are dealing with fermions and are interested in many-body systems, we are mostly interested in the shapes the Fermi surface takes, rather than the properties of the lowest-energy single-particle state. We will assume that all J_j have the same magnitude. In that case, at filling factors $\nu \leq 1/4$, the Fermi surface consists of two closed loops, as shown in the left panel of figure 4.3. Note that such a (non-interacting) many-body state does not break time-reversal symmetry, since the particles fill up the states around both minima equally. At quarter filling, the two loops become triangular and touch at all three corners, leading to a bowtie-shaped Fermi surface. This case was studied in Ref. [60], where a Bose-Fermi mixture was found to have a supersolid phase (the fermions form a density wave, and

superfluid bosons copy the fermionic density wave due to the Bose-Fermi interaction).
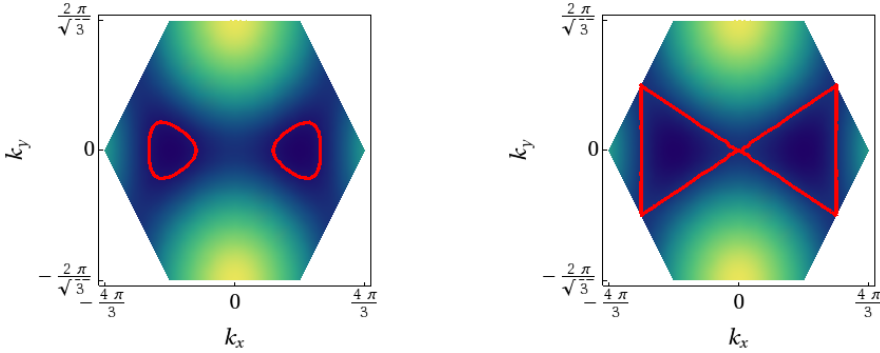
Figure 4.3: Fermi surfaces for $J_1 = -J_2 = -J_3 = -|J|$, at $\mu = -2.6J$ (left) and $\mu = -2J$ (right).

At yet higher filling factors, the two loops join, and the Fermi surface is fully connected. All frustrated single-particle states are now occupied, and the physics of the system is governed by higher-energy states, where the frustration does not play a role (recall that frustration is an effect that only affects low-energy states). Hence, at filling factors $\nu > 1/4$, the many-body system does not show any effects of the frustration anymore. The regimes we are interested in are at low filling and around quarter filling, since the corresponding Fermi surfaces are susceptible to interesting interaction-induced effects.

4.1.2 Long-range interactions

Adding generic long-range interactions to the kinetic term Eq. (4.1), we obtain the complete Hamiltonian,

$$H = \sum_j J_j \sum_{\mathbf{r}} \sum_{\sigma=\pm 1} c_{\mathbf{r}}^\dagger c_{\mathbf{r}+\sigma \mathbf{e}_j} + \sum_{\mathbf{r} \neq \mathbf{r}'} V(\mathbf{r} - \mathbf{r}') c_{\mathbf{r}}^\dagger c_{\mathbf{r}} c_{\mathbf{r}'}^\dagger c_{\mathbf{r}'}. \qquad (4.6)$$

In momentum space, the expression is

$$H = \sum_{\mathbf{k}} \epsilon_{\mathbf{k}} c_{\mathbf{k}}^{\dagger} c_{\mathbf{k}} + \sum_{\mathbf{p},\mathbf{q},\mathbf{k}} V(\mathbf{k}) c_{\mathbf{p}}^{\dagger} c_{\mathbf{p}+\mathbf{k}} c_{\mathbf{q}}^{\dagger} c_{\mathbf{q}-\mathbf{k}}, \qquad (4.7)$$

where $V(\mathbf{k})$ is the Fourier transform of $V(\mathbf{r} - \mathbf{r}')$. Below, we will discuss various consequences of such an interaction term, and briefly sketch the effects we expect in the system under investigation.

Momentum-space attraction

An insightful approximation to this interaction term in the weakly inter-acting limit is obtained by taking its expectation value in a many-particle kinetic eigenstate, characterised by sharp quasimomentum occupation numbers (which, in a fermionic Hubbard model, can only be zero or one):

$$|\{n_{\mathbf{k}}\}\rangle = \prod_{\mathbf{k}} \left(c_{\mathbf{k}}^{\dagger}\right)^{n_{\mathbf{k}}} |\text{vac}\rangle, \qquad (4.8)$$

where $n_{\mathbf{k}} \in \{0, 1\}$. In such a state, the expectation value of the interaction energy is given by

$$\sum_{\mathbf{k},\mathbf{p},\mathbf{q}} V(\mathbf{k}) \left\langle c_{\mathbf{p}}^{\dagger} c_{\mathbf{q}}^{\dagger} c_{\mathbf{q}-\mathbf{k}} c_{\mathbf{p}+\mathbf{k}} \right\rangle = \sum_{\mathbf{p},\mathbf{q}} [V(\mathbf{0}) - V(\mathbf{p} - \mathbf{q})] n_{\mathbf{p}} n_{\mathbf{q}}. \qquad (4.9)$$

This comes down to keeping only the terms $\mathbf{k} = \mathbf{p} - \mathbf{q}$ and $\mathbf{k} = \mathbf{0}$. The zero momentum exchange term simply counts all particles and adds an energy penalty, coming down to a shift in the chemical potential. The crucial point is the minus sign in front of the $V(\mathbf{p} - \mathbf{q})$-term, that appears due to the fermionic anticommutation relations. This minus sign implies that as long as we can approximate the eigenstates of the system by the momentum eigenstates, the effective momentum space interaction is attractive if the real-space interaction is repulsive and decreases with distance.

Time-reversal symmetry breaking

Given a Fermi surface consisting of two disconnected 'Fermi pools' (see fig. 4.3, left panel), at filling $\nu \leq 1/4$, the consequence of such an effective momentum-space attraction is a tendency towards imbalanced filling of the two pools. The energy cost for such an imbalanced filling is purely kinetic, since it does not fill all the lowest available kinetic energy eigenstates. Hence, one expects that at a critical ratio U/J, such the imbalance will become energetically favourable.

As mentioned above, the effects of time-reversal symmetry breaking, imbalanced momentum-space filling, and currents running through the system, are connected. To see this in the many-body context, we Fourier transform the momentum-space population difference to real space, and find

$$
\begin{aligned}
n_{\mathbf{k}} - n_{-\mathbf{k}} &= \left\langle c_{\mathbf{k}}^{\dagger} c_{\mathbf{k}} \right\rangle - \left\langle c_{-\mathbf{k}}^{\dagger} c_{-\mathbf{k}} \right\rangle \\
&= \frac{1}{N_{\mathrm{s}}} \sum_{\mathbf{r},\mathbf{r}'} \sin[\mathbf{k} \cdot (\mathbf{r} - \mathbf{r}')] \underbrace{i\left(\left\langle c_{\mathbf{r}}^{\dagger} c_{\mathbf{r}'} \right\rangle - \left\langle c_{\mathbf{r}'}^{\dagger} c_{\mathbf{r}} \right\rangle \right)}_{\mathcal{J}_{\mathbf{r}-\mathbf{r}'}/J_{\mathbf{r}-\mathbf{r}'}},
\end{aligned}
\tag{4.10}
$$

where $\mathcal{J}_{\mathbf{r}-\mathbf{r}'}$, which is an expectation value rather than an operator, denotes the current from site $\mathbf{r}$ to site $\mathbf{r}'$. To see that $\mathcal{J}_{\mathbf{r}-\mathbf{r}'}$ indeed represents the real-space currents, it is most straightforward to evaluate the expectation value of the continuity equation, $\partial_t \langle \hat{n}_i \rangle = i \langle [\hat{n}_i, H] \rangle$. The most general real-space form contains hopping terms from any site to any site:

$$
\begin{aligned}
\partial_t \langle \hat{n}_{\mathbf{r}} \rangle &= i \langle [\hat{n}_{\mathbf{r}}, H] \rangle \\
&= i \sum_{\mathbf{r}',\mathbf{r}''} J_{\mathbf{r}'-\mathbf{r}''} \left(\left\langle c_{\mathbf{r}}^{\dagger} c_{\mathbf{r}''} \right\rangle \{c_{\mathbf{r}}, c_{\mathbf{r}'}^{\dagger}\} - \left\langle c_{\mathbf{r}'}^{\dagger} c_{\mathbf{r}} \right\rangle \{c_{\mathbf{r}}^{\dagger}, c_{\mathbf{r}''}\} \right) \\
&= i \sum_{\mathbf{r}'} J_{\mathbf{r}-\mathbf{r}'} \left(\left\langle c_{\mathbf{r}}^{\dagger} c_{\mathbf{r}'} \right\rangle - \left\langle c_{\mathbf{r}'}^{\dagger} c_{\mathbf{r}} \right\rangle \right) = \sum_{\mathbf{r}'} \mathcal{J}_{\mathbf{r}'-\mathbf{r}}.
\end{aligned}
\tag{4.11}
$$

Note that the currents depend on both the Hamiltonian and the state of the system - the former dependence is related to the fact that the currents provide information about time-evolution (they are derived from the
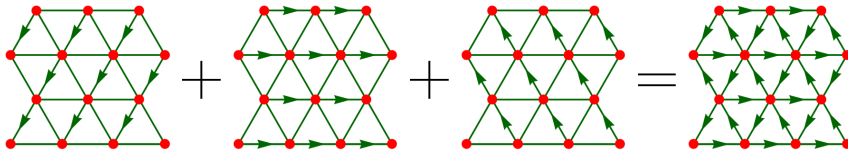
Figure 4.4: The sum of the three different currents is a staggered pattern, where the current running around the up-triangles $\triangle$ is the opposite of that running around the down-triangles $\triangledown$.

continuity equation, or, quite simply, they tell us how the particles in the system flow, *i.e.* where they will be next). Connecting the currents to the momentum-space density distribution again, we find

$$
\begin{aligned}
\mathcal{J}_{\mathbf{r}-\mathbf{r}'} &= -iJ_{\mathbf{r}-\mathbf{r}'}\left(\left\langle c_{\mathbf{r}}^{\dagger}c_{\mathbf{r}'}\right\rangle - \left\langle c_{\mathbf{r}'}^{\dagger}c_{\mathbf{r}}\right\rangle\right) = 2J_{\mathbf{r}-\mathbf{r}'}\,\mathrm{Im}\,\left\langle c_{\mathbf{r}}^{\dagger}c_{\mathbf{r}'}\right\rangle \\
&= \frac{2J_{\mathbf{r}-\mathbf{r}'}}{N_{\mathrm{s}}}\sum_{\mathbf{k}}\sin(\mathbf{k}\cdot\mathbf{e}_{j})n_{\mathbf{k}}.
\end{aligned}
\tag{4.12}
$$

The vector quantity $\mathcal{J}_{j} = \mathcal{J}_{\mathbf{e}_{j}}$ will be our order parameter when calculating the phase diagram of the time-reversal symmetry breaking phase in section 4.2. The vector has three components, since there are three nearest-neighbour current directions. Based on the continuity equation and the absence of any effect favouring an overall current running through the system, we expect the total current pattern to be staggered, as shown in fig. 4.4.

We see that the chiral ground states for the BEC found in Ref. [14] have a fermionic equivalent. In the BEC case, there is complete momentum-space imbalance: all particles occupy either one, or the other minimal-energy state. In the fermionic case, the imbalance needs not be complete; as we will see in section 4.2.1, it depends on the ratio U/J. Another significant difference is that in the BEC case, the imbalance is a consequence of an on-site interaction that is minimised by a homogeneous real-space density distribution, whereas the long-range interaction considered here favours a density wave (see section 4.3).

Density wave

Another consideration starts from the real-space formulation of the Hamiltonian: repulsive off-site density-density interactions favour breaking spatial homogeneity by inducing density waves. The simplest example is the case of NN interactions, which are minimised by surrounding high-density sites by low-density ones. Two such examples, at filling factors 1/3 and 1/4, are shown in fig. 4.5.
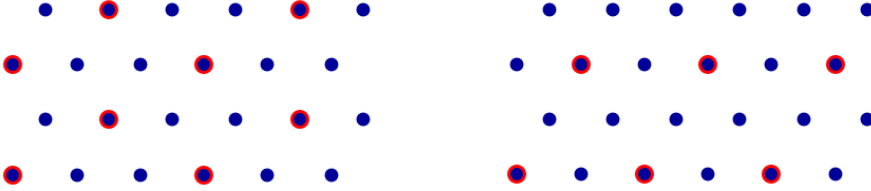
Figure 4.5: The real-space arrangements avoiding nearest-neighbour interaction energy costs, at filling factor 1/3 (left) and 1/4 (right).

However, for such a density modulation to occur in the weakly interacting limit, it should not come with a high kinetic energy cost. This condition is formalised in the requirement that the real part of the susceptibility diverges. The susceptibility, which measures the strength of the perturbation required to induce a density wave, is given by

$$\mathrm{Re}\,\chi_{\mathbf{Q}} = \sum_{\mathbf{k}} \frac{f_{\mathbf{k}} - f_{\mathbf{k}+\mathbf{Q}}}{\xi_{\mathbf{k}} - \xi_{\mathbf{k}+\mathbf{Q}}}, \tag{4.13}$$

where $\xi_{\mathbf{k}} = \epsilon_{\mathbf{k}} - \mu$, *i.e.* the single-particle spectrum shifted by the chemical potential, and $f_{\mathbf{k}} = [1 + \exp(\beta\xi_{\mathbf{k}})]^{-1}$ is the Fermi-Dirac distribution. If the Fermi surface is *nested, i.e.* if $\xi_{\mathbf{k}} \approx -\xi_{\mathbf{k}+\mathbf{Q}}$ along a finite portion of the Fermi surface, the real part of the susceptibility diverges, and the kinetic energy cost for creating density modulations with wavevector $\mathbf{Q}$ vanishes. In this case, even an infinitesimal perturbation, *i.e.* an infinitesimally weak interaction, will lead to a density wave.

Note that an attractive NN density-density interaction will not lead to density waves. In the case of the triangular lattice, the nesting condition is fulfilled at $\nu = 1/4$, but not at $\nu = 1/3$. Hence, the only density wave to be expected in the weakly interacting case is the one around quarter filling. In the strongly-interacting limit, a density wave can also appear at $\nu = 1/3$, but that is not the object of the current investigation.

In the presence of a density wave, the local density is determined by two contributions: $n_{\mathbf{r}} = n_0 + n_{\mathrm{mod}}(\mathbf{r})$. The modulating contribution n_{mod} modulates with the characteristic wavevector of the density wave, and takes both positive and negative values. The overall density obviously never becomes negative, which is ensured by the presence of the constant contribution n_0. The order parameter for a density wave with a particular wavevector is the fraction of the density that modulates. In real space, it is given by

$$\rho_{\mathbf{Q}} = \sum_{\mathbf{r}} \cos(\mathbf{r} \cdot \mathbf{Q}) n_{\mathbf{r}}. \tag{4.14}$$

In momentum space, this can be seen to correspond exactly to the expectation value of the density operator $\hat{\rho}_{\mathbf{Q}}$. The real-space density operator $\hat{\rho}_{\mathbf{r}}$ is given by

$$\hat{\rho}_{\mathbf{r}} = c_{\mathbf{r}}^{\dagger} c_{\mathbf{r}} = \frac{1}{N_{\mathrm{sites}}} \sum_{\mathbf{k},\mathbf{k}'} e^{i\mathbf{r} \cdot (\mathbf{k}-\mathbf{k}')} c_{\mathbf{k}}^{\dagger} c_{\mathbf{k}'} = \frac{1}{N_{\mathrm{sites}}} \sum_{\mathbf{p},\mathbf{q}} e^{i\mathbf{r} \cdot \mathbf{p}} c_{\mathbf{p}+\mathbf{q}}^{\dagger} c_{\mathbf{q}} = \sum_{\mathbf{p}} e^{i\mathbf{r} \cdot \mathbf{p}} \hat{\rho}_{\mathbf{p}},$$

$$\hat{\rho}_{\mathbf{p}} = \frac{1}{N_{\mathrm{sites}}} \sum_{\mathbf{q}} c_{\mathbf{p}+\mathbf{q}}^{\dagger} c_{\mathbf{q}}. \tag{4.15}$$

Fourier transforming the order parameter for the density wave, we find

$$\rho_{\mathbf{Q}} = \sum_{\mathbf{r}} \cos(\mathbf{r} \cdot \mathbf{Q}) \left\langle c_{\mathbf{r}}^{\dagger} c_{\mathbf{r}} \right\rangle = \sum_{\mathbf{k}} c_{\mathbf{k}+\mathbf{Q}}^{\dagger} c_{\mathbf{k}} = \langle \hat{\rho}_{\mathbf{Q}} \rangle, \tag{4.16}$$

which is intuitively easy to understand: it is the expectation value of the $\mathbf{Q}$-component of the density operator. Note that this is not the same as the density of the single-particle state with momentum $\mathbf{Q}$, which is given by $c_{\mathbf{Q}}^{\dagger} c_{\mathbf{Q}}$.

4.1.3 Mean-field approximation

We will study the system in a mean-field approximation, where one-particle operators $c_i^\dagger c_j$ are replaced by their averages plus fluctuations around those averages, and the fluctuations are kept only to first order. In symbols:

$$c_i^\dagger c_j = \left\langle c_i^\dagger c_j \right\rangle + \underbrace{(c_i^\dagger c_j - \left\langle c_i^\dagger c_j \right\rangle)}_{\text{fluctuation}} \tag{4.17a}$$

$$
\begin{aligned}
c_i^\dagger c_j^\dagger c_k c_l \approx {} & \left\langle c_i^\dagger c_l \right\rangle c_j^\dagger c_k + \left\langle c_j^\dagger c_k \right\rangle c_i^\dagger c_l - \left\langle c_i^\dagger c_l \right\rangle \left\langle c_j^\dagger c_k \right\rangle \\
& - \left\langle c_i^\dagger c_k \right\rangle c_j^\dagger c_l - \left\langle c_j^\dagger c_l \right\rangle c_i^\dagger c_k + \left\langle c_i^\dagger c_k \right\rangle \left\langle c_j^\dagger c_l \right\rangle .
\end{aligned}
\tag{4.17b}
$$

Note that we have not taken into account the anomalous averages of the form $\langle c_i c_j \rangle$, which describe superfluid pairing. These terms may be omitted because we are working with a repulsive interaction, where pairing is not expected. Consequently, all terms in the mean-field approximation take the form $c_{\mathbf{k}}^\dagger c_{\mathbf{k}'}$.

In the following sections, we will make various assumptions about the averages $\left\langle c_{\mathbf{k}}^\dagger c_{\mathbf{k}'} \right\rangle$. In section 4.2, we study only the time-reversal symmetry breaking discussed above, and hence assume translational invariance. In that case, we have

$$\left\langle c_{\mathbf{k}}^\dagger c_{\mathbf{k}'} \right\rangle = \left\langle c_{\mathbf{k}}^\dagger c_{\mathbf{k}} \right\rangle \delta_{\mathbf{k},\mathbf{k}'} = n_{\mathbf{k}} \delta_{\mathbf{k},\mathbf{k}'}, \tag{4.18}$$

and the effective Hamiltonian is diagonal in the quasimomentum states, taking the form $\sum_{\mathbf{k}} \omega_{\mathbf{k}} c_{\mathbf{k}}^\dagger c_{\mathbf{k}}$ where $\omega_{\mathbf{k}}$ is the single-particle spectrum shifted by the contributions from the interaction term. In section 4.3, we study only the density wave. There, we do naturally not assume translational invariance, but instead use the *ansatz*

$$\left\langle c_{\mathbf{k}\pm\mathbf{Q}_j}^\dagger c_{\mathbf{k}} \right\rangle \neq 0 \tag{4.19}$$

for a certain set of $\mathbf{Q}_j$, namely those that fulfill the nesting condition $\xi_{\mathbf{k}} \approx -\xi_{\mathbf{k}\pm\mathbf{Q}}$ for a finite part of the Fermi surface. Lastly, in section 4.4, we

study yet another phase, where both time-reversal and spatial symmetry are broken. This calculation is based on the same terms as were taken into account for the density wave. At the end, we summarise the results by presenting a unified phase diagram in which all phases found are indicated.

The route we choose for the calculations is as follows: we treat the quantities $\langle c_i^\dagger c_j \rangle$ introduced in Eq. (4.17a) as variational parameters, and extremise the corresponding free energy with respect to them. In the course of performing this extremisation, we find that it is equivalent to treating $\langle c_i^\dagger c_j \rangle$ as an expectation value and demanding that it is self-consistent, *i.e.* that when calculating that expectation value in the mean-field ground state, we find the same value as we put into the mean-field Hamiltonian. The advantage of extremisation, however, is that we do not need to calculate the values of all variational parameters, while still obtaining a phase boundary.

To conclude this introductory section, we give the complete mean-field Hamiltonian:

$$
H = \sum_{\mathbf{k}} \left(\omega_{\mathbf{k}} c_{\mathbf{k}}^\dagger c_{\mathbf{k}} + \sum_j \omega_{\mathbf{k}}^{\mathbf{Q}_j} c_{\mathbf{k}+\mathbf{Q}_j}^\dagger c_{\mathbf{k}} \right)
$$
$$
- \sum_{\mathbf{k},\mathbf{p}} \left\{ [V(\mathbf{0}) - V(\mathbf{k} - \mathbf{p})] \left\langle c_{\mathbf{k}}^\dagger c_{\mathbf{k}} \right\rangle \left\langle c_{\mathbf{p}}^\dagger c_{\mathbf{p}} \right\rangle \right. \tag{4.20a}
$$
$$
\left. + [V(\mathbf{Q}) - V(\mathbf{k} - \mathbf{p} + \mathbf{Q})] \left\langle c_{\mathbf{k}+\mathbf{Q}}^\dagger c_{\mathbf{k}} \right\rangle \left\langle c_{\mathbf{p}-\mathbf{Q}}^\dagger c_{\mathbf{p}} \right\rangle \right\},
$$
$$
\omega_{\mathbf{k}} = \epsilon_{\mathbf{k}} - \mu + 2 \sum_{\mathbf{p} \in \mathrm{BZ}_1} [V(\mathbf{0}) - V(\mathbf{k} - \mathbf{p})] \left\langle c_{\mathbf{p}}^\dagger c_{\mathbf{p}} \right\rangle \tag{4.20b}
$$
$$
\omega_{\mathbf{k}}^{\mathbf{Q}} = 2 \sum_{\mathbf{p} \in \mathrm{BZ}_1} [V(\mathbf{Q}) - V(\mathbf{k} - \mathbf{p} + \mathbf{Q})] \left\langle c_{\mathbf{p}+\mathbf{Q}}^\dagger c_{\mathbf{p}} \right\rangle. \tag{4.20c}
$$

4.2   Staggered currents

In this section, we investigate the possibility of spontaneous time-reversal symmetry breaking by the appearance of staggered currents, as depicted in

fig. 4.4. We will only take into account the spatially homogeneous terms from Eq. (4.20a), yielding a mean-field Hamiltonian that is immediately diagonal in Fourier space:

$$H_{\mathrm{MF}} = \sum_{\mathbf{k}} \omega_{\mathbf{k}} c_{\mathbf{k}}^{\dagger} c_{\mathbf{k}} - \sum_{\mathbf{k},\mathbf{p}} [V(\mathbf{0}) - V(\mathbf{k} - \mathbf{p})] n_{\mathbf{k}} n_{\mathbf{p}}, \qquad (4.21\text{a})$$

$$\omega_{\mathbf{k}} = \xi_{\mathbf{k}} + 2 \sum_{\mathbf{p}} [V(\mathbf{0}) - V(\mathbf{k} - \mathbf{p})] n_{\mathbf{p}}. \qquad (4.21\text{b})$$

By minimising the free energy corresponding to the mean-field Hamiltonian with respect to all the parameters introduced by the approximation, we find that demanding self-consistency is equivalent to treating the Hamiltonian as a variational *ansatz*. Self-consistently solving for the required parameters allows us to find the phase transition.

4.2.1   Gap equations

The free energy corresponding to the mean-field Hamiltonian, F_{MF}, is given by:

$$F_{\mathrm{SC}}^{\mathrm{MF}} = -\frac{1}{\beta} \sum_{\mathbf{k}} \ln(1 + e^{-\beta \omega_{\mathbf{k}}}) - \sum_{\mathbf{k},\mathbf{p}} n_{\mathbf{k}} n_{\mathbf{p}} [V(\mathbf{0}) - V(\mathbf{k} - \mathbf{p})]. \qquad (4.22)$$

The subscript $_{\mathrm{SC}}$ indicates that this free energy expression only takes into account the possibility of staggered currents, and not the density wave discussed in section 4.1. The superscript $^{\mathrm{MF}}$ will be dropped from here on, since we will only be working with mean-field approximations to the free energy. The first term in this free energy is obtained from the first term in Eq. (4.21a), and simply gives the free energy of a set of non-interacting fermions subject to dispersion relation $\omega_{\mathbf{k}}$. The second term is quite simply the constant correction from Eq. (4.21a). Considering a purely nearest-neighbour interaction, the interaction-related term in the mean-field single-

particle dispersion can be rewritten as

$$\sum_{\mathbf{p}} n_{\mathbf{p}} V(\mathbf{k} - \mathbf{p}) = \frac{1}{N_s} \sum_{\mathbf{p},j} U_j \cos[(\mathbf{k} - \mathbf{p}) \cdot \mathbf{e}_j] n_{\mathbf{p}}$$
$$= \frac{1}{2} \sum_{i} \frac{U_j}{J_j} [D_j \cos(\mathbf{k} \cdot \mathbf{e}_j) + \mathcal{J}_j \sin(\mathbf{k} \cdot \mathbf{e}_j)], \tag{4.23}$$

where we have defined

$$D_j = \frac{2 J_j}{N_s} \sum_{\mathbf{k}} n_{\mathbf{k}} \cos(\mathbf{k} \cdot \mathbf{e}_j), \tag{4.24}$$

analogously to $\mathcal{J}_j$. This D_j is a self-energy term that appears in the effective mean-field dispersion in the form of a shift of the hopping coefficients J_j. Lastly, writing the constant energy correction in terms of $\mathcal{J}_j$ and D_j, we find

$$\sum_{\mathbf{k},\mathbf{p}} n_{\mathbf{k}} n_{\mathbf{p}} V(\mathbf{k} - \mathbf{p}) = \frac{N_s}{4} \sum_{j} \frac{U_j}{J_j^2} (D_j^2 + \mathcal{J}_j^2). \tag{4.25}$$

Now we express F_{SC} as a function of the seven parameters $\mathcal{J}_j$, D_j, and N:

$$F_{\mathrm{SC}} = - N^2 V(\mathbf{0}) + \frac{N_s}{4} \sum_{j} \frac{U_j}{J_j^2} (\mathcal{J}_j^2 + D_j^2) - \frac{1}{\beta} \sum_{\mathbf{k}} \ln(1 + e^{-\beta \omega_{\mathbf{k}}}) \tag{4.26}$$

Minimising F_{SC} with respect to $\mathcal{J}_j$ yields

$$\mathcal{J}_j = \frac{2 J_j}{N_s} \sum_{\mathbf{k}} \frac{\sin(\mathbf{k} \cdot \mathbf{e}_j)}{1 + e^{\beta \omega_{\mathbf{k}}(\{\mathcal{J}_j\})}} = \frac{2 J_j}{N_s} \sum_{\mathbf{k}} n_{\mathbf{k}} \sin(\mathbf{k} \cdot \mathbf{e}_j), \tag{4.27}$$

which is exactly our definition from Eq. (4.12). For D, the 'gap equation' is also its definition, just like for $\mathcal{J}$ - here we see that demanding self-consistency of N, $\mathcal{J}_j$, and J_j has the same result as extremisation of F. Now all we have to do is solve the self-consistent set of equations. Given D_j and $\mathcal{J}_j$, we have to self-consistently solve

$$N = \sum_{\mathbf{k}} n_{\mathbf{k}} = \sum_{\mathbf{k}} \frac{1}{1 + e^{\beta \omega_{\mathbf{k}}(\{\mathcal{J}_j, D_j, N\})}}. \tag{4.28}$$

Note that we are not fixing the particle number: we are merely calculating the average value for N. The fixed quantity is still the chemical potential μ. To solve these equations, we employ numerical iteration: for an initial guess N_0, $\mathcal{J}_{j,0}$, and $D_{j,0}$, we calculate $N(N_0, \mathcal{J}_{j,0}, D_{j,0})$. Based on the outcome, we adjust our input values, until we reach $N(N_0, \mathcal{J}_{j,0}, D_{j,0}) = N_0$, etc. The results found are like those shown in fig. 4.6.

Effective mean-field dispersion relation

As anticipated in section 4.1, our theory predicts the appearance of staggered currents running around the elementary plaquettes of the lattice in an extended region of parameter space. Self-consistently solving for N, $\mathcal{J}_j$, and D_j yields two distinct extremal energy solutions, each of which breaks time-reversal symmetry and features the momentum-space imbalance discussed in section 4.1.2. The two solutions correspond to two chiralities for the currents, *i.e.* two directions in which they can run around the plaquettes. This degeneracy is reflected in the two different sign configuration of the three $\mathcal{J}_j$ that both minimise the mean-field free energy.

For the purposes of calculating the mean-field dispersion relation, we note that μ and $2NV(\mathbf{0})$ are constant shifts, which play a role in determining the overall population, but not the imbalance. The imbalance between the two 'Fermi pools' is directly visible in the mean-field dispersion relation introduced in Eq. (4.21b). The shape of the dispersion is determined by both the D_j, which form a simple addition to the hopping matrix elements J_j and thus only increase the energetic width of the dispersion relation, and the $\mathcal{J}_j$, which alter the relative depths of the minima:

$$
\begin{aligned}
\epsilon_{\mathbf{k}} &- UD \sum_j \cos(\mathbf{k} \cdot \mathbf{e}_j) - U\mathcal{J} \sum_j \sin(\mathbf{k} \cdot \mathbf{e}_j) \\
&= \sum_j [(2J_j - UD) \cos(\mathbf{k} \cdot \mathbf{e}_j) - U\mathcal{J} \sin(\mathbf{k} \cdot \mathbf{e}_j)] \\
&= \sum_j \sqrt{(2J_j - UD)^2 + (U\mathcal{J})^2} \cos(\mathbf{k} \cdot \mathbf{e}_j + \varphi_j),
\end{aligned}
\tag{4.29}
$$

where $\varphi_j = -\arctan[\mathcal{J}U/(2J_j - UD)]$. The combined effect of the terms related to each of the three lattice directions is a deepening of one minimum, while the other becomes more shallow. Fig. 4.6 shows $\omega_{\mathbf{k}}$ next to the corresponding momentum space density for $\mu = 1$, $U = 2$, and $T = 0.1$, all in units of J. Having established that the expected spontaneous symmetry
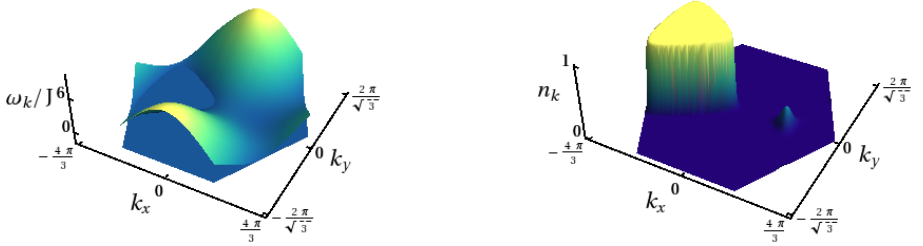
Figure 4.6: Left: $\omega_{\mathbf{k}}$; the $\omega_{\mathbf{k}} = 0$-plane is indicated. Right: corresponding momentum space density. This prediction is obtained for $\mu = 1$, $U = 2$, and $T = 0.1$, all in units of J. The filling factor is ≈ 0.15.

breaking phase does indeed occur, we now turn to the phase diagram.

4.2.2 Ginzburg-Landau expansion of free energy

In order to obtain phase boundaries and information about the order of the transition, let us perform a Ginzburg-Landau expansion of the free energy, with the currents $\mathcal{J}_j$ as three separate order parameters. The interaction will be taken to be isotropic, *i.e.* $U_j = U$. Eq. (4.26) gives the free energy, which will be Taylor-expanded in the currents $\mathcal{J}_j$, which constitute the order parameter for the time-reversal symmetry breaking transition. Let us start with the result, to second order:

$$F_{\text{SC}} \approx F^{(0)} + \begin{bmatrix} \mathcal{J}_1 & \mathcal{J}_2 & \mathcal{J}_3 \end{bmatrix} \begin{bmatrix} \alpha_{\text{SC}} & \gamma_{\text{SC}} & \gamma_{\text{SC}} \\ \gamma_{\text{SC}} & \alpha_{\text{SC}} & \gamma_{\text{SC}} \\ \gamma_{\text{SC}} & \gamma_{\text{SC}} & \alpha_{\text{SC}} \end{bmatrix} \begin{bmatrix} \mathcal{J}_1 \\ \mathcal{J}_2 \\ \mathcal{J}_3 \end{bmatrix}. \qquad (4.30)$$

Now let us calculate the coefficients, order by order. The first order vanishes due to the gap equation. The second order diagonal coefficients are all equal due to the symmetry of the problem, and given by

$$
\alpha_{\text{SC}} = \left.\frac{\partial^2 F_{\text{SC}}}{\partial \mathcal{J}_j^2}\right|_{\mathcal{J}_j=0} = \frac{N_{\text{s}}U}{2J_j^2} - U\frac{\partial}{\partial \mathcal{J}_j}\sum_{\mathbf{k}}\frac{1}{1+e^{\beta\omega_{\mathbf{k}}}}\underbrace{\left.\frac{\sin(\mathbf{k}\cdot\mathbf{e}_j)}{J_j}\right|_{\mathcal{J}_j=0}}_{g_{\mathbf{k}}^j}
$$
$$
= \frac{N_{\text{s}}U}{2J_j^2} - \frac{\beta U^2}{4}\sum_{\mathbf{k}}\left.\frac{(g_{\mathbf{k}}^j)^2}{\cosh^2(\beta\omega_{\mathbf{k}}/2)}\right|_{\mathcal{J}_j=0}. \tag{4.31}
$$

Next, let us consider mixing terms between the different currents. At second order, there are three of them, again all equal:

$$
\gamma_{\text{SC}} = \frac{\partial^2 F_{\text{SC}}}{\partial \mathcal{J}_j \partial \mathcal{J}_l} = -U^2\sum_{\mathbf{k}}\frac{g_{\mathbf{k}}^j g_{\mathbf{k}}^l}{\cosh^2(\beta\omega_{\mathbf{k}}/2)}. \tag{4.32}
$$

This quantity is always negative in the parameter regime explored here. Combining all second-order terms, we find Eq. (4.30). Given that γ_{SC} is always negative, diagonalising the matrix of second-order coefficients shows that the eigenvector with the lowest eigenvalue is given by $(1,1,1)$. A second-order phase transition is indicated by this lowest eigenvalue becoming negative, provided that the fourth-order terms are positive (as will be checked below). Hence, the state that minimises the free energy has all three currents present in equal measure, in such a way that there is no net current running through the system, as expected (see fig. 4.4). To finally obtain the phase boundary, we self-consistently solve the equations for the filling factor ν and the self-energy coefficient D_j, given by

$$
\nu = \frac{1}{N_{\text{s}}}\sum_{\mathbf{k}}n_{\mathbf{k}}(\nu, D_j)
$$
$$
D_j = \frac{2}{J_j N_{\text{s}}}\sum_{\mathbf{k}}n_{\mathbf{k}}\cos(\mathbf{k}\cdot\mathbf{e}_j)n_{\mathbf{k}}(\nu, D_j), \tag{4.33}
$$

and calculate the corresponding values for α_{SC} and γ_{SC}. Note that we do not need to self-consistenly calculate $\mathcal{J}_j$, since it vanishes on the phase boundary.

A remark on the validity of these results: The mean-field approximation can only be expected to be good as long as the contribution of the interaction energy does not exceed that of the kinetic energy. Hence, the important quantity is the ratio of the bandwidth over the average interaction energy per particle. The bandwidth is $6J$, and the average interaction energy per particle is $U\nu$, setting the validity condition at $U\nu < 6J$. The predicted phase boundary lies entirely within the domain where this condition holds, mostly due to the low densities required for this effect to occur. Thus, there is no evidence within this calculation that suggests the approximation is invalid. Of course, the assumptions that are made at the beginning limit the scope of potential outcomes: by not including *e.g.* spatially modulating terms, we have excluded the possibility of finding a density wave (this restriction will be lifted in section 4.3).

Higher-order terms

The Ginzburg-Landau expansion can be continued beyond second order. All third-order terms vanish, since they are all of third order in the functions $g_{\mathbf{k}}^j$, which is odd in $\mathbf{k}$; given that $\omega_{\mathbf{k}}$ is even (remember that the $\mathcal{J}_j$ are set to zero when evaluating the sum over the Brillouin zone), the combined summand is odd, and the entire sum vanishes. We show one example in equations:

$$\frac{\partial^3 F_{\mathrm{SC}}}{\partial \mathcal{J}_j^2 \partial \mathcal{J}_l} = -\frac{\beta U^2}{4} \sum_{\mathbf{k}} (g_{\mathbf{k}}^j)^2 \frac{\partial}{\partial \mathcal{J}_l} \frac{1}{\cosh^2(\beta \omega_{\mathbf{k}}/2)} \bigg|_{\mathcal{J}_j = \mathcal{J}_l = 0}$$
$$= \frac{\beta^2 U^3}{4} \sum_{\mathbf{k}} (g_{\mathbf{k}}^j)^2 g_{\mathbf{k}}^l \frac{\tanh(\beta \omega_{\mathbf{k}}/2)}{\cosh^2(\beta \omega_{\mathbf{k}}/2)} = 0. \tag{4.34}$$

For the fourth order, we obtain

$$\eta_{\mathrm{SC}} = \frac{1}{4!} \frac{\partial^4 F_{\mathrm{SC}}}{\partial \mathcal{J}_j^4} = \frac{\beta^3 U^4}{48} \sum_{\mathbf{k}} (g_{\mathbf{k}}^j)^4 \frac{1 - 2\sinh^2(\beta \omega_{\mathbf{k}}/2)}{\cosh^4(\beta \omega_{\mathbf{k}}/2)}, \tag{4.35a}$$

$$\zeta_{\text{SC}} = \frac{1}{(2!)^2} \frac{\partial^4 F_{\text{SC}}}{\partial \mathcal{J}_j^2 \mathcal{J}_l^2} = \frac{\beta^3 U^4}{32} \sum_{\mathbf{k}} (g_{\mathbf{k}}^l g_{\mathbf{k}}^j)^2 \frac{1 - 2\sinh^2(\beta\omega_{\mathbf{k}}/2)}{\cosh^4(\beta\omega_{\mathbf{k}}/2)}. \qquad (4.35b)$$

The other terms all contain odd-order derivatives of F_{SC} and consequently vanish. Given the two coefficients, the self-interaction η_{SC} and the intercurrent interaction ζ_{SC}, we have three questions to consider: Is η_{SC} positive or negative? Is ζ_{SC} positive or negative? And, lastly, which one has a larger absolute value? There are $2^3 = 8$ distinct possible ways to answer these questions. Let us go through the different realisations and their effects on how the staggered currents manifest themselves. Table 4.1 summarises the results, which are discussed in more detail below.

Situation	Coefficients	PB	TO	currents
1	$\eta_{\text{SC}} > 0, \zeta_{\text{SC}} > 0, \eta_{\text{SC}} > \zeta_{\text{SC}}$	same	2nd	isotropic
2	$\eta_{\text{SC}} > 0, \zeta_{\text{SC}} > 0, \eta_{\text{SC}} < \zeta_{\text{SC}}$	same	2nd	anisotropic
3	$\eta_{\text{SC}} > 0, \zeta_{\text{SC}} < 0, |\eta_{\text{SC}}| > |\zeta_{\text{SC}}|$	same	2nd	isotropic
4	$\eta_{\text{SC}} > 0, \zeta_{\text{SC}} < 0, |\eta_{\text{SC}}| < |\zeta_{\text{SC}}|$	changed	1st	isotropic
5	$\eta_{\text{SC}} < 0, \zeta_{\text{SC}} > 0, |\eta_{\text{SC}}| > |\zeta_{\text{SC}}|$	changed	1st	isotropic
6	$\eta_{\text{SC}} < 0, \zeta_{\text{SC}} > 0, |\eta_{\text{SC}}| < |\zeta_{\text{SC}}|$	changed	1st	anisotropic
7	$\eta_{\text{SC}} < 0, \zeta_{\text{SC}} < 0, \eta_{\text{SC}} < \zeta_{\text{SC}}$	changed	1st	isotropic
8	$\eta_{\text{SC}} < 0, \zeta_{\text{SC}} < 0, \eta_{\text{SC}} > \zeta_{\text{SC}}$	changed	1st	isotropic

Table 4.1: The different possibilities for the fourth-order terms in the Ginzburg-Landau expansion for the staggered current phase transition. Legend: PB = phase boundary (whether it is the same as the 2nd-order one or not), TO = transition order (first-order or second-order phase transition).

In case both η_{SC} and ζ_{SC} are positive, the fourth-order terms all result in energy penalties for large values of the order parameters. Hence, the phase transition remains continuous - as was assumed when performing the second-order calculation - and the phase boundary does not change relative to the second-order result. However, in case $\zeta_{\text{SC}} > \eta_{\text{SC}}$, *i.e.* the intercurrent

repulsion is stronger than the self-interaction, it is energetically favourable to for one current direction to have a larger weigth than the others, resulting in an anisotropic current pattern, as well as a net current running through the system. This situation (number 2 in table 4.1) does not occur within the parameter regime we are considering.

In case $\eta_{\mathrm{SC}} > 0$ but $\zeta_{\mathrm{SC}} < 0$, there are two very distinct cases depending on which one has a larger absolute value, although in both cases, the current pattern is isotropic, and no net current runs through the system. In case the self-interaction dominates, we have essentially the same situation as when the intercurrent interaction is weaker than the self-interaction but positive: the fourth-order terms have a net negative effect on the magnitude of the order parameters, the phase transition is continuous, and the phase boundary is the same as in the second-order calculation. This situation, number 3 in table 4.1, occurs for low temperatures and near the upper critical density. However, when the intercurrent attraction becomes stronger than the self-interaction, the combined effect of the fourth-order terms favours larger values for the order parameters, and the phase transition becomes discontinuous. In this case, the phase boundary also changes (the symmetry-broken region grows), as is generally the case when the combined fourth-order terms become negative. This situation, number 4 in table 4.1, occurs in a slightly smaller area than situation 3, for higher densities and lower temperatures. It is reflected in the phase diagram in the left panel of fig. 4.7 by the first-order transition that appears in the upper left corner. Note that in case the fourth-order terms favour larger values for the order parameters, yet higher orders are required to estimate the phase boundary.

The self-interaction η_{SC} does not become negative in the region of parameter space we have considered, although it does approach zero arbitrarily closely as $T \to 0$. However, in the interest of completeness, we will give a short discussion of what would happen in case it did, *i.e.* the last four situations described in table 4.1. In all of them, the transition is discontinuous and the phase boundary is different than the second-order calculation indicates. If the intercurrent interaction is repulsive, the system has an incentive to give one current direction a larger weight; however, if the ab-
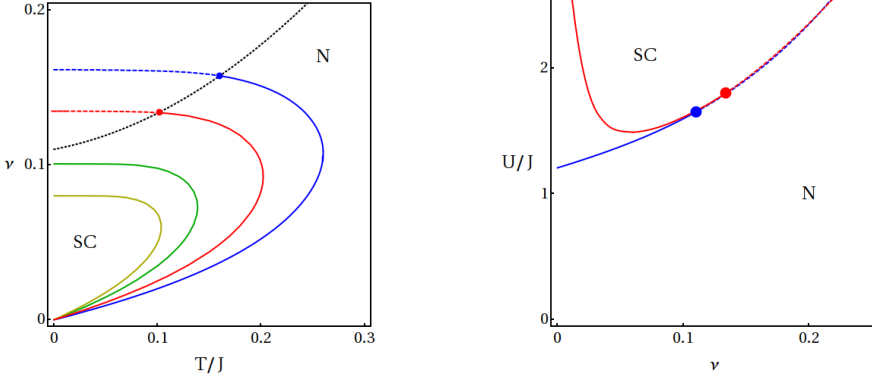
Figure 4.7: The phase diagram for the staggered currents. Left: filling ν versus dimensionless temperature T/J; interaction strengths used are $U/J = 1.5, 1.6, 1.8, 2.0$ (yellow, green, red, and blue lines, respectively). Smaller interaction strengths lead to smaller regions of parameter space where the currents occur. Dashed (solid) lines indicate a first- (second-)order phase transition. The big dots and dotted black line indicate where the transition order changes from first to second. Right: U/J versus ν; temperatures used are $T/J = 0, 0.1$ (blue and red, respectively). At $T = 0$, the currents occur for arbitrarily low filling factors. Dashed/solid lines indicate first/second order transition; the big dots indicate where the transition order changes. The only phases shown are the ones with staggered currents (SC) and without (N); for other phases, see sections 4.3 and 4.4. The phase boundary predicted by a second-order calculation is practically identical with the phase boundary predicted by the complete mean-field theory (not just the Ginzburg-Landau expansion): the difference is not visible on the plot. The difference is that the second-order calculation predicts a phase transition at marginally lower densities.

solute value of the self-interaction is larger than the intercurrent repulsion, *i.e.* $|\eta_{SC}| > |\zeta_{SC}|$, there is an effective energy penalty for making one order parameter smaller than the others, and all currents will be present in equal

measure. If $|\eta_{\mathrm{SC}}| < |\zeta_{\mathrm{SC}}|$, the intercurrent repulsion wins, and the current pattern will become anisotropic, like in situation 2 in table 4.1. Lastly, if both the self-interaction and the intercurrent interaction would be negative, all terms would favour larger values for all order parameters, resulting in a discontinuous transition and an isotropic current pattern.

In most of the domain where the mean-field approximation is valid, either situation 1 or situation 3 from table 4.1 occurs, and the transition is continuous. However, at low temperatures and densities near the upper critical density, the transition may become discontinuous. Hence, a tricritical point occurs in the high-density part of the staggered current phase boundary. However, since the magnitudes of the fourth-order coefficients in this region are significantly smaller than those of the second-order coefficients, the phase boundary shift is expected to be very small. Note that where the transition is first-order, the Ginzburg-Landau expansion does not give us the exact location of the phase boundary, unlike for second-order transitions. We have tested the phase boundary shift hypothesis at a few points by iteratively determining the exact mean-field prediction for the magnitude of $\mathcal{J}_j$, rather than relying on the Ginzburg-Landau expansion. We do indeed find that a first-order phase transition occurs where expected, with a very small shift in the phase boundary. The phase diagram is shown in fig. 4.7.

4.3   Density wave

In this section, we investigate the possibility of spontaneous density wave (DW) formation. As stated in section 4.1.2, repulsive NN (or longer-range) interactions can induce density waves even for spinless fermions. The traditional example of a fermionic density wave involves attractive interspecies on-site interactions for spin-$\frac{1}{2}$ fermions, where the system gains energy by increasing the on-site density. Here, the system gains energy by reducing the NN density, which also leads to modulations.

4.3.1 Mean-field assumption and order parameter

To calculate whether such a density modulation is energetically favourable, we simply go through the same motions as for the staggered current: calculate a mean-field Hamiltonian, obtain the corresponding free energy, and perform a Landau-Ginzburg expansion in the order parameters. However, for this calculation we use a different *ansatz*, which takes also takes into account spatially inhomogeneous terms. In addition to the $\langle c_{\mathbf{k}}^{\dagger} c_{\mathbf{k}} \rangle$-terms, we also assume nonzero values for

$$\left\langle c_{\mathbf{k} \pm \mathbf{Q}_j}^{\dagger} c_{\mathbf{k}} \right\rangle = n_{\mathbf{k}}^{\pm \mathbf{Q}_j}. \tag{4.36}$$

Hence, the expectation values with a number of different relative momenta will survive: $\mathbf{0}$ and $\{\mathbf{Q}_j\}$.

$$\left\langle c_{\mathbf{k}}^{\dagger} c_{\mathbf{p}} \right\rangle = n_{\mathbf{k}} \delta_{\mathbf{k},\mathbf{p}} + \sum_j \left(n_{\mathbf{k}}^{\mathbf{Q}_j} \delta_{\mathbf{k}-\mathbf{p},\mathbf{Q}_j} + n_{\mathbf{k}}^{-\mathbf{Q}_j} \delta_{\mathbf{k}-\mathbf{p},-\mathbf{Q}_j} \right). \tag{4.37}$$

The $\mathbf{Q}$'s selected for investigation are those where the nesting condition $\epsilon_{\mathbf{k}} \approx -\epsilon_{\mathbf{k}+\mathbf{Q}}$ is fulfilled in the vicinity of the Fermi surface. There are only three such cases in the shaken triangular lattice, all occurring near filling $\nu = 1/4$: $\mathbf{Q}_1 = (2\pi/a, 0)$, $\mathbf{Q}_2 = (-\pi/a, \sqrt{3}\pi/a)$, and $\mathbf{Q}_3 = (-\pi/a, -\sqrt{3}\pi/a)$ (see fig. 4.8). Since all of these vectors lie outside the first Brillouin zone, we map them to $\mathbf{Q}_1 = (0, 2\pi/\sqrt{3}a)$, $\mathbf{Q}_2 = (-\pi/a, -\pi/\sqrt{3}a)$, and $\mathbf{Q}_3 = (\pi/a, -\pi/\sqrt{3}a)$ under the reciprocal lattice symmetry.

4.3.2 Free energy expansion & degeneracy

The order parameter for the DW transition is the fraction of the density that modulates with the given wavevector:

$$\rho_j = \sum_{\mathbf{r}} n_{\mathbf{r}} \cos(\mathbf{r} \cdot \mathbf{Q}_j) = \sum_{\mathbf{r}} \left\langle c_{\mathbf{r}}^{\dagger} c_{\mathbf{r}} \right\rangle e^{i \mathbf{Q}_j \cdot \mathbf{r}}. \tag{4.38}$$

In the last step, we have made use of the fact that in the absence of the staggered currents discussed in the previous section, the density distribution
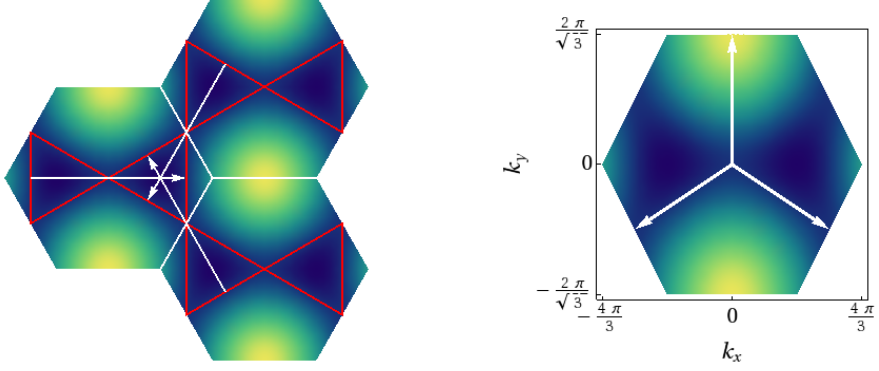
Figure 4.8: The nesting of the Fermi surface at filling $\nu = 1/4$. Right panel: the nesting vectors mapped to their equivalents within the first Brillouin zone.

is even. (For a discussion of the density wave in the presence of staggered currents, see section 4.5.) Like in the case of the staggered currents, we perform a Ginzburg-Landau expansion of the mean-field free energy in these order parameters. Since the required calculations are significantly more lengthy for the density wave, we present the details in an appendix, section A.1, and simply provide the main result here.

For each nesting vector, there are two important quantities: the modulating fraction ρ_j, which is the order parameter for the transition, and a self-energy term that we will name $D_{j,j}$ (see section A.1 for the details and rationale behind this name):

$$
\begin{aligned}
\rho_j &= \frac{1}{N_{\mathrm{s}}} \sum_{\mathbf{k}} \left\langle c^{\dagger}_{\mathbf{k}+\mathbf{Q}_j} c_{\mathbf{k}} \right\rangle \\
D_{j,j} &= \frac{1}{N_{\mathrm{s}}} \sum_{\mathbf{k}} \left\langle c^{\dagger}_{\mathbf{k}+\mathbf{Q}_j} c_{\mathbf{k}} \right\rangle \cos(\mathbf{k} \cdot \mathbf{e}_j).
\end{aligned}
\tag{4.39}
$$

This situation is very similar to the one found for the homogeneous density: as we saw in the calculations for the staggered currents, two quantities

always have finite magnitudes at the same time, namely the filling ν and the self-energy coefficient D_j. In the spatially modulated case we are investigating here, the modulating fractions ρ_j are analogous to the filling ν, and the self-energy coefficients $D_{j,j}$ to the self-energy coefficient D_j. In section 4.4, we will also investigate the spatially modulating analogue of the staggered currents $\mathcal{J}_j$. Note that while for the staggered currents, we calculated the mean-field predictions for the filling ν and the self-energy coefficient D_j exactly (within the mean-field approximation), here, we are only interested in the point where the modulating fractions ρ_j take finite values; for this purpose, the Ginzburg-Landau expansion will suffice.

In order to answer that question, we need the following free energy terms related to the density wave:

$$F_{\mathrm{DW}} = F^{(0)} + \sum_{j=1}^{3} \begin{bmatrix} \rho_j & D_j \end{bmatrix} \begin{bmatrix} \alpha_{\mathrm{DW}}^{\rho} & \gamma_{\mathrm{DW}} \\ \gamma_{\mathrm{DW}} & \alpha_{\mathrm{DW}}^{D} \end{bmatrix} \begin{bmatrix} \rho_j \\ \tilde{D}_j \end{bmatrix} \qquad (4.40)$$
$$+ \Gamma^{\rho} \rho_1 \rho_2 \rho_3.$$

Note that at second order in all parameters, the three directions decouple, leading to the conclusion that all three modulations are expected to be present in equal measure. Furthermore, at second order, it can be seen that finite values for the ρ_j are always accompanied by finite values for the $\tilde{D}_j$. A change of variables to the eigenbasis of the 2×2 matrices is not useful, however, since higher-order terms are not necessarily expressed most elegantly in that basis.

The most interesting aspect of this Ginzburg-Landau expansion is the unusual appearance of third-order terms. Normally, such terms vanish, since most calculations are performed with a single order parameter which has an arbitrary sign. In our case, however, a trilinear term can be composed that retains its sign under appropriate sign changes of the order parameters. None of the three single order parameters have a preferred sign, but they do have preferred sign configurations (*e.g.* all positive, or one positive and two negative, etc.).

Degeneracy

The preferred sign configurations due to the trilinear term in Eq. (4.40) leave some degeneracy, which calls for further discussion. A finite value of the order parameter ρ_j corresponds to having alternating rows of high and low density, with the alternation direction being parallel to the equivalent vector of $\mathbf{Q}_j$ within the first Brillouin zone (see fig. 4.8). Clearly, there are two ways to realise alternating rows of high and low density, given a particular direction; this corresponds to the fact that ρ_j can be positive or negative. If it is positive, the density at the point $(0, 0)$ is high, and vice versa. Since there are three vectors $\mathbf{Q}_j$, eight possible combinations exist. It can be seen by inspection that four of these eight have a unit cell with one high- and three low-density sites (see fig. 4.9), and the other four have the opposite (see fig. 4.10). The choice of sign configuration within the two sets of four corresponds to choosing which site in the larger (four-site) unit cell has a different density than the other three, and thus reflects the spatial symmetry breaking discussed in section 4.1.2.

Figure 4.9: The kagomé lattice of low-density sites resulting from a combination of the three DWs with equal weights. Red-circled sites have higher density. This DW is fourfold degenerate due to the freedom to choose the center of the unit cell. Compare to fig. 4.5: we find exactly the quarter-filling density wave pattern expected.

In our case, the interactions will favour the arrangement with one high-density site, thus limiting the degeneracy of the ground state to four. The low-density sites form a kagomé lattice. Once two of the sets of high-density rows have been chosen, the third is fixed by the interactions. Mathematically, this physical argument is expressed through the Γ-term, which par-
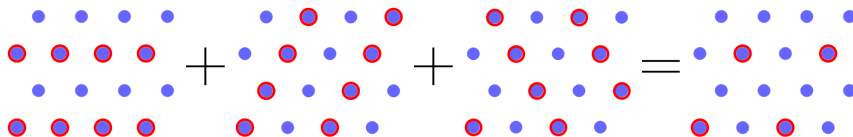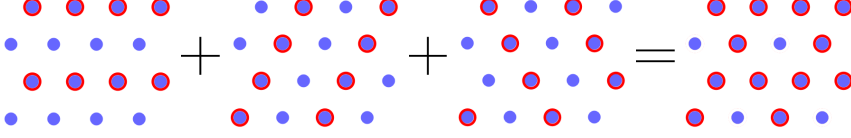
Figure 4.10: The kagomé lattice of high-density sites resulting from a combination of the three DWs with equal weights. This DW is fourfold degenerate due to the freedom to choose the center of the unit cell. It is energetically unfavourable, since it increases the number of NN pairs relative to a homogeneous density distribution.

tially lifts the degeneracy. Γ turns out to be negative, which implies that a positive sign is favoured for the product $\rho_1\rho_2\rho_3$. Such a situation corresponds to raising the density on one of the four sites in the unit cell while lowering it on the other three, as is indeed to be expected in a phase that breaks spatial symmetry to reduce the nearest-neighbour interaction energy. The presence of the other third-order terms (of order one to three in the $\tilde{D}_j$) does not affect this line of reasoning, since those terms are significantly smaller than the Γ^ρ-term.

Phase boundary shift / nature of the phase transition

The third-order term does two other things, beside reducing the eightfold degeneracy to fourfold: it induces a shift in the phase boundary, and renders the phase transition first order. Choosing the sign configuration where all $\rho_j > 0$ (any other of the four would also do, but this one is easiest to work with), and assuming that the higher-order terms favour all three DWs being present with equal magnitude, the terms from the Ginzburg-Landau expansion that involve only ρ's can be written as

$$F \approx F_0 + \frac{a|\rho|^2}{2} + \frac{b|\rho|^3}{3} + \frac{c|\rho|^4}{4}, \tag{4.41}$$

where $b < 0$ and $c > 0$. Extremising F from Eq. (4.41) with respect to $|\rho|$ yields

$$|\rho|(a + b|\rho| + c|\rho|^2) = 0. \tag{4.42}$$

The non-symmetry-broken solution $|\rho| = 0$ is always present. However, for small enough a, another real solution to Eq. 4.42 exists, which at $a = 0$ reduces to $|\rho| = -b/c$. The energy of this solution is given by

$$F \approx F_0 + \frac{b}{3}\left(-\frac{b}{c}\right)^3 + \frac{c}{4}\left(-\frac{b}{c}\right)^4 = F_0 - \frac{b^4}{12c^3} < F_0. \tag{4.43}$$

Around $a = 0$, this solution changes linearly with a. Hence, for small but positive a, it still has a lower energy than the $|\rho| = 0$ solution. As a consequence, breaking the spatial symmetry becomes favourable already before $a = 0$, and $|\rho|$ jumps to a finite value, rendering the transition first order. Schematic plots of $F(\rho)$ for various signs and relative magnitudes of a and b are shown in fig. 4.11.

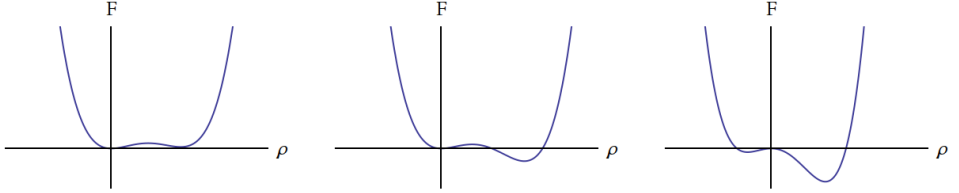Figure 4.11: Schematic plots of $F(\rho)$. Left: positive second-order coefficient ($a > 0$), negative but small third-order coefficient ($b < 0$); no phase transition. Center: positive second-order coefficient ($a > 0$), negative third-order coefficient ($b < 0$) large enough to drive a first-order phase transition. Right: negative second- and third-order coefficients ($a < 0$ and $b < 0$): the deepest minimum has a positive value for ρ.

4.3.3 Phase diagram

Due to the presence of two parameters for each of the three modulation directions (the modulating fraction ρ_j and the self-energy coefficient $D_{j,j}$), calculating all higher-order terms is beyond the scope of this project. Since an estimate of the magnitude of the phase boundary shift induced by the third-order terms requires knowledge of at least the fourth-, but possibly also fifth- and sixth-order terms, we will limit ourselves to the conclusions that a shift occurs and that the transition is driven first-order. In fig. 4.12, we present a phase diagram based on the quadratic terms from the Ginzburg-Landau expansion (*i.e.* where the transition is indicated by the second-order coefficient a turns negative), with a qualitative indication of the transition type and accuracy of the phase boundary location.

4.4 Modulated currents

In this section, we investigate a third type of symmetry breaking, that involves both spatial modulation and time-reversal symmetry breaking. Note, however, that it is *not* just a combination of the previous two phases discussed: it features a *qualitatively different* symmetry-broken state. It involves currents running through the system, but unlike those discussed in section 4.2, they are not spatially homogeneous, but modulate instead. Fig. 4.13 sketches the difference between the spatially homogeneous currents discussed in section 4.2 and the modulating ones here.

The main reason to look for a state that breaks both spatial and temporal symmetry is the tendency towards spatial symmetry breaking discussed in section 4.3, combined with the mechanism that led to time-reversal symmetry breaking in the homogeneous system. The effective momentum-space attraction is still present even in the density wave, but it favours different momentum-space density distributions than it does in the spatially homogeneous phase (this is related to the argument at the end of section 4.3 about the competition between the density wave and the staggered currents). This type of symmetry breaking is more complicated, and therefore less straightforward to generate an intuitive picture for, so we will sim-
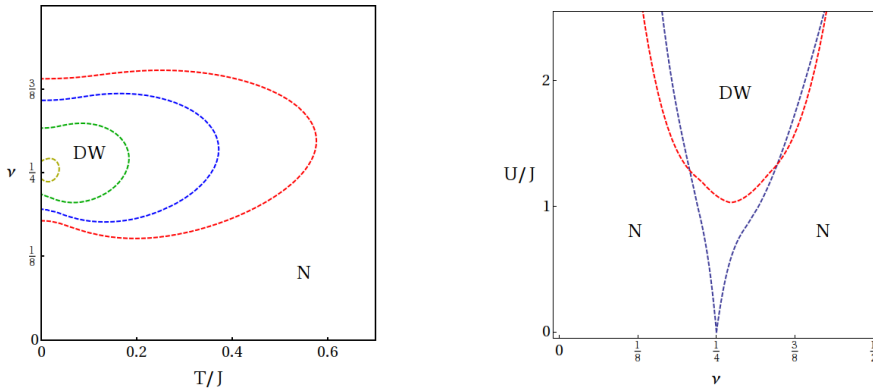
Figure 4.12: The phase diagram for the density wave. Left: ν versus T/J; interaction strengths used are $U/J = 0.5, 1.0, 1.5, 2.0$ (yellow, green, red, and blue lines, respectively). Smaller interaction strengths lead to smaller regions of parameter space where the density wave occurs. The dashing of the lines indicates a first-order phase transition. Right: U/J versus ν; temperatures used are $T/J = 0, 0.2$ (blue and red lines, respectively). At $T = 0$, the density wave occurs for arbitrarily weak interaction strengths. The only phases shown are the density wave (DW) and absence thereof (N); for the other phases investigated here, see sections 4.2 and 4.4.

ply investigate the time-reversal symmetry breaking contributions from the spatially modulating mean-field terms, which were neglected in section 4.3.

4.4.1   Spatially modulating current contributions

Spatially modulating one-particle correlation functions

In section 4.3, we have started our investigation from one-particle correlation functions of the form $\langle c_{\mathbf{k}+\mathbf{Q}}^{\dagger} c_{\mathbf{k}} \rangle$, but proceeded to take only some of
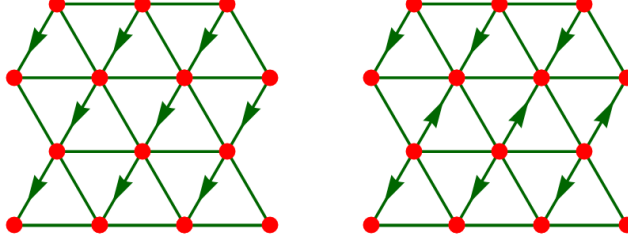
Figure 4.13: Left: the homogeneous currents along one particular lattice direction. Right: the modulated currents along the same lattice direction, modulated along $\mathbf{Q}_1 = (0, 2\pi/\sqrt{3}a)$. Note that only one current direction is depicted here, which by itself would violate the continuity equation. However, six such modulating currents will appear in the symmetry-broken phase, in such a combination that no density build-up or depletion takes place.

the Fourier components into account:

$$
\begin{aligned}
\rho_j &= \sum_{\mathbf{k}} \left\langle c_{\mathbf{k}+\mathbf{Q}_j}^\dagger c_{\mathbf{k}} \right\rangle e^{i\mathbf{k}\cdot\mathbf{0}} \\
D_{j,j} &= \mathrm{Re} \sum_{\mathbf{k}} \left\langle c_{\mathbf{k}+\mathbf{Q}_j}^\dagger c_{\mathbf{k}} \right\rangle e^{i\mathbf{k}\cdot\mathbf{e}_j}.
\end{aligned}
\tag{4.44}
$$

It is clear that a number of other Fourier components might also have finite values:

$$
\begin{aligned}
D_{j,l} &= \mathrm{Re} \sum_{\mathbf{k}} \left\langle c_{\mathbf{k}+\mathbf{Q}_j}^\dagger c_{\mathbf{k}} \right\rangle e^{i\mathbf{k}\cdot\mathbf{e}_l} \quad \text{with } j \neq l \\
\mathcal{J}_{j,j} &= \mathrm{Im} \sum_{\mathbf{k}} \left\langle c_{\mathbf{k}+\mathbf{Q}_j}^\dagger c_{\mathbf{k}} \right\rangle e^{i\mathbf{k}\cdot\mathbf{e}_j} \\
\mathcal{J}_{j,l} &= \mathrm{Im} \sum_{\mathbf{k}} \left\langle c_{\mathbf{k}+\mathbf{Q}_j}^\dagger c_{\mathbf{k}} \right\rangle e^{i\mathbf{k}\cdot\mathbf{e}_l} \quad \text{with } j \neq l.
\end{aligned}
\tag{4.45}
$$

In particular, it is noteworthy that even if $\mathcal{J}_{j,j}$ or $\mathcal{J}_{j,l}$ is finite, there is no need for ρ_j to also be finite. In other words, it is quite possible to have finite one-particle correlation functions $\langle c^\dagger_{\mathbf{k}+\mathbf{Q}} c_{\mathbf{k}} \rangle$ that break translational symmetry, without having a density wave.

Spatially modulating current contributions

As we have seen in Eq. (4.12), the currents are given by

$$\mathcal{J}_{\mathbf{r}-\mathbf{r}'} = 2J_{\mathbf{r}-\mathbf{r}'} \operatorname{Im} \left\langle c^\dagger_{\mathbf{r}} c_{\mathbf{r}'} \right\rangle. \tag{4.46}$$

However, in section 4.2, where that result was derived, only one-particle correlation functions corresponding to a spatially homogeneous density distribution were evaluated: $\langle c^\dagger_{\mathbf{k}} c_{\mathbf{p}} \rangle$ was assumed to be proportional to $\langle c^\dagger_{\mathbf{k}} c_{\mathbf{k}} \rangle \delta_{\mathbf{k},\mathbf{p}}$. In section 4.3, we introduced three extra terms to be taken into account. Applying the same strategy to the calculation of the currents, we Fourier transform and insert Eq. (4.37):

$$
\begin{aligned}
\mathcal{J}_{\mathbf{r}-\mathbf{r}'} = {} & 2J_{\mathbf{r}-\mathbf{r}'} \operatorname{Im} \sum_{\mathbf{k},\mathbf{p}} e^{i(\mathbf{k}\cdot\mathbf{r}-\mathbf{p}\cdot\mathbf{r}')} \left\langle c^\dagger_{\mathbf{k}} c_{\mathbf{p}} \right\rangle \\
= {} & J_{\mathbf{r}-\mathbf{r}'} \sum_{\mathbf{k}} \Bigg[2n_{\mathbf{k}} \sin[\mathbf{k}\cdot(\mathbf{r}-\mathbf{r}')] \\
& - i \sum_l \left\langle c^\dagger_{\mathbf{k}+\mathbf{Q}_l} c_{\mathbf{k}} \right\rangle \left(e^{i\mathbf{k}\cdot(\mathbf{r}-\mathbf{r}')} e^{i\mathbf{Q}_l\cdot\mathbf{r}} - e^{-i\mathbf{k}\cdot(\mathbf{r}-\mathbf{r}')} e^{i\mathbf{Q}_l\cdot\mathbf{r}'} \right) \Bigg] \\
= {} & \mathcal{J}_{\mathbf{r}-\mathbf{r}',0} + \sum_l \mathcal{J}_{\mathbf{r}-\mathbf{r}',\mathbf{Q}_l}.
\end{aligned}
\tag{4.47}
$$

Now, let us take a closer look, in real space, at what terms like $\mathcal{J}_{\mathbf{r}-\mathbf{r}',\mathbf{Q}_l}$ represent. Considering only the term where $l = 1$ (remember, $\mathbf{Q}_1 = (0, 2\pi/a\sqrt{3})$) from the last line of Eq. (4.47), and comparing the current from site $\mathbf{r}_0 = (0,0)$ to site $\mathbf{r}_1 = (1, \sqrt{3})a/2$ to the one from site $\mathbf{r}_1$ to site $\mathbf{r}_2 = (2, \sqrt{3})a$, we find:

$$\mathcal{J}_{\mathbf{r}_1-\mathbf{r}_0,\mathbf{Q}_1} = -\, i\, J_3 \sum_{\mathbf{k}} \left\langle c^\dagger_{\mathbf{k}} c_{\mathbf{k}-\mathbf{Q}_1} \right\rangle \left(e^{-i\mathbf{k}\cdot(\mathbf{r}_1-\mathbf{r}_0)} e^{i\mathbf{Q}_1\cdot\mathbf{r}_0} - e^{i\mathbf{k}\cdot(\mathbf{r}_1-\mathbf{r}_0)} e^{i\mathbf{Q}_1\cdot\mathbf{r}_1} \right)$$

$$= -i\, 2J_3 \sum_{\mathbf{k}} \left\langle c_{\mathbf{k}}^\dagger c_{\mathbf{k}-\mathbf{Q}_1} \right\rangle \cos(\mathbf{k} \cdot \mathbf{r}_1) \tag{4.48}$$

$$\mathcal{J}_{\mathbf{r}_2-\mathbf{r}_1,\mathbf{Q}_1} = i\, 2J_3 \sum_{\mathbf{k}} \left\langle c_{\mathbf{k}}^\dagger c_{\mathbf{k}-\mathbf{Q}_1} \right\rangle \cos(\mathbf{k} \cdot \mathbf{r}_1).$$

Here, we have made use of the fact that $\mathbf{Q}_1 \cdot \mathbf{r}_0 = 0$, that $\mathbf{Q}_1 \cdot \mathbf{r}_1 = \pi$, and that $\mathbf{Q}_1 \cdot \mathbf{r}_2 = 2\pi$. We conclude that the sign of the current contribution from $\langle c_{\mathbf{k}}^\dagger c_{\mathbf{k}+\mathbf{Q}_j} \rangle$ modulates with wavevector $\mathbf{Q}_j$. Note that due to this modulation, the current along any particular lattice vector is no longer constant across the system - the spatial homogeneity of the currents has been broken. If this current would appear by itself, it would violate the continuity theorem, as illustrated in fig. 4.14. However, when combined with similar contributions that modulate with the same wavevector but correspond to a different current direction, this violation disappears.

Next, let us consider the current from site $\mathbf{r}_0 = (0,0)$ to site $\mathbf{r}_3 = (1,0)$ and that from $\mathbf{r}_1$ to $\mathbf{r}_4 = (3, \sqrt{3})a/2$.

$$\mathcal{J}_{\mathbf{r}_3-\mathbf{r}_0,\mathbf{Q}_1} = -i\, J_1 \sum_{\mathbf{k}} \left\langle c_{\mathbf{k}}^\dagger c_{\mathbf{k}-\mathbf{Q}_1} \right\rangle \left(e^{-i\mathbf{k}\cdot(\mathbf{r}_3-\mathbf{r}_0)} e^{i\mathbf{Q}_1\cdot\mathbf{r}_0} - e^{i\mathbf{k}\cdot(\mathbf{r}_3-\mathbf{r}_0)} e^{i\mathbf{Q}_1\cdot\mathbf{r}_3} \right)$$

$$= 2J_1 \sum_{\mathbf{k}} \left\langle c_{\mathbf{k}}^\dagger c_{\mathbf{k}-\mathbf{Q}_1} \right\rangle \sin(\mathbf{k} \cdot \mathbf{r}_3) \tag{4.49}$$

$$\mathcal{J}_{\mathbf{r}_4-\mathbf{r}_1,\mathbf{Q}_1} = -2J_1 \sum_{\mathbf{k}} \left\langle c_{\mathbf{k}}^\dagger c_{\mathbf{k}-\mathbf{Q}_1} \right\rangle \sin(\mathbf{k} \cdot \mathbf{r}_3).$$

Hence, we conclude that the spatially inhomogeneous current contributions whose direction is parallel to the nesting vector, *i.e.* of the type $\mathcal{J}_{\mathbf{r}_3-\mathbf{r}_0,\mathbf{Q}_1}$, also modulate with the same wavevector, as was to be expected. It will turn out, however, that these contributions are energetically unfavourable in the parameter regime we are interested in.

4.4.2 Order parameters

In order to see whether these modulating currents are in fact energetically favourable, we once again revisit the mean-field free energy and perform
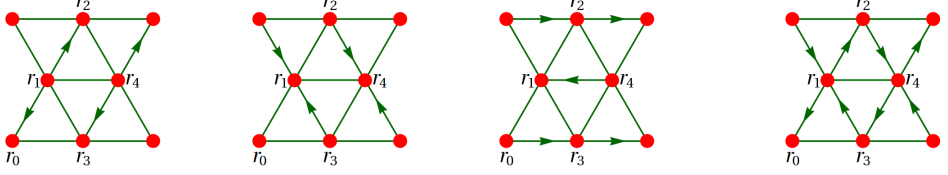
Figure 4.14: The current patterns that modulate with wavevector $\mathbf{Q}_1 = (0, 2\pi/\sqrt{3}a)$. From left to right: the contributions shown in Eq. (4.48); the analogue along lattice vector $\mathbf{e}_2$; the currents that run orthogonal to the direction in which they modulate; and the energetically favourable combination of the leftmost two images (see section 4.4.2).

yet another Ginzburg-Landau expansion. This time, we have to deal with nine different order parameters: there are currents along each of the three lattice directions that can modulate with each of the three nesting vectors. The details of the calculations are presented in appendix A.2; here we give the second-order terms:

$$F \approx F_0 + \sum_{j=1}^{3} \left(\lambda_{\mathrm{MC}} \mathcal{J}_{j,\mathbf{Q}_j}^2 + \begin{bmatrix} \mathcal{J}_{j',\mathbf{Q}_j} & \mathcal{J}_{j'',\mathbf{Q}_j} \end{bmatrix} \begin{bmatrix} \alpha_{\mathrm{MC}} & \gamma_{\mathrm{MC}} \\ \gamma_{\mathrm{MC}} & \alpha_{\mathrm{MC}} \end{bmatrix} \begin{bmatrix} \mathcal{J}_{j',\mathbf{Q}_j} \\ \mathcal{J}_{j'',\mathbf{Q}_j} \end{bmatrix} \right),$$

$$(4.50)$$

where j' and j'' are different from each other and from j. We see immediately that at second-order level, like in the case of the density wave analysis, terms corresponding to different nesting vectors $\mathbf{Q}_j$ decouple. Furthermore, it turns out that $\lambda_{\mathrm{MC}} > 0$ in the entire parameter regime investigated here, implying that, as mentioned above, contributions of the type $\mathcal{J}_{j,j}$ do not enter into the ground state. Hence, only the terms $\mathcal{J}_{j,l}$ with $j \neq l$ are of importance now. (Note that we are not investigating terms like $D_{j,l}$ as defined in Eq. (4.45), because they do not couple to any order parameters of interest, at least at second-order level.)

From the structure of the 2×2 matrix in Eq. (4.50), we may immediately conclude that $\mathcal{J}_{j,l}$ and $\mathcal{J}_{j,l'}$ (where $l \neq l'$ and $l, l' \neq j$) will take finite

values simultaneously, with equal magnitude and opposite sign, as long as $\gamma_{\mathrm{MC}} > \alpha_{\mathrm{MC}}$. An illustration is provided in the rightmost panel of fig. 4.14; fig. 4.15 shows the combined current pattern. It turns out that these currents do indeed occur, in a region of parameter space that largely overlaps with the density wave (see the phase diagram in fig. 4.16). The combined effect of the contributions related to all three nesting vectors adds up to a pattern of currents running around the triangular plaquettes of a kagomé lattice formed by removing one out of every four sites of the triangular lattice (see fig. 4.15). The expectation is that if both the density wave
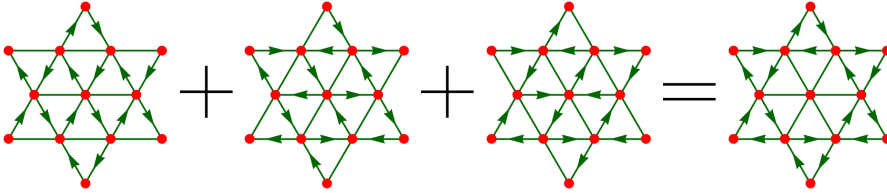
Figure 4.15: The modulated currents add up to a kagomé pattern. Different sign combinations for the three individual contributions lead only to a shifted pattern and/or reversed currents.

and the modulated currents are present, the kagomé lattice on which these currents appear will consist of the low-density sites in the DW phase. An intuitive physical argument can be made based on the continuity equation: If the currents do not avoid the high-density sites, their magnitude has to be adjusted to avoid net density build-up or depletion, *i.e.* violations of the continuity theorem. Since nothing in the Ginzburg-Landau coefficients suggests such an adaptation of the current strengths would be energetically favourable (the terms are identical for all current directions), and the continuity theorem can be satisfied by confining the currents to the low-density kagomé lattice, we have every reason to expect that this will indeed happen.

Degeneracy

Like in the case of the density wave, there are three order parameters governing the modulated currents (each consisting of a combination $(\mathcal{J}_{j,l}, -\mathcal{J}_{j,l'})$. Each of these three order parameters may take a positive or a negative sign, resulting in an eight-fold degeneracy. Unlike the density wave, however, this degeneracy is not expected to be lifted. To begin with, there is a four-fold degeneracy due to the fact that the unit cell of this phase contains four sites. The remaining two-fold degeneracy is related to the operation of changing the signs of all three order parameters. Now recall that in the case of the density wave, changing the signs of all three order parameters gave rise to a qualitatively different density distribution, since the numbers of high- and low-density sites were not equal. In the case of the modulated currents, however, changing the signs of all three order parameters simply inverts the directions of the currents, but does not alter their distribution or magnitude. Hence, we expect the eight-fold degeneracy for the modulated currents to remain in place.

The trilinear term that appears for the static density wave is required to partially lift the degeneracy of the three separate density modulation order parameters. Since this degeneracy is expected to remain present at the level where only the modulated currents are considered, all trilinear terms related to the modulated currents from the Ginzburg-Landau expansion are expected to vanish. This expectation is confirmed easily by considering the summand:

$$\Gamma^{\mathcal{J}} \propto \sum_{\mathbf{k}} \frac{\tanh(\beta\omega_{\mathbf{k}}/2)}{(\omega_{\mathbf{k}} - \omega_{\mathbf{k}+\mathbf{Q}_j})(\omega_{\mathbf{k}} - \omega_{\mathbf{k}+\mathbf{Q}_{j'}})} \sin(\mathbf{k}\cdot\mathbf{e}_1)\sin(\mathbf{k}\cdot\mathbf{e}_2)\sin(\mathbf{k}\cdot\epsilon_3) = 0,$$

$$(4.51)$$

since the fraction multiplying the sines is even, but the product of three sines itself is odd. However, there are some mixing terms between the modulated currents and the static DW at third-order level, that do not vanish; an example is

$$\Gamma^{\mathcal{J}\mathcal{J}\rho} \propto \sum_{\mathbf{k}} \frac{\tanh(\beta\omega_{\mathbf{k}}/2)}{(\omega_{\mathbf{k}} - \omega_{\mathbf{k}+\mathbf{Q}_j})(\omega_{\mathbf{k}} - \omega_{\mathbf{k}+\mathbf{Q}_{j'}})} \sin(\mathbf{k}\cdot\mathbf{e}_l)\sin(\mathbf{k}\cdot\mathbf{e}_{l'}). \quad (4.52)$$

Given a sign configuration for the density wave order parameters ρ_j, such trilinear terms as shown in Eq. (4.52) will lead to favoured sign configurations of the modulated currents. Evaluating the signs of those terms shows that as expected, the modulated currents will be confined to the low-density kagomé sublattice.

4.4.3 Phase diagram

Based on the second-order Ginzburg-Landau term, the modulated current phase is expected to occur in roughly the same region of parameter space as where the DW is expected. The modulated currents do not appear for arbitrarily weak interactions, unlike the DW (see fig. 4.16). The region where they occur grows faster than that of the DW as the interaction strength is increased. Around $U \approx 0.8J$, a region appears where the modulated currents are energetically favourable but the static DW is not. For strong enough interactions, the two time-reversal symmetry breaking patterns start to occur simultaneously in a small region at intermediate filling. The phase diagram is shown in fig. 4.16; see fig. 4.17 for a phase diagram that combines the different phases.

4.5 Summary and discussion of mean-field results

In sum, our mean-field analysis predicts three different symmetry-breaking phases. Fig. 4.17 shows two surfaces within the three-dimensional (T/J, ν, U/J) diagram, at $U/J = 2$ and at $T = 0$. For the simplest possible implementation of the above-mentioned system (a triangular lattice with frustrated hopping and nearest-neighbour interactions), we have found three different candidate phases breaking either translational symmetry, or time-reversal symmetry, or both. Since the different symmetry-breaking patterns are predicted to occur simultaneously in certain parameter ranges, a short discussion of such a combined phase follows below.
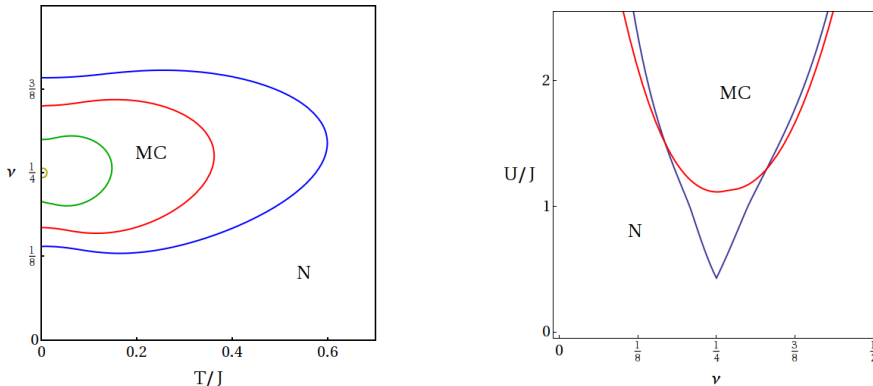
Figure 4.16: The phase diagram for the modulating currents. Left: ν versus T/J; interaction strengths used are $U/J = 0.5, 1.0, 1.5, 2.0$. Smaller interaction strengths lead to smaller regions of parameter space where the currents occur. The solid lines indicate a second-order phase transition. Right: U/J versus ν; temperatures used are $T/J = 0, 0.2$. At $T = 0$, the modulating currents occur for arbitrarily weak interaction strengths. The only phases shown are the ones with modulated currents (MC) and without (N); for the density wave and staggered currents, see sections 4.3 and 4.2, respectively.

Interaction between staggered currents and density wave

Since there are regions where the second-order theory predicts both the staggered currents and the density wave to be present, a natural question to ask is whether the two effects reinforce each other, or compete. Based on simple physical arguments, one expects competition: The staggered currents modify the shape of the Fermi surface, reducing the degree of nesting. Since the nesting condition implies that the density wave does not introduce large kinetic energy costs, combining the staggered currents and the density wave requires stronger interactions. Conversely, the density wave comes about because the interaction term couples momentum states near
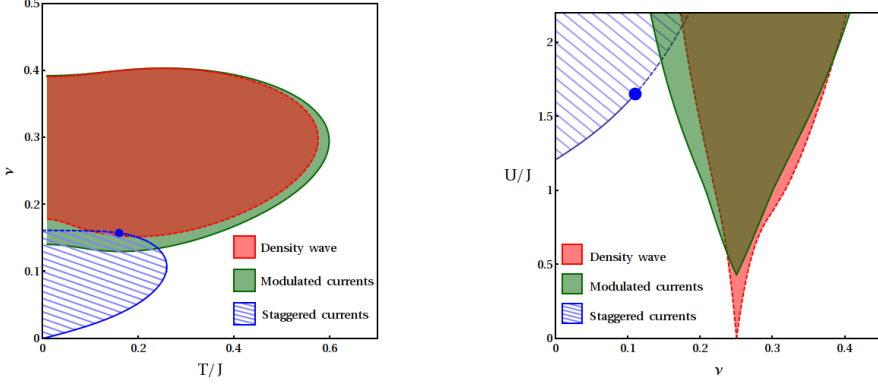
Figure 4.17: The combined phase diagram at $U/J = 2$ (left) and at $T = 0$ (right). Solid (dashed) lines correspond to second (first) order phase transitions. The large dot on the phase boundary for the staggered currents indicates the tricritical point, where the transition order changes.

the Fermi surface, thus delocalising the momentum-space density distribution and weakening the effect of the attractive momentum-space interaction discussed in section 4.1.2 (recall that it relied on a distribution localised around the two minima of the single-particle dispersion relation). Thus, the staggered currents are seen to be less favourable if a density wave is present.

To test this physical argument mathematically, we return to the free energy and consider interaction terms like $\rho_j^2 \mathcal{J}_l^2$ (lower orders vanish). The details of the calculations are presented in section A.1.4, but the main conclusion is that the combined coefficients of these terms are positive, which confirms our expectation. Quantitative statements on the effect this interaction has on the phase boundary require reliable estimates of the magnitude of the order parameters, which are unavailable for the density wave (see the discussion of the phase boundary above). A qualitative point worth remarking on is that since the density wave transition is first order (the arguments leading to that conclusion are unaffected by the interaction with

the staggered currents), the Ginzburg-Landau coefficient of the quadratic term for the staggered currents is expected to jump, when the density wave transition occurs. As a consequence, the phase transition for the staggered currents itself could also be driven first order, where it borders the density wave and is not already first order. It is indeed generally the case that a phase transition where one type of ordering disappears and another appears is first order. The two phases could also occur simultaneously, in which case the order of the staggered current transition is expected to be unaffected by the presence of the density wave.

Combination of staggered and modulating currents - trimerisation

It is interesting to note that the modulated currents add up to a pattern that is not staggered, but instead has the same current running around every triangular plaquette of the kagomé lattice. The hexagons of the kagomé lattice have twice the opposite current running around them. The staggered currents (see fig. 4.4) that occur at lower fillings, and compete with the DW, are also expected to compete with the modulated currents. Uniform density distributions are conserved by both current patterns. Combining them leads to a pattern of currents that breaks translational symmetry, where neighbouring triangles no longer have equal amounts of current running around them (see fig. 4.18). Although there is a region in parameter space where both current patterns are favourable based on simple, second-order Ginzburg-Landau considerations (see fig. 4.17), it is uncertain whether this combination will occur at all, since the two patterns should compete by the same mechanisms that lead to the repulsion between the staggered currents and the DW. The combined current pattern that would result from both phases occurring together, features a four-site unit cell, with different current magnitudes for each plaquette involved.

Given the predicted repulsion, the expectation is that where the staggered currents and the density wave or modulated currents overlap in parameter space, the phase boundary will shift, and no intermediate phase occurs. Of course, more quantitative analysis is needed to make more defi-
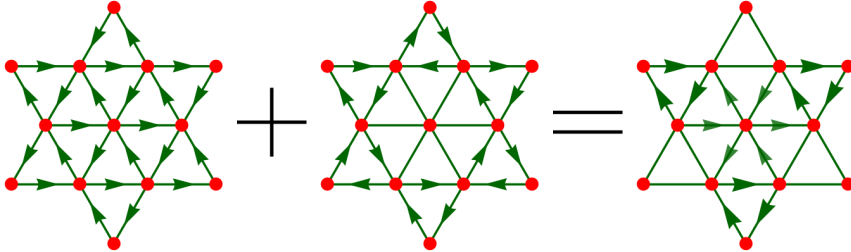
Figure 4.18: The staggered and modulating currents combined lead to a trimerised pattern. The size of the arrowheads indicates the relative current strenghts. Note that due to the expected competition between the two types of symmetry breaking, the occurrence of such a current pattern is actually relatively unlikely.

nite statements about this region - in case the predicted repulsion turns out to be very weak, it could be overcome by a sufficiently strong interparticle interaction U.

4.6   Exact diagonalisation of small systems

Although the mean-field results seem reasonable because they can be explained by simple intuitive physical arguments, an exact calculation is useful as a complementary study. We perform exact diagonalisations on small systems with periodic boundary conditions, to investigate whether the staggered currents appear in the ground state as predicted by the mean-field treatment done above. The main results are that the staggered currents do indeed occur more or less as predicted - there will always be some differences due to finite-size effects - and that a clear tendency towards density wave formation is observed. In the case of the density wave, certain finite-size effects are more persistent than in the staggered-current case, which can be understood from the fact that the density wave has a larger unit cell, and that therefore the diagonalised systems are effectively smaller for

the density wave than for the currents.

We describe the algorithms and code used in the appendix; see section A.3. Below, we discuss in detail the finite-size effects that play a role in our investigations, and the results obtained.

4.6.1 Finite-size effects

There are, of course, numerous finite-size effects that play a role in the exact diagonalisation. They come from two sources: the lattice we are using is finite, and the number of particles. The most general one, that plagues all exact diagonalisation studies, is that finite systems do not exhibit true phase transitions. Below, we discuss a number of effects that are specific to our investigation.

Discretisation gap of kinetic energy

In the non-interacting case, the finiteness of the lattice translates into a finite number of momentum eigenstates with discrete energies. This in turn leads to an effective gap for the occurrence of the staggered currents. The small size of the particle number adds to this gap, since it sets a minimum value for the current density: the smallest amount of current that can be produced is associated with transferring one particle to a momentum state with higher kinetic but lower interaction energy. If there are e.g. only four particles, states with small current densities are likely to be missed even if they are calculated to be favourable in the thermodynamic limit. Table 4.2 gives an illustration, albeit in a 3-particle scenario: in order to increase the staggered current density, the system has to go from partial to complete momentum space imbalance; there is no intermediate step.

Staggered current bias

If the number of particles is odd but the momentum states available are evenly distributed around the two spectrum minima, the kinetic energy cost to inducing staggered currents is much lower than if the number of particles is even. Considering the non-interacting case, it is easy to see

that there are two (or an integer multiple of two, if there are degenerate single-particle momentum states near the minima of the spectrum) degenerate ground states, and that both can be chosen to break time-reversal symmetry. In the case of an even number of particles, the degeneracy of the non-interacting ground states is only half that of the odd particle number case. This effect also disappears in the thermodynamic limit, since the current density induced by an imbalance of one particle between the two minima vanishes as the total particle number goes to infinity.

In order to minimise the discretisation gap of the kinetic energy, the lattice can be chosen such that the degeneracy of the single-particle momentum states is minimal (every energy around the minima will occur once for each minimum, so there is always some degeneracy). Furthermore, in case the ground state has a bias towards the presence of staggered currents, evidence for the system's tendency towards spontaneous time-reversal symmetry breaking can be found in the occurrence of additional imbalance between the two minima. See the figures in tables 4.2 and 4.3 for an illustration: the lowest-energy state in the non-interacting case already features momentum-space imbalance and therefore breaks time-reversal symmetry, as mentioned above. However, interactions favour a configuration as shown on the right, which is more imbalanced than the left one.

DW frustration and degeneracy

The finite size of the lattice, especially in combination with the periodic boundary conditions that are employed, can also frustrate the kagomé DW. To avoid this frustration, the lattice must be composed of four-site unit cells. Such a lattice never frustrates the staggered currents, since those are spatially homogeneous. For small enough systems (*e.g.* the smallest non-trivial one that does not frustrate the DW, 2×4 sites with 2 particles), states exist that simultaneously correspond to the absolute minimum of both the kinetic and the interaction energies (see section A.3.3; we will call them 'absolute minimal energy states'). Such states feature a density wave that is formed by superimposing momentum modes of minimal (and hence equal)

kinetic energy. The existence of these states is related to the degeneracy of the momentum eigenstates around the Fermi surface, which becomes less relevant as the system grows. At system sizes where this degeneracy effect becomes negligible, the calculational cost becomes prohibitive. Hence, this finite-size effect cannot be avoided in the current investigation. It should be noted that the absolute minimal energy states do feature density modulations, but not exactly of the type expected. However, at slightly larger systems (*e.g.* 4×4 sites with 4 particles), the density waves formed by the system are approaching the expected type more closely already.

4.6.2   Results

Staggered currents

Since exact diagonalisation can provide us with both the complete spectrum and the actual state, there are many ways to look for evidence of the predicted effects. For the staggered currents, we have chosen to investigate the energy spectrum. Here, we are showing results from a 5×9 lattice, described in table 4.2, with three particles, corresponding to a filling factor of 1/15 (recall that the staggered currents were predicted to occur for low fillings).

Fig. 4.19 shows the 10 lowest-energy states in the system described above (each state is doubly degenerate: mirroring a state in momentum space yields a different state with the same energy).

At zero interaction, the spectrum is easy to understand, since it is completely determined by the momentum eigenstates (the single-particle energies are shown in Table 4.2). The lowest-energy three-particle states can be shown to correspond to occupying the two lowest and first higher state; the two lowest and second higher; etc., as shown in Table 4.3. As soon as a weak interaction is switched on, certain states become energetically relatively more favourable. These turn out to be states that correspond to a higher imbalance than the necessary division of two particles in one minimum and one in the other, *i.e.* states with larger staggered currents. The non-interacting states from table 4.3 can be identified by comparing
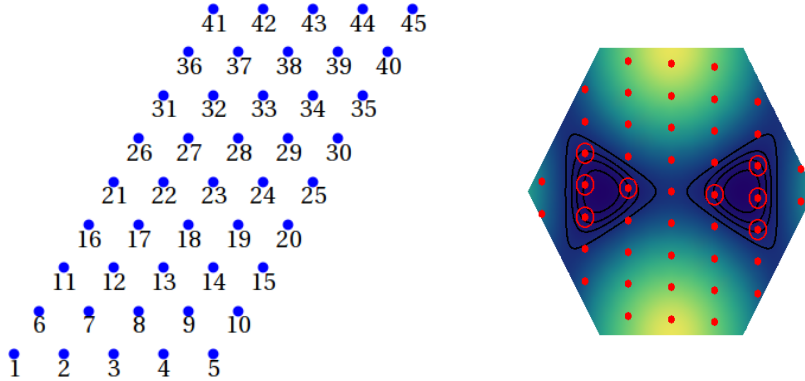
State	1	2	3	4	5	6	7	8
E_n	-2.842	-2.842	-2.666	-2.666	-2.610	-2.610	-2.445	-2.445

Table 4.2: Properties of the 5×9 lattice discussed in the text. Top left: real-space representation, with site numbering. Top right: corresponding single-particle spectrum with all momentum eigenstates indicated by red dots. The eight lowest energy states are circled. Bottom: table of the eight lowest single-particle eigenenergies.

energies. The eight-fold degeneracy of the fifth lowest in energy is lifted by the interactions, favouring the configuration shown on the right and its time-reversed counterpart. Of course, the interaction term mixes kinetic eigenstates, but the evolution of the various non-interacting states can easily be seen in the spectrum near $U/J = 3$ (see arrow).

Density wave

To find indications for the presence of a density wave, we have followed two strategies: simply evaluating the ground state density distribution, and investigating the degeneracy of the ground state. Based on the four-fold degeneracy of the density wave, one might expect a fourfold degenerate ground state. Considering the modulated currents, at high enough inter-
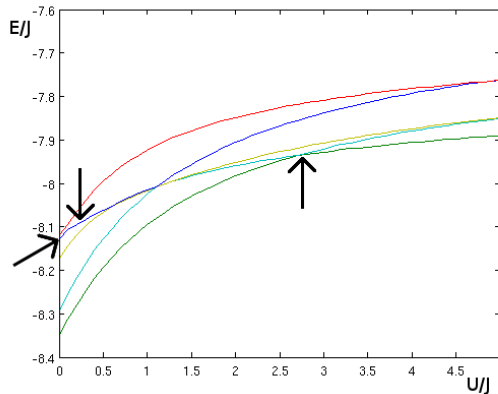
Figure 4.19: The 10 lowest energy states of the exact diagonalisation spectrum of a system of 5×9 lattice sites with 3 particles on them (every line is twofold degenerate). The energies are in units of J, and the interaction strength is plotted on the horizontal axis. The evolution of the state with maximal staggered current density from an excited state to the ground state can clearly be seen. The arrows indicate the interactions-driven process where states with larger staggered currents cross states with less: Without interactions, the maximal staggered current density has the highest energy in the plot. Almost immediately, it drops below the next highest energy state; near $U/J = 3$, it becomes the ground state.

actions one might even expect an eight-fold degeneracy. However, neither were found quite as expected: a density wave pattern is present, but different than the isotropic kagomé one that was predicted by the mean-field theory, and the ground state degeneracy is lower than the expected four to eight. One possible reason for these discrepancies is the existence of states that simultaneously minimise the kinetic and interaction energy, which are found in very small systems (e.g. 2×4 sites with 2 particles), where the lowest kinetic energy states have momenta that lie on the bowtie of the Fermi

Occupied	$\sum E$	Degeneracy
1,2,3	-8.350	2: 1,2,4
1,2,5	-8.294	2: 1,2,6
1,3,4	-8.175	2: 2,3,4
1,2,7	-8.129	2: 1,2,8
1,3,5	-8.119	8: (1/2),(3/4),(5/6)
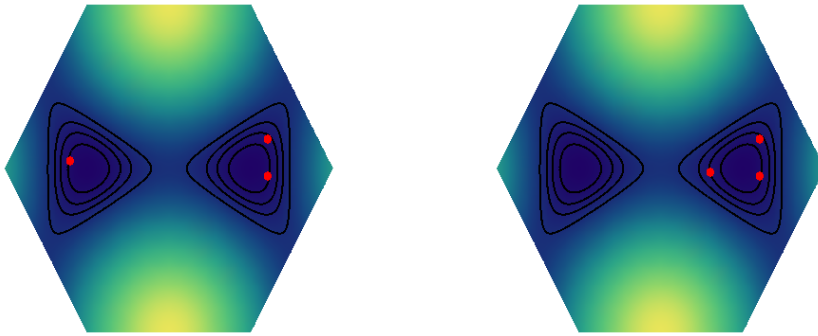
Table 4.3: Left: table of the energies of the lowest-energy non-interacting three-particle states in the 5×9 lattice. The degeneracy of each energy level is also listed, as are the occupied kinetic single-particle eigenstates for each three-particle state (see table 4.2). Center: one of the two lowest-energy non-interacting three-particle states represented in the first Brillouin zone. Right: one of the two states that evolve into the lowest-energy ones in the presence of a sufficiently strong interaction (see fig. 4.19) - with maximal staggered current density.

surface (see fig. 4.3 for the bowtie, and section A.3 for the density pattern). As the system size grows, momentum states are added at lower energies and the successors to these states no longer fully avoid the interaction, but still have most of their momentum-space density on the bowtie-shaped Fermi surface, simply because there are very few states located within the bowtie. The development towards the thermodynamic-limit situation where the mo-

mentum space density is not mainly (or only) located on the Fermi surface
is too slow for the system size to remain manageable. However, even these
states, which develop into the expected density wave at large enough sys-
tem sizes, already feature density waves, although slightly different from
the ones we expect.
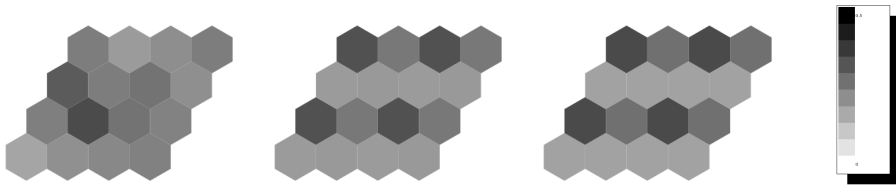
Figure 4.20: The density wave patterns found in the ground state of a 4×4
lattice with 4 particles, at various interaction strengths. Higher densities
are represented by darker coloring; the scale runs from 0 to 0.5 particles on
a site. Left: $U = 0$, no discernible order is present; the density fluctuations
are due to the large ground state degeneracy combined with the fact that
the algorithm randomly picks a superposition. Center: $U/J = 0.1$, some
density modulation is present. Right: $U/J = 1$, the modulation pattern
becomes stronger.

Fig. 4.20 shows the density patterns found in a lattice of 4×4 sites with
4 particles and periodic boundary conditions for $U/J = 0, 0.1$, and 1. Note
that the density wave spontaneously chooses a direction (the direction is
different for every diagonalisation, and has been aligned in the figures for
easier comparison). Another potential, although perhaps less plausible,
explanation is that the higher-order terms in the Ginzburg-Landau expan-
sion in fact lead to a preference for configurations where one nesting vector
dominates.

In conclusion, we see that although the exact diagonalisation studies
are plagued by finite-size effects, indications of the physics predicted by the
mean-field calculations are still present.

4.7 Realisations

The system discussed in this chapter has two ingredients: long-range interaction and kinetic frustration. Below, we discuss various ways of realising both ingredients in cold atomic gases loaded into optical lattices.

4.7.1 Long-range interactions

The main candidates for long-range interacting ultracold gases are dipolar atoms or heteronuclear molecules, which have both been discussed in the introductory chapters. The most relevant point for this chapter is the fact that they extend beyond nearest-neighbour: if, for example, the NN interaction strength is given by $U_{nn} = 2J$, then in a triangular lattice, the next-nearest neighbour interaction strength $U_{nnn} \approx 0.4J$. Such additional interaction terms have two effects: the effective attractive momentum-space interaction is renormalised, and interaction-assisted hopping processes beyond NN can be induced. If we can approximately ignore the extra hopping terms in the mean-field Hamiltonian, the only effect that remains is the possibility of stabilising more exotic density patterns by the additional interaction terms. If the additional hopping processes can not be ignored, more calculations are needed to assess the effects of the currents that could be induced between non-neighbouring sites.

In Ref. [37], a Bose-Fermi mixture was considered in the Mott-insulating regime. The bosons can be bound to the fermionic holes, and are then shown to have NN density-density interactions. Longer-ranged interactions are negligibly weak in this case, since the mechanism relies on second-order hopping processes. Hence, this realisation is attractive option as far as limiting the interaction-induced effects to the ones described here. The downside, however, is the extra experimental difficulty of creating a Bose-Fermi mixture loaded into the same lattice [53].

4.7.2   Kinetic frustration

Kinetic frustration in a triangular lattice can be achieved by inverting the band structure. To do so, one can change the sign of an odd number of hopping matrix elements, or study holes instead of particles.

As discussed in the introductory chapters, shaking the lattice allows one to modify the sign and magnitude of the hopping coefficients. This strategy has been applied successfully in one-dimensional [19] and cubic lattices [25], and recently in two-dimensional triangular ones as well (see Ref. [14, 10]). All experiments performed so far involve bosonic gases, but since the renormalisation of the hopping terms is a single-particle effect, it does not depend on particle statistics.

To obtain an expression for the Hamiltonian in terms of holes, we note that for a filling factor between 0 and 1, $n_h = 1 - n_p$, where n_h is the hole density and n_p is the particle density. Fourier transforming the hopping term and considering the interaction term in real space, we find

$$
\begin{aligned}
H &= \sum_{\mathbf{k}} \epsilon_{\mathbf{k}} n_{p,\mathbf{k}} + \sum_{\mathbf{r} \neq \mathbf{r'}} V(\mathbf{r} - \mathbf{r'}) n_{p,\mathbf{r}} n_{p,\mathbf{r'}} \\
&= \sum_{\mathbf{k}} \epsilon_{\mathbf{k}}(1 - n_{h,\mathbf{k}}) + \sum_{\mathbf{r} \neq \mathbf{r'}} V(\mathbf{r} - \mathbf{r'})(1 - n_{h,\mathbf{r}})(1 - n_{h,\mathbf{r'}}) \\
&= -\sum_{\mathbf{k}} \epsilon_{\mathbf{k}} n_{h,\mathbf{k}} + \sum_{\mathbf{r} \neq \mathbf{r'}} V(\mathbf{r} - \mathbf{r'}) n_{h,\mathbf{r}} n_{h,\mathbf{r'}} \\
&\quad + \underbrace{\sum_{\mathbf{k}} \epsilon_{\mathbf{k}} + \sum_{\mathbf{r} \neq \mathbf{r'}} V(\mathbf{r} - \mathbf{r'}) + 2 \sum_{\mathbf{r} \neq \mathbf{r'}} V(\mathbf{r} - \mathbf{r'}) n_{h,\mathbf{r}}}_{\text{constants}} .
\end{aligned}
\tag{4.53}
$$

We see that the sign of the dispersion is inverted, since the kinetic term is linear in the density, and that the sign of the interactions remains the same, since the interaction term is quadratic in the density. Another way of obtaining this result is to simply replace $c_{\mathbf{k}}^{\dagger} \to d_{\mathbf{k}}$ and $c_{\mathbf{k}} \to d_{\mathbf{k}}^{\dagger}$ where $d_{\mathbf{k}}^{\dagger}$ is the creation operator for a hole if the band-insulating state (filled band) plays the role of the vacuum. The inverted sign of the dispersion relation corresponds to inverting the sign of all three of the hopping coefficients

(remember, an odd number of hopping matrix elements has to have an inverted sign, so changing all three signs does the trick).

4.8   Summary

Summarising, we have shown that a kinetically frustrated lattice gas of single-species fermions with long-ranged density-density interactions features a rich phase diagram in the weakly interacting regime.

The analysis was performed based on a mean-field decomposition of the quartic interaction term in the lattice Hamiltonian. The order parameters for the various phases are single-particle observables constructed out of the correlation functions $\langle c_{\mathbf{k}}^{\dagger} c_{\mathbf{p}} \rangle$. An interesting aspect of all phases that were studied is the vectorial nature of the order parameters - three for each type of symmetry breaking, in the system under investigation. In the case of the density wave, the fact that three order parameters were present led to the appearance of a third-order term in the Ginzburg-Landau expansion, which drives the transition first order. This term plays clear role in the physical characterisation of the way the spatial symmetry is broken: it lifts the apparent degeneracy between two different types of density waves. The two time-reversal symmetry breaking phases do not feature such apparent degeneracies, and hence only even-order terms appear.

The time-reversal symmetry breaking manifests itself in the form of currents running through the system. Two distinct patterns occur in the kinetically frustrated triangular lattice, one mimicking the one found in Ref. [14] and one being confined to a kagomé sublattice. The latter occurs only if the Fermi surface is nested, and is therefore found in the vicinity of filling factor $\nu = 1/4$. It could be interpreted as the analogue of the spatially uniform staggered currents, occurring on the effective kagomé lattice that emerges as a consequence of the nested Fermi surface. A more thorough argument for this proposition would require a detailed study of the effective single-particle spectrum obtained after taking the symmetry-breaking single-particle correlators $\langle c_{\mathbf{k}+\mathbf{Q}}^{\dagger} c_{\mathbf{k}} \rangle$ into account. Interestingly, the currents on the kagomé sublattice also occur for densities slightly lower

than those required for the density wave itself.

The three phases interact and compete with each other, since there are regions in parameter space where two (or even all three) are predicted to occur simultaneously. The staggered currents can be expected to repel the two spatially symmetry-broken phases, as can be seen from intuitive physical arguments as well as mixing terms in the Ginzburg-Landau expansion of the free energy. The two spatially symmetry-broken phases, the density wave from section 4.3 and the modulated currents from section 4.4, couple to each other in a complicated way, due to the presence of third-order mixing terms. The large number of order parameters to be taken into account led evaluating all higher-order terms to be beyond the scope of the present project; hence, we do not have quantitative predictions on how the phase boundaries are affected by these interaction effects. There are, in principle, two main possibilities: either the different types of symmetry breaking repel each other, or they hybridise and occur simultaneously.

Additional support for the predicted symmetry breaking comes from exact diagonalisation studies. Finite-size effects prevent us from reproducing anything like a proper phase diagram, but clear indications for the occurrence of staggered currents are found in the low-energy spectrum. By comparing the exact low-energy spectrum to the momentum eigenstates and their energies, the eigenstates of the full Hamiltonian can be linked to non-interacting states, revealing which configurations in momentum space are most favourable with respect to the interaction energy. A tendency towards spatial symmetry breaking is also found, although not with the same degree of isotropy as expected based on the second-order Ginzburg-Landau expansion of the mean-field free energy. A number of possible explanations for this difference is given, based on finite-size effects in the exact diagonalisation studies, and higher-order terms in the Ginzburg-Landau expansion of the mean-field calculations.

Chapter 5

Supersolid phases of dipolar bosons in optical lattices with a staggered flux

Abstract

In this chapter[1], we present the theoretical mean-field zero-temperature phase diagram of a Bose-Einstein condensate (BEC) with dipolar interactions loaded into a square optical lattice with a staggered flux. Apart from uniform superfluid, checkerboard supersolid and striped supersolid phases, we identify several supersolids with staggered vortices. By allowing for different phases and densities on each of the four sites of the elementary plaquette, more complex configurations are found.

---

[1]This chapter is based on the publication *Supersolid phases of dipolar bosons in optical lattices with a staggered flux*, Phys. Rev. A **83**, 013627 (2011) by O. Tieleman, A. Lazarides, and C. Morais Smith.

5.1   Introduction

Supersolidity, a topic of long-standing interest in the condensed matter community, is commonly defined as the simultaneous presence of diagonal and off-diagonal long-range order in the system [44]. The most prominent candidate for experimental realisation is solid ^{4}He [89, 90]; other realisations have been suggested in the domain of ultracold atomic gases, such as rapidly rotating Fermi-Fermi mixtures [91] and dipolar bosonic gases in optical lattices [56]. In an optical lattice, one clearly has diagonal long-range order, since the density at the minima of the lattice potential is higher than at the maxima; however, this type of long-range order is imposed externally. To preserve the analogy to bulk supersolids, where the diagonal order is spontaneously present in the system, we define a supersolid in an optical lattice as a phase with both long-range off-diagonal and diagonal order, where the diagonal order breaks the translational symmetry of the lattice [92]. Recently, dipolar atoms or molecules in optical lattices have been predicted to feature such supersolidity. Refs. [59, 93] present analytical and numerical analyses of dipolar atoms in square lattices with only nearest-neighbour (NN) hopping. Other examples include square lattices with NN and next-nearest-neighbour hopping [94] and triangular lattices [92].

Uniform magnetic fields for ultracold atomic gases have been mimicked by applying rotation [95, 91] and by generating gauge fields using position-dependent optical coupling between internal states of the atoms [96, 97]. Analogous to superconductors in magnetic fields, these systems exhibit vortices. A staggered gauge field for neutral atoms has also been proposed [15], leading to a staggered-vortex superfluid phase [30]. In this chapter, we describe how a dipolar bosonic gas subjected to a staggered gauge field exhibits a supersolid phase which features vortices. In contrast to Ref. [91], we study the gas in a lattice and do not have a rotating trap.

We analyse the interplay between NN interactions and an artificial staggered magnetic field in a system of bosons in a two-dimensional square optical lattice. In order to perform this analysis, we generalise and combine the methods used in Refs. [56], [30], and [29], to allow for the description of phases with a higher degree of broken symmetry than discussed in those

three references. We present a phase diagram containing combinations of the uniform and staggered-vortex phases found in Ref. [30] and the super-solid phases found in Ref. [56], as well as a region, where two phases coexist and the system will phase separate. We find that several continuous and discontinuous phase transitions between different superfluid and supersolid phases can be driven in two ways: by changing the NN interaction strength or by changing the applied flux. Apart from the presence or absence of density modulations, we discuss the existence of another type of structure in the system, which arises when the many-body wavefunction exhibits phase differences between neighbouring lattice sites. The vortices studied in Refs. [30] and [29] are a realisation of a non-trivial, although relatively simple phase structure.

This chapter is structured as follows: In section 5.2, we introduce the system and briefly discuss its constituent components. In section 5.3, we present the methods used to determine the phase diagram, which is displayed and discussed in sections 5.4 and 5.5. In section 5.6 we show experimental signatures of the phases found. Section 5.7 concludes the chapter by summarizing and discussing the results.

5.2 The system

We consider a system of dipolar bosons in a two-dimensional square optical lattice [56] with staggered flux [29]. Below, we briefly explain the consequences of a staggered flux (section 5.2.1) and dipolar interactions in a lattice (section 5.2.2) for the phases found in the system. We work at $T = 0$ and consider only Bose-condensed phases, since we are interested in the combined effects of a staggered flux and NN interaction in a superfluid.

The Hamiltonian we investigate is

$$
\begin{aligned}
H &= H_{\text{flux}} + H_{\text{on}-\text{site}} + H_{\text{dip}} \\
&= -J \sum_{\mathbf{r}\in\mathcal{A},l} \left(e^{i(-1)^l\phi} a_{\mathbf{r}}^{\dagger} b_{\mathbf{r}+\mathbf{e}_l} + \text{H.c.} \right) + \frac{U}{2} \sum_{\mathbf{r}\in\mathcal{A}\oplus\mathcal{B}} n_{\mathbf{r}}(n_{\mathbf{r}}-1) \\
&\quad + \sum_{\mathbf{r}\in\mathcal{A}} \sum_{\sigma=\pm 1} \left(V_x n_{\mathbf{r}} n_{\mathbf{r}+\sigma\mathbf{e}_1} + V_y n_{\mathbf{r}} n_{\mathbf{r}+\sigma\mathbf{e}_2} \right).
\end{aligned}
\tag{5.1}
$$

Here, J represents the hopping strength between neighboring sites; ϕ is the phase picked up at each tunnelling process, which is related to the magnitude of the flux through a plaquette; U the on-site interaction strength; and V_x and V_y the anisotropic NN interaction strengths. The lattice is represented as two interspersed square sublattices, $\mathcal{A}$ and $\mathcal{B}$. The operators $a_{\mathbf{r}}$ ($a_{\mathbf{r}}^{\dagger}$) and $b_{\mathbf{r}'}$ ($b_{\mathbf{r}'}^{\dagger}$) are destruction (creation) operators acting on sites in the sublattices $\mathcal{A}$ and $\mathcal{B}$, respectively; note that there is only one type of particle being created and destroyed. The operator $n_{\mathbf{r}}$ is the number operator for site $\mathbf{r}$, irrespective of the sublattice in which it is located. The lattice vectors $\mathbf{e}_l$, $l \in \{1, 2, 3, 4\}$ are defined by $\mathbf{e}_1 = -\mathbf{e}_3 = \mathbf{e}_x$ and $\mathbf{e}_2 = -\mathbf{e}_4 = \mathbf{e}_y$.

5.2.1   Staggered flux

The term H_{flux} breaks the symmetry between the sublattices $\mathcal{A}$ and $\mathcal{B}$, as can be seen in Fig. 5.1(a). It can be represented as a synthetic magnetic field which alternates in sign between neighboring plaquettes. For the details of the derivation of this hopping term, we refer the reader to Refs. [30] and [15]. The phase diagram of bosons with on-site interactions in such a lattice is presented in Ref. [30]; we reproduce it in Fig. 5.1(b). The main conclusions from Ref. [30] which will be important for this chapter are the following: For strong on-site interactions (large U), a Mott-insulating phase is found. By reducing U, a second-order phase transition into a superfluid phase occurs at some critical value of U/J; the value of $(U/J)_c$ depends on ϕ as shown in Fig. 5.1(b). For $|\phi| < \pi/4$, *i.e.* small flux, the zero-momentum superfluid phase is unaltered; for $\pi/4 < |\phi| < 3\pi/4$, the system features a staggered-vortex superfluid phase, where the vortex cores are located at the centers of
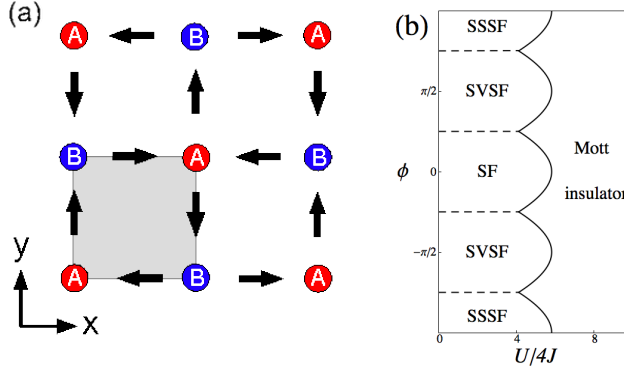
Figure 5.1: (a) The division into sublattices $\mathcal{A}$ and $\mathcal{B}$ caused by the staggered flux. (b) The phase diagram for bosons with on-site interactions in an optical lattice with staggered flux as found by the authors of Ref. [30] (for unit filling factor). Legend: SF = conventional superfluid; SVSF = staggered-vortex superfluid; SSSF = staggered-sign superfluid.

the plaquettes and the sign of the vorticity alternates between plaquettes. This phase comes about due to the development of a second minimum in the single-particle spectrum, at a finite momentum, which becomes the global minimum if $\pi/4 < |\phi| < 3\pi/4$. Condensation in this minimum introduces phase differences of $\pi/2$ between the lattice points, in such a pattern that a particle tunnelling around a plaquette picks up a phase of $\pm 2\pi$, depending on the direction of tunnelling and the plaquette. Note the periodicity in the ϕ-dependence of $(U/J)_c$. We find that the same periodic pattern emerges in the V_x-ϕ-diagrams that we present in sections 5.4 and 5.5, respectively, in spite of the fact that we are studying different phase transitions. We will confine ourselves to considering the weakly interacting limit, since our aim here is to study the interplay between the supersolidity found in Ref. [56] and the staggered-vortex patterns found in Ref. [30].

5.2.2   Dipolar interaction

As discussed in the introductory chapters, the interaction energy between two polarized dipoles is given by

$$v_{dd}(\mathbf{r}) = d^2 g_{dd} \frac{1 - 3\cos^2 \zeta}{r^3}, \tag{5.2}$$

where ζ is the angle between the polarisation axis and the displacement vector $\mathbf{r}$. Loading the dipoles into a deep lattice and approximating the dipolar interaction by cutting it off at NN distance, the only displacement vectors that we have to consider are $\mathbf{e}_1$ and $\mathbf{e}_2$, the lattice vectors in the x- and y-directions. The NN dipolar interaction strengths in the two relevant directions are given by

$$\begin{aligned}
V_x &= d^2 g_{dd} \frac{1 - 3\sin^2 \vartheta \cos^2 \varphi}{a^3}, \\
V_y &= d^2 g_{dd} \frac{1 - 3\sin^2 \vartheta \sin^2 \varphi}{a^3},
\end{aligned} \tag{5.3}$$

where a is the lattice spacing, ϑ is the inclination, and φ is the azimuthal angle. At $\varphi = \pi/4$, the interaction strength is isotropic and can be varied continuously from repulsive ($\vartheta = 0$) to attractive ($\vartheta = \pi/2$), being zero at $\vartheta = \sin^{-1}\sqrt{2/3}$. By varying the azimuthal angle, we can tune the ratio between V_x and V_y to any desired value. We note that tuning the NN interactions to zero will make the next-nearest-neighbor interactions more relevant; however, in this chapter, we focus on the regime where only the on-site and NN interactions are significant. By tuning U, ϑ and φ, we can cover the complete V_x/U-V_y/U-plane, providing us with complete control over the two relevant quantities for the purposes of our analysis. In the NN approximation, the Hamiltonian for the dipolar interaction thus takes the form

$$H_{\text{dip}} = \frac{1}{2} \sum_{\mathbf{r},\sigma=\pm 1} \left(V_x n_{\mathbf{r}} n_{\mathbf{r}+\sigma\mathbf{e}_1} + V_y n_{\mathbf{r}} n_{\mathbf{r}+\sigma\mathbf{e}_2} \right). \tag{5.4}$$

In Ref. [56], the phase diagram of dipolar bosons in a square optical lattice is presented, which we reproduce in Fig. 5.2 and briefly discuss here. At
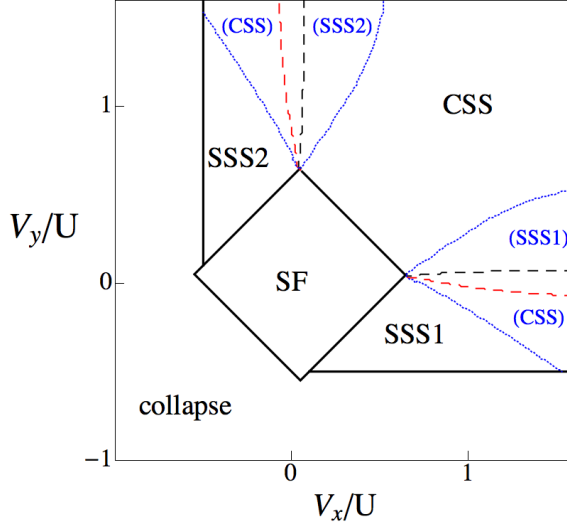
Figure 5.2: The phase diagram for dipolar bosons in a square optical lattice, at $J/(\nu U) = 0.1$. The black and blue lines were also found by the authors of Ref. [56]. Legend: SF = homogeneous superfluid, CSS = checkerboard supersolid, SSS = striped supersolid. SSS1 (SSS2) has the stripes in the y-(x-)direction. The solid black lines are second-order phase boundaries, the dashed black lines first-order phase transitions, and the dotted blue (grey) lines represent the existence of metastable states, which are labelled in blue (grey) and between brackets. The red (grey) dashed lines are our finding, and represent the SSS-CSS phase boundary for the case of strong flux, $\phi = \pi/2$; see the discussion in section 5.5.

mean-field-level, the authors identify three types of superfluid phases: a conventional superfluid one (SF), for weak NN interactions; one with a density modulation in a checkerboard pattern (checkerboard supersolid - CSS), for strong enough repulsive $V_x \approx V_y$; and one with a striped pattern (striped supersolid - SSS), where only one of the NN interaction parameters dominates. Both the checkerboard and striped superfluids have long-range

diagonal as well as off-diagonal order, *i.e.* they break both translational and local $U(1)$-gauge symmetry. These properties justify the epithet supersolid, as discussed in the introduction.

The checkerboard and striped phases are intuitively easy to understand. Consider the case where $V_x = V_y$: here, the NN interaction energy is reduced by arranging the atoms in a checkerboard-modulated density pattern, since there are fewer pairs of nearest neighbors in such a configuration. Similarly, if V_y is negative (or positive but small) and V_x is positive and of the order of U, the NN interaction energy is reduced by a striped configuration. As a final remark, taking longer-range interactions into account does affect the phase diagram to some extent, but the basic structure of checkerboard and striped phases remains intact [56].

5.3   The method: mean-field

Below, we explain how to obtain the phase diagram presented in sections 5.4 and 5.5. We use the Bogolyubov approximation to describe the condensate, which is justified if $J \gg U, V_x, V_y$ [56]; we calculate the ground state energies and excitation spectra of all the phases we identify. The excitation spectrum is required to check the dynamical stability of the phases we find: since we are dealing with bosons, a negative or complex excitation spectrum implies that the ground state above which the spectrum is calculated is not the real ground state of the system.

We will be working in the limit of high filling factor ν and strong hopping (or weak interaction), such that we can consider every lattice point to contain a condensate, and still have a small $J/(\nu U)$, where ν is the filling factor. The ratio $J/(\nu U)$ is required to be small for the density modulations to appear; if the energy gain from wavefunction overlaps between neighboring sites is too large, the system will ignore the NN interactions and simply remain in a superfluid state with homogeneous density.

5.3.1   Two-sublattice formalism

As described in section 5.2.1, the staggered flux divides the square lattice into two interpenetrating square sublattices, necessitating a two-sublattice description of the system, which is developed below. In the next subsection, we introduce another subdivision, into four sublattices, in order to allow for more complex density and phase distributions around the elementary plaquette.

We will perform our calculations in momentum space, where the grand-canonical version of the Hamiltonian given in Eq. (5.1) reads

$$
\begin{aligned}
H - \mu N = &\sum_{\mathbf{k} \in \mathrm{BZ}_1} \left(\epsilon_{\mathbf{k}} a_{\mathbf{k}}^\dagger b_{\mathbf{k}} + \mathrm{h.c.} - \mu a_{\mathbf{k}}^\dagger a_{\mathbf{k}} - \mu b_{\mathbf{k}}^\dagger b_{\mathbf{k}} \right) \\
&+ \sum_{\substack{\mathbf{k}_1,\dots,\mathbf{k}_4 \\ \in \mathrm{BZ}_1}} \left[\frac{U}{2N_{\mathrm{s}}} \left(a_{\mathbf{k}_1}^\dagger a_{\mathbf{k}_2}^\dagger a_{\mathbf{k}_3} a_{\mathbf{k}_4} + b_{\mathbf{k}_1}^\dagger b_{\mathbf{k}_2}^\dagger b_{\mathbf{k}_3} b_{\mathbf{k}_4} \right) \right. \\
&\left. + \frac{2V(\mathbf{k}_4 - \mathbf{k}_2)}{N_{\mathrm{s}}} a_{\mathbf{k}_1}^\dagger b_{\mathbf{k}_2}^\dagger a_{\mathbf{k}_3} b_{\mathbf{k}_4} \right] \delta_{\mathbf{k_1}+\mathbf{k_2}-\mathbf{k_3}-\mathbf{k_4},0},
\end{aligned}
\tag{5.5}
$$

with

$$
\begin{aligned}
\epsilon_{\mathbf{k}} = -4J \Bigg[&\cos(\phi) \cos\left(\frac{k_x + k_y}{2} a \right) \cos\left(\frac{k_x - k_y}{2} a \right) \\
&+ i \sin(\phi) \sin\left(\frac{k_x + k_y}{2} a \right) \sin\left(\frac{k_x - k_y}{2} a \right) \Bigg],
\end{aligned}
\tag{5.6}
$$

and

$$
V(\mathbf{k}) = V_x \cos(\mathbf{e}_x \cdot \mathbf{k}) + V_y \cos(\mathbf{e}_y \cdot \mathbf{k}).
\tag{5.7}
$$

N is the particle number operator for the entire system, μ is the chemical potential, N_{s} is the number of sites per sublattice, *i.e.* half the total number of sites, and BZ_1 is the first Brillouin zone. Now, we apply the Bogolyubov approximation: we replace $a_{\mathbf{k}} \to \delta_{\mathbf{k},\mathbf{c}} \langle a \rangle + \tilde{a}_{\mathbf{k}}$ and $b_{\mathbf{k}} \to \delta_{\mathbf{k},\mathbf{c}} \langle b \rangle + \tilde{b}_{\mathbf{k}}$, where $\mathbf{c}$ is the condensation momentum, and we treat $\tilde{a}_{\mathbf{k}}$ and $\tilde{b}_{\mathbf{k}}$ as small fluctuations relative to the average occupations $\langle a \rangle$ and $\langle b \rangle$. We then require that the

terms linear in the fluctuations vanish. This requirement yields the values for the chemical potential and, if present, the density modulation; for the details, see sections 5.4 and 5.5. The terms of order zero in the fluctuations represent the ground state energy per particle,

$$
\begin{aligned}
E_0 = {}& 2\mathrm{Re}(\epsilon_\mathbf{c} \langle a \rangle \langle b \rangle^*) + U(|\langle a \rangle|^4 + |\langle b \rangle|^4)/2N_\mathrm{s} \\
& + 2V(\mathbf{0})|\langle a \rangle|^2|\langle b \rangle|^2/N_\mathrm{s}.
\end{aligned}
\tag{5.8}
$$

The second-order terms can be diagonalised to give the excitation spectrum. They can be represented in matrix form as

$$
H^{\mathrm{ex}} = \frac{1}{2}\sum_{\mathbf{k}\in\mathrm{BZ}_1} A_\mathbf{k}^\dagger
\begin{bmatrix}
\omega_\mathbf{k} & \lambda_\mathbf{k} & \gamma_\mathbf{k} & \zeta_\mathbf{k} \\
\lambda_\mathbf{k}^* & \omega_\mathbf{k} & \zeta_\mathbf{k}^* & \gamma_\mathbf{k}^* \\
\gamma_\mathbf{k}^* & \zeta_\mathbf{k} & \omega_\mathbf{k} & \lambda_\mathbf{k} \\
\zeta_\mathbf{k}^* & \gamma_\mathbf{k} & \lambda_\mathbf{k}^* & \omega_\mathbf{k}
\end{bmatrix}
A_\mathbf{k} = \frac{1}{2}\sum_{\mathbf{k}\in\mathrm{BZ}_1} A_\mathbf{k}^\dagger M_\mathbf{k} A_\mathbf{k},
\tag{5.9}
$$

where

$$
A_\mathbf{k}^\dagger = \begin{bmatrix} a_\mathbf{k}^\dagger & a_{-\mathbf{k}} & b_\mathbf{k}^\dagger & b_{-\mathbf{k}} \end{bmatrix},
\tag{5.10}
$$

and $\omega_\mathbf{k}$, $\lambda_\mathbf{k}$, $\gamma_\mathbf{k}$, and $\zeta_\mathbf{k}$ are functions to be calculated for each specific phase we describe with this formalism. We diagonalise this quadratic Hamiltonian by solving

$$
\left(M_\mathbf{k} - \Omega_\mathbf{k}[A_\mathbf{k}, A_\mathbf{k}^\dagger]\right) = 0,
\tag{5.11}
$$

for $\Omega_\mathbf{k}$, which then is the excitation spectrum.

5.3.2   Four-sublattice description

The method presented above is in fact a simple combination of the approaches used in Refs. [56] and [30]. It works as long as either the phase distribution around the elementary plaquette is trivial (*i.e.* all sites have the same phase) or the density modulation is absent. If we allow $V_x \neq V_y$, striped or otherwise asymmetric phases may occur, in which case the four
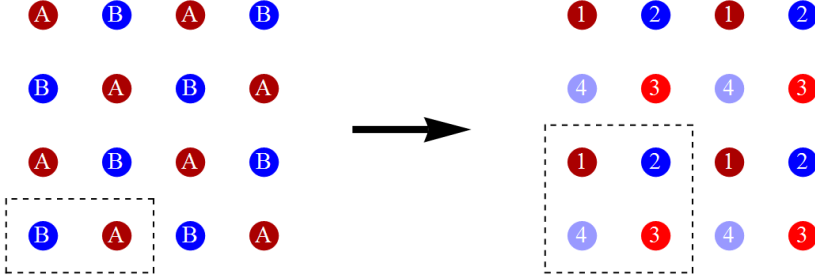
Figure 5.3: The two- and four-sublattice divisions of the square lattice.

sites of the elementary plaquette could all have different densities, or the phase drops could be distributed unevenly along the plaquette. In such phases, the two-sublattice formalism does not hold, since the density modulation and the phase pattern will influence each other, as we show below. One interesting phenomenon to be investigated here is the competition between NN interactions favouring stripes on the one hand, and a staggered flux on the other hand, since the staggered flux is associated with checkerboard-subdivision of the lattice (see section 5.2.1, Fig. 5.1). To investigate such phenomena, we need a description of the system which allows the condensate wavefunction to be different at all four sites of the elementary plaquette. Such a description involves four different sublattices: we have to split each of the sublattices $\mathcal{A}$ and $\mathcal{B}$ into two new ones, such that $\mathcal{A} = \text{SL}_1 \oplus \text{SL}_3$ and $\mathcal{B} = \text{SL}_2 \oplus \text{SL}_4$, as shown in Fig. 5.3. The resulting equations for the chemical potential and condensate wavefunction cannot be solved analytically, and have to be solved numerically instead. In this

representation, the momentum-space Hamiltonian becomes

$$H = \sum_{\mathbf{k} \in \mathrm{BZ}_1} \left(\epsilon_{\mathbf{k}}^x a_{1,\mathbf{k}}^\dagger a_{2,\mathbf{k}} + (\epsilon_{\mathbf{k}}^y)^* a_{1,\mathbf{k}}^\dagger a_{4,\mathbf{k}} + \epsilon_{\mathbf{k}}^x a_{3,\mathbf{k}}^\dagger a_{4,\mathbf{k}} + (\epsilon_{\mathbf{k}}^y)^* a_{3,\mathbf{k}}^\dagger a_{2,\mathbf{k}} \right) + \mathrm{h.c.}$$

$$- \mu \sum_{\mathbf{k} \in \mathrm{BZ}_1} \sum_{i=1}^4 a_{i,\mathbf{k}}^\dagger a_{i,\mathbf{k}} + \sum_{\mathbf{k}_1, \ldots, \mathbf{k}_4} \delta_{\mathbf{k}_1 + \mathbf{k}_2 - \mathbf{k}_3 - \mathbf{k}_4, 0} \left[\frac{U}{2N} \sum_{i=1}^4 a_{i,\mathbf{k}_1}^\dagger a_{i,\mathbf{k}_2}^\dagger a_{i,\mathbf{k}_3} a_{i,\mathbf{k}_4} \right.$$

$$+ \frac{2V_x}{N} \cos[(\mathbf{k}_4 - \mathbf{k}_2) \cdot \mathbf{e}_x] \left(a_{1,\mathbf{k}_1}^\dagger a_{2,\mathbf{k}_2}^\dagger a_{1,\mathbf{k}_3} a_{2,\mathbf{k}_4} + a_{3,\mathbf{k}_1}^\dagger a_{4,\mathbf{k}_2}^\dagger a_{3,\mathbf{k}_3} a_{4,\mathbf{k}_4} \right)$$

$$\left. + \frac{2V_y}{N} \cos[(\mathbf{k}_4 - \mathbf{k}_2) \cdot \mathbf{e}_y] \left(a_{1,\mathbf{k}_1}^\dagger a_{4,\mathbf{k}_2}^\dagger a_{1,\mathbf{k}_3} a_{4,\mathbf{k}_4} + a_{2,\mathbf{k}_1}^\dagger a_{3,\mathbf{k}_2}^\dagger a_{2,\mathbf{k}_3} a_{3,\mathbf{k}_4} \right) \right],$$

$$\tag{5.12}$$

where

$$\epsilon_{\mathbf{k}}^{x/y} = -2J \cos(k_{x/y} a) e^{i\phi}. \tag{5.13}$$

Note that this four-sublattice formalism can in principle be used to describe all the phases that we will encounter in the system, including the ones that can be analysed within the two-sublattice formalism; for example, the checkerboard-modulated phase without vortices has $\langle a_1 \rangle = \langle a_3 \rangle = \beta \langle a_2 \rangle = \beta \langle a_4 \rangle$, where β is a measure for the strenght of the modulation.

Bogolyubov approximation

In the four-sublattice description, the real space unit cell is twice as large as in the two-sublattice description. As a consequence, the first Brillouin zone is only half the size, and the number of bands in the excitation spectrum is doubled. The minimum in the corner of the first Brillouin zone found in Ref. [30] is mapped to the center of the new first Brillouin zone. Hence, the minimum of the single-particle spectrum in the four-sublattice description is always at $\mathbf{k} = 0$, and we use the mean-field ansatz $a_{j,\mathbf{k}} \to \delta_{\mathbf{k},0} \langle a_j \rangle + \tilde{a}_{j,\mathbf{k}}$. We obtain four equations for the chemical potential, of the form

$$\mu_1 = -2J \frac{e^{i\phi} \langle a_2 \rangle + e^{-i\phi} \langle a_4 \rangle}{\langle a_1 \rangle} + U \nu |\langle a_1 \rangle|^2$$

$$+ 2V_x \nu |\langle a_2 \rangle|^2 + 2V_y \nu |\langle a_4 \rangle|^2 \tag{5.14}$$

(we omit the other three for brevity; they can easily be deduced from the Hamiltonian). These four μ_j can be interpreted as the chemical potentials of the four sublattices, which are then thought of as macroscopic systems with an exchange mechanism (the hopping terms). The condition that all four chemical potentials are equal represents the equilibrium condition in this picture. Since the expression in Eq. (5.14) is in principle complex, we have to allow for complex $\langle a_j \rangle$ in order to be able to make the imaginary parts of the μ_j vanish. Representing $\langle a_j \rangle$ as $r_j e^{i\theta_j}$, the requirement that all μ_j are real yields the conditions

$$
\begin{aligned}
r_2 \sin \alpha_1 &= r_4 \sin \alpha_4 \\
r_3 \sin \alpha_2 &= r_1 \sin \alpha_1 \\
r_4 \sin \alpha_3 &= r_2 \sin \alpha_2 \\
r_1 \sin \alpha_4 &= r_3 \sin \alpha_3,
\end{aligned}
\tag{5.15}
$$

where $\alpha_j = \theta_{j+1} - \theta_j + \phi$. The four equations (5.15) can be reduced to three without loss of generality. A fourth equation comes from the requirement that the mean-field wavefunction is always single-valued. To satisfy this requirement, the phase picked up when hopping around a plaquette has to be an integer multiple of 2π; thus,

$$
\sum_i \alpha_i - 4\phi = 2\pi n,
\tag{5.16}
$$

where n determines the vorticity pattern of the system. Apart from Eqs. (5.15), we also have the real parts of the chemical potentials, which have to be equal to each other. They take the form

$$
\begin{aligned}
\mu_1 = &-\frac{2J}{r_1}\left(r_2 \cos \alpha_1 + r_4 \cos \alpha_4\right) + U\nu r_1^2 \\
&+ 2V_x \nu r_2^2 + 2V_y \nu r_4^2,
\end{aligned}
\tag{5.17}
$$

and similar expressions for μ_2, μ_3 and μ_4. Finally, there is the normalisation condition,

$$
r_1^2 + r_2^2 + r_3^2 + r_4^2 = 4,
\tag{5.18}
$$

bringing us to a total of eight equations in eight unknowns. Of course, more than one unique solution may still exist. We have to find all unique solutions, since each represents a different phase of the system, and we want to compare all phases for stability and ground state energy. Hence, we solve the eight equations Eqs. (5.15)-(5.18) numerically, in such a way that we find all solutions. Having found the $\langle a_j \rangle$, the ground state energy is given by

$$
\begin{aligned}
E_0 = & -4J \operatorname{Re} \sum_j e^{i\phi} \langle a_j \rangle^* \langle a_{j+1} \rangle + \frac{U}{2N} \sum_j |\langle a_j \rangle|^4 \\
& + \frac{2V_x}{N_s} \left(|\langle a_1 \rangle|^2 |\langle a_2 \rangle|^2 + |\langle a_3 \rangle|^2 |\langle a_4 \rangle|^2 \right) \\
& + \frac{2V_y}{N_s} \left(|\langle a_1 \rangle|^2 |\langle a_4 \rangle|^2 + |\langle a_3 \rangle|^2 |\langle a_2 \rangle|^2 \right),
\end{aligned}
\tag{5.19}
$$

where j is to be taken modulo 4.

Excitation spectrum

As before, finding all solutions that represent equilibrium situations is not enough: we also have to investigate their excitation spectra to assess their respective dynamical stabilities. In order to derive the excitation spectra, we collect all terms of second order in the fluctuations, and obtain, quite generally,

$$
\begin{aligned}
H_{\text{ex}}^{4\text{sl}} = \frac{1}{2} \sum_{\mathbf{k} \in \text{BZ}_1} \sum_{i,j} & \Big[\omega_{\mathbf{k}}^{ij} a_{i,\mathbf{k}}^\dagger a_{j,\mathbf{k}} + \omega_{\mathbf{k}}^{ji} a_{j,\mathbf{k}}^\dagger a_{i,\mathbf{k}} \\
& + (\lambda_{\mathbf{k}}^{ij})^* a_{i,\mathbf{k}}^\dagger a_{j,-\mathbf{k}}^\dagger + \lambda_{\mathbf{k}}^{ij} a_{i,\mathbf{k}} a_{j,-\mathbf{k}} \Big],
\end{aligned}
\tag{5.20}
$$

where

$$
A_{\mathbf{k}}^\dagger = \begin{bmatrix} a_{1,\mathbf{k}}^\dagger & a_{1,-\mathbf{k}} & a_{2,\mathbf{k}}^\dagger & a_{2,-\mathbf{k}} & a_{3,\mathbf{k}}^\dagger & a_{3,-\mathbf{k}} & a_{4,\mathbf{k}}^\dagger & a_{4,-\mathbf{k}} \end{bmatrix}.
\tag{5.21}
$$

In our specific case, ω^{ii} and λ^{ii} do not depend on $\mathbf{k}$: they are given by

$$\omega_{\mathbf{k}}^{11} = 2U|\langle a_1\rangle|^2 + 2V_x|\langle a_2\rangle|^2 + 2V_y|\langle a_4\rangle|^2 - \mu$$
$$\omega_{\mathbf{k}}^{22} = 2U|\langle a_2\rangle|^2 + 2V_x|\langle a_1\rangle|^2 + 2V_y|\langle a_3\rangle|^2 - \mu$$
$$\omega_{\mathbf{k}}^{33} = 2U|\langle a_3\rangle|^2 + 2V_x|\langle a_4\rangle|^2 + 2V_y|\langle a_2\rangle|^2 - \mu \qquad (5.22a)$$
$$\omega_{\mathbf{k}}^{44} = 2U|\langle a_4\rangle|^2 + 2V_x|\langle a_3\rangle|^2 + 2V_y|\langle a_1\rangle|^2 - \mu$$
$$\lambda_{\mathbf{k}}^{ii} = U(\langle a_i\rangle^*)^2.$$

The hopping terms have the following coefficients:

$$\omega_{\mathbf{k}}^{12} = (\omega_{\mathbf{k}}^{21})^* = \epsilon_{\mathbf{k}}^x + 2V_x\cos(k_xa)\,\langle a_1\rangle\,\langle a_2\rangle^*$$
$$\omega_{\mathbf{k}}^{23} = (\omega_{\mathbf{k}}^{32})^* = \epsilon_{\mathbf{k}}^y + 2V_y\cos(k_ya)\,\langle a_2\rangle\,\langle a_3\rangle^*$$
$$\omega_{\mathbf{k}}^{34} = (\omega_{\mathbf{k}}^{43})^* = \epsilon_{\mathbf{k}}^x + 2V_x\cos(k_xa)\,\langle a_3\rangle\,\langle a_4\rangle^*$$
$$\omega_{\mathbf{k}}^{41} = (\omega_{\mathbf{k}}^{14})^* = \epsilon_{\mathbf{k}}^y + 2V_y\cos(k_ya)\,\langle a_4\rangle\,\langle a_1\rangle^* \qquad (5.22b)$$
$$\omega_{\mathbf{k}}^{13} = (\omega_{\mathbf{k}}^{13})^* = 0$$
$$\omega_{\mathbf{k}}^{24} = (\omega_{\mathbf{k}}^{24})^* = 0.$$

Lastly, the off-diagonal mixing terms read

$$\lambda_{\mathbf{k}}^{12} = \lambda_{\mathbf{k}}^{21} = 2V_x\cos(k_xa)\,\langle a_1\rangle^*\,\langle a_2\rangle^*$$
$$\lambda_{\mathbf{k}}^{23} = \lambda_{\mathbf{k}}^{32} = 2V_y\cos(k_ya)\,\langle a_2\rangle^*\,\langle a_3\rangle^*$$
$$\lambda_{\mathbf{k}}^{34} = \lambda_{\mathbf{k}}^{43} = 2V_x\cos(k_xa)\,\langle a_3\rangle^*\,\langle a_4\rangle^*$$
$$\lambda_{\mathbf{k}}^{41} = \lambda_{\mathbf{k}}^{14} = 2V_y\cos(k_ya)\,\langle a_4\rangle^*\,\langle a_1\rangle^* \qquad (5.22c)$$
$$\lambda_{\mathbf{k}}^{13} = \lambda_{\mathbf{k}}^{21} = 0$$
$$\lambda_{\mathbf{k}}^{24} = \lambda_{\mathbf{k}}^{21} = 0.$$

As before, we diagonalise this Hamiltonian by numerically solving

$$\left(M_{\mathbf{k}}^{4\mathrm{sl}} - \Omega_{\mathbf{k}}^{4\mathrm{sl}}[A_{\mathbf{k}}, A_{\mathbf{k}}^\dagger]\right) = 0 \qquad (5.23)$$

for $\Omega_{\mathbf{k}}^{4\mathrm{sl}}$, which then gives the excitation spectrum.

In most regions of parameter space, there is only one dynamically stable phase. However, there are some regions where two phases are dynamically stable; here, we compare the ground state energies (which are equal to the free energies, since we are working at $T = 0$) to see which phase is favoured.

The phase diagram we find is, in principle, three-dimensional, since we have the three parameters ϕ, V_x and V_y. In addition to the V_x/U-V_y/U-diagram at $\phi = 0$ from Ref. [56], we present three cross sections which together form a representative sample of the results: the V_x-ϕ-diagram at $V_y = V_x$, the V_x-ϕ-diagram at $V_y = 0$, and the V_x/U-V_y/U-diagram at $\phi = \pi/2$.

5.4   Quantum phases: symmetric case

In this section, we discuss the symmetric case, where the NN interaction is equally strong in both directions. This can be achieved by polarising the dipoles perpendicular to the plane, or at an angle of $\pi/4$ relative to the in-plane lattice vectors. By tuning the inclination, the ratio $V_{x/y}/U$ can be tuned without changing U. However, if this technique is employed, the next-nearest-neighbor interactions will not be isotropic; this is only the case if the polarisation axis is perpendicular to the plane. As a consequence, the description presented here will be more accurate if the dipoles are polarised perpendicularly to the plane.

5.4.1   Weak flux: no vortices

For small values of the flux, $0 \leq |\phi| \leq \pi/4$, the system does not feature any vortices in the ground state. It may still exhibit density modulations, since these are caused by the NN interactions.

Superfluid: homogeneous density

For homogeneous or checkerboard-modulated density distributions, we can use the two-sublattice formalism, and replace $a_{\mathbf{k}} \rightarrow \delta_{\mathbf{k},0} \langle a \rangle + \tilde{a}_{\mathbf{k}}$ and $b_{\mathbf{k}} \rightarrow \delta_{\mathbf{k},0} \langle b \rangle + \tilde{b}_{\mathbf{k}}$. If the density is homogeneous, we have a conventional

superfluid (SF) and $|\langle a \rangle| = |\langle b \rangle| = \sqrt{N_{\mathrm{p}}/2}$, with N_{p} being the total number of particles in the system. Setting the term linear in the fluctuations zero yields

$$\mu_{\mathrm{SF}} = \epsilon_0 + \nu(U + 2V_x + 2V_y). \tag{5.24}$$

Note that $\epsilon_0 = -4J\cos\phi$, and hence as $\phi \to 0$, we recover the result found in Ref. [56]: $\mu_{\mathrm{SF}} = -4J + \nu(U + 2V_x + 2V_y)$. In order to determine where this superfluid phase is dynamically stable, we consider the excitation spectrum given by Eq. (5.9). The matrix elements of $M_{\mathbf{k}}^{\mathrm{SF}}$ are

$$\begin{aligned}
\omega_{\mathbf{k}} &= 2\nu(U + V_x + V_y) - \mu_{\mathrm{SF}} \\
\lambda_{\mathbf{k}} &= \nu U \\
\gamma_{\mathbf{k}} &= \epsilon_{\mathbf{k}} + \zeta_{\mathbf{k}} \\
\zeta_{\mathbf{k}} &= 2\nu V(\mathbf{k}).
\end{aligned} \tag{5.25}$$

As $\phi \to 0$, the excitation spectrum should reduce to

$$\Omega_{\mathbf{k}}^{\mathrm{SF}} = \sqrt{\tilde{\epsilon}_{\mathbf{k}}[\tilde{\epsilon}_{\mathbf{k}} + 2\nu(U + 2V(\mathbf{k}))]}, \tag{5.26}$$

with $\tilde{\epsilon}_{\mathbf{k}} = 2J[2 + \cos(k_x a) + \cos(k_y a)]$, as found in Ref. [56]. However, in order to make this comparison properly, we have to map the two-band excitation spectrum in the Brillouin zone defined by $k_x \pm k_y \in [-\pi/a, \pi/a]$ derived above, to the single-band spectrum in the Brillouin zone $k_{x/y} \in [-\pi/a, \pi/a]$ given in Ref. [56]. This mapping is described in e. g. Ref. [98]: it is the mapping from the extended to the reduced zone scheme. After applying this mapping, the two spectra are seen to be identical. In addition, as $V_x \to 0$ and $V_y \to 0$, the spectrum reduces to the one found in Ref. [30].

Checkerboard supersolid

To describe a phase with a checkerboard-modulated density (checkerboard supersolid, CSS), we follow the scheme used in Ref. [56]. We assume that the population density of sublattice $\mathcal{A}$ is different from that of sublattice

$\mathcal{B}$; hence, $\langle a \rangle \neq \langle b \rangle$. Instead of working with $\langle a \rangle$ and $\langle b \rangle$ directly, we go to a center-of-mass and relative representation, and write

$$
\begin{aligned}
\langle a \rangle &= \sqrt{N_{\mathrm{p}}/2}\left(\sqrt{\alpha} + \sqrt{\beta}\right) \\
\langle b \rangle &= \sqrt{N_{\mathrm{p}}/2}\left(\sqrt{\alpha} - \sqrt{\beta}\right).
\end{aligned}
\tag{5.27}
$$

Clearly, if we send β to zero, the density modulation vanishes. Replacing $a_{\mathbf{k}} \to \delta_{\mathbf{k},0}\langle a \rangle + \tilde{a}_{\mathbf{k}}$ and $b_{\mathbf{k}} \to \delta_{\mathbf{k},0}\langle b \rangle + \tilde{b}_{\mathbf{k}}$ in Eq. (5.5) and requiring the terms of first order in the fluctuations to vanish yields

$$
\begin{aligned}
\frac{\mu_{\mathcal{A}}}{\nu} &= \frac{\epsilon_{\mathbf{0}}}{\nu}\frac{\sqrt{\alpha} - \sqrt{\beta}}{\sqrt{\alpha} + \sqrt{\beta}} + U + 2V(0) + 2\sqrt{\alpha\beta}[U - 2V(0)], \\
\frac{\mu_{\mathcal{B}}}{\nu} &= \frac{\epsilon_{\mathbf{0}}}{\nu}\frac{\sqrt{\alpha} + \sqrt{\beta}}{\sqrt{\alpha} - \sqrt{\beta}} + U + 2V(0) - 2\sqrt{\alpha\beta}[U - 2V(0)],
\end{aligned}
\tag{5.28}
$$

where $\nu = N_{\mathrm{p}}/N_{\mathrm{s}}$ is the average number of atoms per site (filling factor) and we have used the fact that that $|\langle a \rangle|^2 + |\langle b \rangle|^2 = N_{\mathrm{p}}$ and hence $\alpha + \beta = 1$. Setting $\mu_{\mathcal{A}} = \mu_{\mathcal{B}}$ yields a condition on α and β, which can be solved for the difference $\alpha - \beta$; the result is

$$
\alpha - \beta = \frac{4J\cos\phi}{\nu(2V_x + 2V_y - U)}.
\tag{5.29}
$$

Now, we can now write α and β in terms of the parameters J, ϕ, U, V_x and V_y:

$$
\begin{aligned}
\alpha &= \frac{1}{2} + \frac{2J\cos\phi}{\nu(2V_x + 2V_y - U)}, \\
\beta &= \frac{1}{2} - \frac{2J\cos\phi}{\nu(2V_x + 2V_y - U)}.
\end{aligned}
\tag{5.30}
$$

With this result, we can calculate the chemical potential, and find $\mu_{\mathrm{CSS}} = 2\nu U$. For the checkerboard-modulated case, the matrix elements of $M_{\mathbf{k}}^{\mathrm{CSS}}$

in Eq. (5.9) are given by

$$
\begin{aligned}
\omega_{\mathbf{k}}^{a/b} &= 2U\nu\big(1 \pm 2\sqrt{\alpha\beta}\big) + 2V(0)\nu\big(1 \mp 2\sqrt{\alpha\beta}\big) - \mu_{\mathrm{CSS}}, \\
\lambda_{\mathbf{k}}^{a/b} &= U\nu\big(1 + 2\sqrt{\alpha\beta}\big), \\
\gamma_{\mathbf{k}} &= \epsilon_{\mathbf{k}} + \zeta_{\mathbf{k}}, \\
\zeta_{\mathbf{k}} &= 2\nu V(\mathbf{k}).
\end{aligned}
\tag{5.31}
$$

As in the homogeneous case, if we take the limit $\phi \to 0$, we recover the results from Ref. [56]: density modulation, chemical potential, and excitation spectrum. Note that for $0 < |\phi| < \pi/4$, the density modulation is affected by the flux, even though no vortices appear (see Eq. (5.29)).

5.4.2 Strong flux: staggered-vortex phase

As was found in Ref. [30], under the influence of a strong flux, $\pi/4 < |\phi| < 3\pi/4$, the system goes to a staggered-vortex superfluid (SVSF) phase. This corresponds to condensation in the single-particle state with momentum $(\pm\pi/a, 0)$ or $(0, \pm\pi/a)$, *i.e.* in the corners of the first Brillouin zone [2]. To describe this region of parameter space, we need the four-sublattice formalism presented in section 5.3.2. Although the description is different, the *ansatz* is still informed by earlier findings: we expect a combination of the staggered-vortex pattern from Ref. [30] and, for appropriately strong NN interactions, the checkerboard-modulated density from Ref. [56]. For a homogeneous density distribution, the *ansatz* is quite simple:

$$
\langle a_j \rangle = \nu e^{i(j-1)\pi/2},
\tag{5.32}
$$

where we have defined the phase of the mean-field wavefunction at sublattice SL_1 to be zero. For the discussion of the staggered-vortex checkerboard supersolid (SVCSS), there is a general point that is worth noting: in cases where the density modulation is invariant under exchange of the two lattice vectors, the vortices do not interfere with the density modulation. This

---

[2]Note that although the condensation momenta do not look identical, they actually are, since the relevant reciprocal lattice vectors are those of the $\mathcal{A}$ and $\mathcal{B}$ sublattices, which do translate these condensation points into each other.

can be seen from Eq. (5.15): as long as $r_1 = r_3$ and $r_2 = r_4$, the conditions on the phase drops do not depend on the wavefunction amplitudes. Since the checkerboard pattern has this symmetry, we can try to guess the modulation strength from the two-sublattice formalism. The *ansatz* would be:

$$
\begin{aligned}
a_{\mathbf{k}} &\to \sqrt{N_{\mathrm{p}}/2}\,\delta_{\mathbf{k},\pi}\left(\sqrt{\alpha} + \sqrt{\beta}\right) + \tilde{a}_{\mathbf{k}} \\
b_{\mathbf{k}} &\to i\sqrt{N_{\mathrm{p}}/2}\,\delta_{\mathbf{k},\pi}\left(\sqrt{\alpha} - \sqrt{\beta}\right) + \tilde{b}_{\mathbf{k}}.
\end{aligned}
\tag{5.33}
$$

Performing the same analysis as for the weak-flux case, we find that the density modulation strength is given by

$$
\alpha - \beta = \frac{4J\sin\phi}{\nu(2V_x + 2V_y - U)}
\tag{5.34}
$$

Hitherto, the two formalisms work equally well. However, the excitation spectrum can only be calculated in the four-sublattice formalism; the mean-field values for the four sublattices are

$$
\begin{aligned}
\langle a_1 \rangle &= \sqrt{N_{\mathrm{p}}/2}(\sqrt{\alpha} + \sqrt{\beta}) \\
\langle a_2 \rangle &= -i\sqrt{N_{\mathrm{p}}/2}(\sqrt{\alpha} - \sqrt{\beta}) \\
\langle a_3 \rangle &= -\sqrt{N_{\mathrm{p}}/2}(\sqrt{\alpha} + \sqrt{\beta}) \\
\langle a_4 \rangle &= i\sqrt{N_{\mathrm{p}}/2}(\sqrt{\alpha} - \sqrt{\beta}).
\end{aligned}
\tag{5.35}
$$

By inserting these values for $\langle a_j \rangle$ into Eqs. (5.19) and (5.22), we find the corresponding ground state energy and excitation spectrum.

5.4.3   Phase diagram

Now we have all the information required to determine the cross section of the phase diagram along the line $V_x = V_y$. In order to obtain the phase boundaries, we calculate the parameter values where the density modulation vanishes, where the excitation spectra become unstable, and where

the ground state energies of two phases are equal. These three phenomena happen simultaneously at the SF-CSS and SVSF-SVCSS phase boundaries (see Fig. 5.4). Since the relevant order parameter for this phase transition is the density modulation, which vanishes continously at the border, this is a second-order phase transition. At the SF-SVSF and CSS-SVCSS boundaries, the ground state energies of the uniform and staggered-vortex phases become equal. The relevant order parameter for these transitions is the (staggered) number of vortices per plaquette, which jumps from zero to unity; hence, these are first-order phase transitions.

Fig. 5.4 shows the $V_x = V_y$ cross section of the phase diagram. The combination of flux and NN interactions leads to a phase boundary with the same shape as observed in Ref. [30] in the MI-SF phase diagram. The phase transition from the homogeneous-density phase to the checkerboard phase is continuous, independently of the flux; the phase transition from the uniform to the staggered-vortex phase is discontinuous, independently of the density modulation.

In conclusion, this cross-section of the phase diagram shows a relatively straightforward superposition of the phases found in Refs. [56] and [30]. Beyond the results found in those references, we note a few aspects: The symmetry in the line $\phi = \pi/4$ goes further than the shape of the phase boundary, since the strength of the density modulation is also symmetric. The origin of this symmetry can be found in Eqs. (5.29) and (5.34): the cosine from the uniform SF and CSS phases is replaced by a sine in the staggered-vortex phases. The SF-CSS transition can also be induced by changing ϕ, provided V_x and V_y are in the right range. The critical value of V_x/U shifts with $J/\nu U$, but the phase boundaries retain their periodicity in ϕ, within the approximation used here.

5.5 Quantum phases: asymmetric case

In Eqs. (5.15) and (5.17), we see the interplay between the phase and density distributions. As noted in section 5.4.2, both a homogeneous density and a checkerboard pattern are possible within the *ansatz* employed in Ref. [30], in
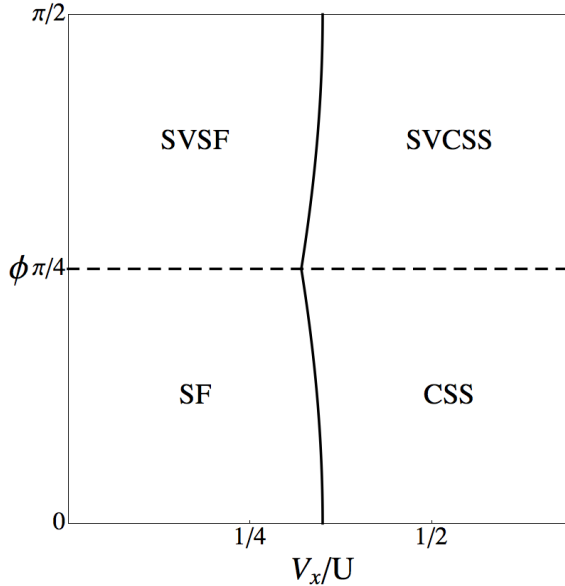
Figure 5.4: Cross section of the phase diagram for $V_x = V_y$ and $J/(\nu U) = 0.1$. Dashed (solid) lines are first (second) order phase transitions. Legend: SVSF = homogeneous staggered-vortex superfluid; SVCSS = staggered-vortex checkerboard supersolid.

which all phase drops are assumed to be equal. If, however, $r_1 \neq r_3$ and/or $r_2 \neq r_4$, as in the case of stripes or four different densities on the four sites of one plaquette, the phase distribution is influenced by the density modulation, and we have to allow for phase drops taking other values than integer multiples of $\pi/2$. We indeed find such solutions, in the striped phase for $0 < \phi < \pi/2$. The mean-field wavefunction values $\langle a_j \rangle$ are determined by numerically solving Eqs. (5.15)-(5.18).

5.5.1 Phase diagram cross section I: $V_y = 0$

We obtain the phase diagram in the same manner as in section 5.4: by calculating where the density modulations vanish, where the excitation spectra develop instabilities, and by comparing ground state energies. Along the
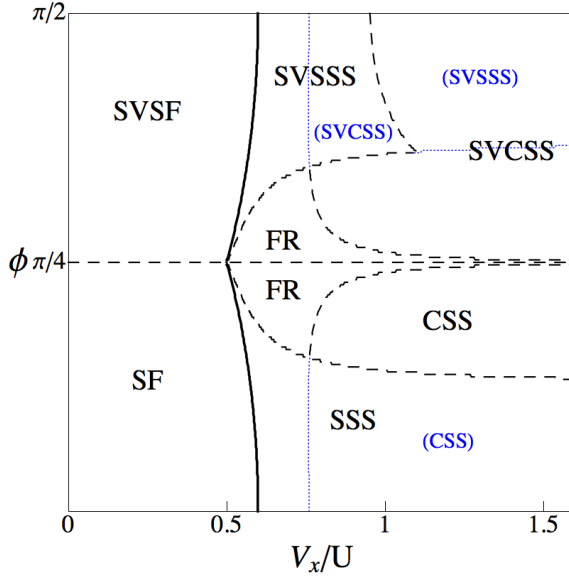
Figure 5.5: Cross section of the phase diagram for $V_y = 0$ and $J/(\nu U) = 0.1$. Legend: SSS = striped supersolid; SVSSS = staggered-vortex striped supersolid; FR = forbidden region, phase separation. Dotted blue (grey) lines represent the existence of metastable states, which are labelled in blue (grey) and between brackets.

line $V_y = 0$, we find a variety of phases (see Fig. 5.5.1). The superposition of the CSS phase from Ref. [56] with the staggered-vortex phase from Ref. [30] is there, as well as the uniform and staggered-vortex superfluids without density modulation. The striped supersolid (SSS) and staggered-vortex striped supersolid (SVSSS) phases are not simple combinations of earlier

found phases, however: they break the symmetry within the sublattices $\mathcal{A}$ and $\mathcal{B}$, *i.e.* between sublattices SL_1 and SL_3, and SL_2 and SL_4, respectively. The density modulates in a striped pattern, but the phase drops are different on all four edges of the elementary plaquette. Note again the high degree of symmetry in the line $\phi = \pi/4$: the dynamical stability diagram is completely symmetric, as well as the density modulation strength, also for the striped phase. Apart from the phase distribution, which cannot be symmetric, it is only the ground state energy difference between the checkerboard and striped phases that is different between the two regions $|\phi| < \pi/4$ and $|\phi| > \pi/4$. In the staggered-vortex region, the checkerboard phase has a lower ground state energy than the striped phase, which can be understood as a consequence of the matching between the sublattice divisions associated with the flux and the density modulation. The flux breaks the symmetry between sublattices $\mathcal{A}$ and $\mathcal{B}$ (for details see Ref. [30]), thus introducing a checkerboard pattern, which competes with the striped pattern introduced by the NN interactions.

Also note the shape of the second-order phase boundary, in this case between the homogeneous and striped phases. It shows the same pattern as the boundary between the homogeneous and checkerboard phases (see Fig. 5.4), and the SF-MI boundary in the absence of NN interactions (see Fig. 5.1). This shape can be understood from the effect of the flux on the hopping energy in the ground state: it is modified by $\cos\phi$ in the uniform superfluid, and $\sin\phi$ in the staggered-vortex superfluid, resulting in a minimum at $\phi = \pi/4$. Since it is the hopping term in the Hamiltonian that favors the superfluidity in the SF-MI phase transition, and the homogeneity in the SF-CSS and SF-SSS transitions, the reduction in hopping energy makes phases which break the phase coherence or homogeneous density distribution more favorable.

There is one region, close to $\phi = \pi/4$, where we do not find any dynamically stable phases (FR - forbidden region). This result is a consequence of our approach, which assumes the existence of a well-defined chemical potential for the whole system, and hence a uniform macroscopic density distribution, since we are not working in a trap. If we drop the assumption of a well-defined chemical potential, we effectively allow the system to

separate into parts with different densities. Shifting the density changes the parameter $J/\nu U$, which changes the critical values of V_x/U in such a way that any point in the forbidden region can be made to lie within the two closest neighboring stable regions. Hence, if the parameters are tuned to lie in the forbidden region, our calculations predict that the system will phase separate. Note that there are actually two different forbidden regions, since the phases the system will separate into are different for $|\phi| < \pi/4$ and $|\phi| > \pi/4$.

5.5.2 Phase diagram cross section II: $\phi = \pi/2$

Finally, a comment on the two cross sections of constant ϕ (see Fig. 5.2). We show the cases where $\phi = 0$ and $\phi = \pi/2$, *i.e.* the centers of the uniform and the staggered-vortex phases. As mentioned above, the phase diagram has a high degree of symmetry in the line $\phi = \pi/4$, the only differences being the phase distribution and the ground state energies of the striped and checkerboard phases. In Fig. 5.2, we see that the CSS-SSS phase boundary shifts, but nothing else. Intermediate cross sections would also reveal the forbidden region discussed above, and the disappearance of the striped phase near $\phi = \pi/4$.

5.6 Experimental signatures

A good starting point for experimental detection of the various phases discussed in this chapter is the momentum distribution $n(\mathbf{k})$, since most of the phases have a unique momentum distribution, as will be discussed below. Experimentally, the momentum distribution is accessible through the technique of time-of-flight measurement [1], which converts the momentum distribution into a spatial one by suddenly turning off the lattice and allowing the cloud to expand ballistically. $n(\mathbf{k})$ is given by [30]

$$n(\mathbf{k}) = |w(\mathbf{k})|^2 \left| \sum_{\mathbf{P}} e^{i\mathbf{k}\cdot\mathbf{P}} \right|^2 \sum_{\mu,\nu=1}^{4} e^{i\mathbf{k}\cdot(\mathbf{r}_\nu - \mathbf{r}_\mu)} \left\langle a^\dagger_{\mathbf{r}_\mu} a_{\mathbf{r}_\nu} \right\rangle. \qquad (5.36)$$
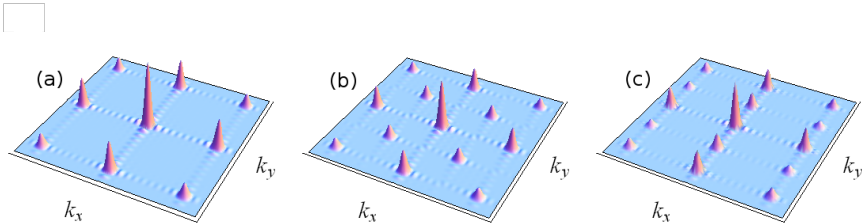
Figure 5.6: The momentum distributions for the (a) SF, (b) CSS, and (c) SSS phases.

Here, $\mathbf{P}$ runs over all plaquettes, i.e. $\mathbf{P} = 2a(n_x, n_y)$, with integer $n_{x/y}$, and $\mathbf{r}_\mu$ and $\mathbf{r}_\nu$ run over the four sites of the plaquette. The last factor is the one that distinguishes between the phases, since all configurations are invariant under translation by $\mathbf{P}$. To calculate it, we follow Ref. [30] and approximate the N-particle state on the lattice by a coherent state with on average N particles. Now the calculation becomes very simple, since in this approximation,

$$\left\langle a^\dagger_{\mathbf{r}_\mu} a_{\mathbf{r}_\nu} \right\rangle \approx \langle a_\mu \rangle \langle a_\nu \rangle, \tag{5.37}$$

for which we have explicit results (see sections 5.3-5.5). Using the same parameters as in Ref. [30], we obtain the signatures shown in Figs. 5.6 and 5.7. In Fig. 5.6, we see that supersolidity manifests itself in the momentum distribution by replacing the peaks from the homogeneous SF by a smaller peak and 'satellite peaks' displaced by the characteristic vectors of the density modulation. Fig. 5.7 shows that the same replacement takes place in the staggered-vortex phases. Unfortunately, this implies that the SVSF and SVCSS phases look exactly the same, since the peaks of the SVSF momentum distribution are displaced from each other by exactly the characteristic vectors of the CSS density modulation. In Fig. 6, we see another curiosity: the two striped phases, with stripes in the x- and y-directions, are indistinguishable for $\phi = \pi/2$, where the phase drops along the plaquette are equal. For different values of ϕ, the two striped phases are distinguishable. Also,
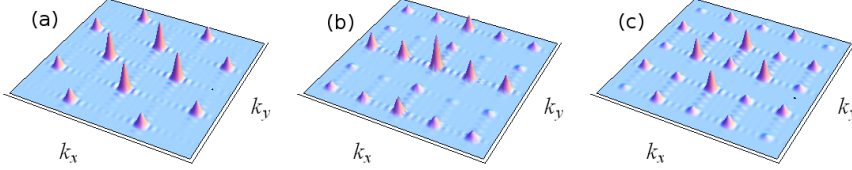
Figure 5.7: The momentum distributions for the (a) SVSF, (b) SVSSS at $\phi = 7\pi/20$, and (c) SVSSS at $\phi = \pi/2$ phases. The SVCSS phase has exactly the same signature as the SVSF phase.

as discussed in sections 5.3 and 5.5, the phase distribution is asymmetric for $\phi \notin \{0, \pi/2\}$ in the striped phase. This asymmetry reflects the interplay between NN interactions and applied flux, and is a continuous function of ϕ.

5.7 Discussion & conclusions

In this chapter, we have analysed the interplay between NN interactions and a synthetic staggered magnetic field in a system of bosons in a two-dimensional square optical lattice. We have used the Bogolyubov approximation to obtain the theoretical mean-field phase diagram of the system. The equilibrium condition that traditionally gives the value of the chemical potential was replaced by a set of conditions that give the density and phase modulations between the lattice sites, as well as the chemical potential. The excitation spectrum allowed us to determine the dynamical stability of the phases encountered in the system.

Our analysis resulted in a rich phase diagram featuring various superfluid and supersolid phases. Apart from the conventional and staggered-vortex superfluids and the checkerboard and striped supersolids found before, the system turns out to feature phases which combine a staggered-vortex phase configuration and supersolidity. Where the density modula-

tion is invariant under exchange of the lattice vectors, it does not influence the phase configuration; in case of an asymmetric density modulation, the phase drops around the plaquette are also distributed asymmetrically. Lastly, we have identified a forbidden region, where the system cannot form a stable state with the same average density in all areas. In this region of parameter space, our calculations predict that the system will phase separate.

We observe that even a rather crude approximation to the dipolar interaction, where the long tail is cut off beyond the NN range, combined with the staggered flux, leads to a very rich phase diagram. Apart from the expected 'superposition' of density modulations and a staggered-vortex pattern, another layer of structure emerges: the phase drops do not have to be distributed homogeneously along the elementary plaquette.

We also see that many of the phase transitions can be driven by tuning either the NN interaction strengths or the flux, which is a consequence of the fact that the flux modifies the hopping energy. Thus, it affects both the vorticity, which is a discrete variable, and the density modulation, which is a continuous variable. This is yet another example of the interesting physics that comes with the possibility of generating an artificial staggered magnetic field in an optical lattice.

Potentially interesting questions that were beyond the scope of this project include taking into account the effects of the long tail of the dipolar interaction and the effects of finite temperatures on the supersolid phases. Since our work was exploratory in nature, we have not been able to address these problems, but they would certainly be relevant for experimental tests of the predicted phases. Another point left unaddressed here is the full periodicity in ϕ of the phase diagram. Fig. 5.1 shows the 2π-periodic nature of the system, while we have only considered values of ϕ between 0 and $\pi/2$ in this chapter. Note that since the two staggered-vortex phases are identical, the system is symmetric under $\phi \to -\phi$. Thus, we have studied half of the phase diagram's entire period. The other half is expected to feature phases and phenomena similar to those already discussed here, as can be deduced from the nature of the density and phase distributions found.

Chapter 6

Incommensurability effects for strongly interacting bosons in a 1D optical lattice

Abstract

In this chapter[1], we investigate quantum phase transitions occurring in a system of strongly interacting ultracold bosons in a 1D optical lattice. After discussing the commensurate-incommensurate transition, we focus on the phases appearing at incommensurate filling. We find a rich phase diagram, with superfluid, supersolid and Mott insulator (kink-lattice) phases. Supersolids generally appear in theoretical studies of systems with long-range interactions; our results break this paradigm and show that they may also emerge in models including only short-range (contact) interactions, provided that quantum fluctuations are properly taken into account.

---

[1]This chapter is based on the publication *Strongly interacting bosons in a one-dimensional optical lattice at incommensurate densities*, Phys. Rev. A **84**, 023620 (2011) by A. Lazarides, O. Tieleman, and C. Morais Smith.

6.1   Introduction

In the previous chapters, we have dealt with 2D systems. Here, we go one dimension lower, and study a gas of bosonic atoms trapped in a one-dimensional lattice. In one dimension, a number of interesting effects occur, related to the fact that the particle statistics (bosonic or fermionic) do not play as large a role as they do in higher dimensions. One such example is the Tonks-Girardeau gas, where bosons avoid spatial overlap and acquire fermionic properties due to strong repulsive interactions. This peculiar state of matter has been experimentally realized in 1D [99]. On the other hand, the low-energy behaviour of many fermionic systems is accurately described by bosonic models, obtained from a procedure called *bosonisation* [100].

Recently, a new type of quantum phase transition was observed in 1D in the very strongly interacting regime: for an arbitrarily weak optical lattice potential *commensurate* with the atomic density of the Bose gas, a quantum phase transition into an insulating, gapped state, was observed, with the atoms pinned at the lattice minima [62]. Theoretical studies of 1D systems based on the sine-Gordon model indeed predict that above a critical interaction strength, the superfluid should become a Mott insulator even for a *vanishingly weak* optical lattice [64].

The quantum sine-Gordon model has been intensively studied in condensed matter and high-energy physics because it is an exactly solvable quantum field theory, which is able to capture non-linear effects due to the presence of the cosine term [101]. The experiment in Ref. [62] has then extended the phase diagram for bosons in one dimension from the Hubbard regime, which occurs for weakly interacting atoms, into the strongly interacting regime of the sine-Gordon model, thus revealing a new class of quantum phase transitions.

In this chapter, we show that another interesting regime can be reached if the density is *incommensurate* with the optical lattice. The system is then described by the Pokrovsky-Talapov model, which is a *driven* sine-Gordon model. In this model, the SF-MI transition may be approached in two different ways, either by tuning the interaction strength at constant lattice

depth and commensurate period, as already realized experimentally [62], or by tuning the density or lattice parameter away from commensurability. We study the excitations of the system in the incommensurate phase and show that a supersolid phase may arise. In addition, for sufficiently large lattice strengths, a MI phase is stabilized even at non-unit filling.

6.1.1 Approach

Our approach to studying this system is as follows: First, following previous works [63, 64, 62], we formulate the underlying 1D interacting boson problem in terms of a quantum sine-Gordon field theory, with the deviation of the number density from commensurate values driving the appearance of kinks in the field. We then show that a previous result [64], in which a finite threshold for the commensurate-incommensurate MI-SF transition was found, is incorrect, and obtain the correct result, $Q_c = 0$. We next study the incommensurate regime, in which the excess particles appear as kinks of the sine-Gordon field, having an effective mass and effective interactions different from the bare particles. We extract these two parameters exactly from the underlying field theory and finally apply a functional renormalization group (RG) approach to the path integral formulation of the many-body statistical density matrix to obtain the ground state properties of the system. The RG transformation shows that quantum fluctuations renormalize the interactions between the kinks to a power law form, which corresponds to the Calogero-Sutherland model [102]. This finally allows us to propose a phase diagram for the incommensurate regime (see Fig. 6.3). When the lattice potential is strong enough, the system is a MI. However, the MI phase here is actually a lattice of kinks, and the number of particles per site is not fixed. At intermediate values of the lattice potential, we predict the emergence of a supersolid phase. As discussed in chapter 5, supersolid phases usually occur in model Hamiltonians which include long-range interactions, and have a characteristic wavelength which is an integer multiple of the lattice spacing [32, 103, 56, 57, 104]. The most striking feature of the system studied in this chapter is that while the original Hamiltonian contains only *local* interactions, the supersolid phase appears due to the

finite-range nature of the interaction between the excitations. In addition, the periodicity of the supersolid phase found here is *unrelated* to that of the lattice. This makes the appearance of this supersolid phase qualitatively different from the situations usually found in the literature, where the characteristic wavelength of the supersolid is an integer multiple of the lattice spacing.

6.2   Model

The microscopic description of a trapped gas of cold bosons in 1D with contact interactions and in the presence of a single-particle potential $V(x)$ is

$$
\begin{aligned}
H = \int_{-\infty}^{\infty} dx \left[\psi^\dagger(x) \left(-\frac{\hbar^2}{2m} \nabla^2 + V(x) \right) \psi(x) \right. \\
\left. + \frac{g}{2} \int_{-\infty}^{\infty} dx\, \psi^\dagger(x) \psi^\dagger(x) \psi(x) \psi(x) \right],
\end{aligned}
\tag{6.1}
$$

where g is the strength of the δ-function interaction, ψ ($\psi^\dagger$) are bosonic annihilation (creation) operators, and m is the atomic mass. The parameter characterizing the strength of the interactions is the Lieb-Liniger parameter $\gamma = mg/\hbar^2 n_0$, where n_0 is the average density.

Density operator

Below, we will write $\psi(x) = \sqrt{n(x)} \exp(-i\theta(x))$, with $n(x)$ the density and $\theta(x)$ the (real) phase. Before continuing, let us cast the density operator in a more pratical form:

$$
\rho(x) = \sum_j \delta(x - x_j) = \sum_n \partial_x \chi(x) \delta[\chi(x) - 2\pi n],
\tag{6.2}
$$

where the field $\chi(x)$ takes the value $2\pi n$ at the position of the nth particle (see Ref. [100] for some details on how to obtain this form). Using the

Poisson summation formula to express the delta functions yields

$$\rho(x) = \frac{\partial_x \chi(x)}{2\pi} \sum_p e^{ip\chi(x)}. \tag{6.3}$$

Now we divide χ by 2 and subtract out its increase due to the average density:

$$\phi(x) = \chi(x)/2 - \pi\rho_0 x. \tag{6.4}$$

This last step allow us, after only a few more steps of symbol manipulation, to obtain the following, final form for the density operator [63, 64]:

$$n(x) = \left(n_0 - \frac{1}{\pi}\partial_x\phi(x)\right) \sum_{p=-\infty}^{\infty} e^{2ip[\pi n_0 x - \phi(x)]}. \tag{6.5}$$

The field χ obeys the boundary condition $\int dx \partial_x \chi(x) = 2\pi N$, and consequently, ϕ must obey $\int dx \partial_x \phi(x) = 0$. Eq. (6.5) yields an expression for the bosonic operators in Eq. (6.1) in terms of the new field ϕ. The appropriate bosonic commutation relations are satisfied if $[\partial_x\phi(x), \theta(x')] = -i\pi\hbar\delta(x - x')$; that is, θ and $\partial_x\phi/\pi$ are canonically conjugate variables. From Eq. (6.5), it follows that *kinks in the ϕ field correspond to particle-like excitations*: the kinks are where $\partial_x\phi(x)$ deviates from its average value of zero. This fact will be of great importance to us later on. In order to make proper comparisons to earlier work, it is also important to note that the field ϕ of Eq. (6.5) is *non*-compact; that is, it is not a periodic field; $\phi + 2\pi \neq \phi$.

Action

In the long-wavelength limit, and in the presence of an optical lattice creating a single-particle potential $V(x) = (V/2)\cos(4\pi x/\lambda)$, the system of

Eq. (6.1) may be described by an action of the form

$$
\begin{aligned}
\mathcal{S}[\phi] = &\int_0^\beta d\tau \int_{-\infty}^\infty dx \, \frac{1}{8\pi K} \left[(\partial_x \phi)^2 + (\partial_\tau \phi)^2 \right] \\
&+ \frac{u}{2} \int_0^\beta d\tau \int_{-\infty}^\infty dx \, \cos[\phi(x) - Qx],
\end{aligned}
\tag{6.6}
$$

where we have now set $\hbar = 1$, scaled lengths such that the speed of sound is unity, and finally scaled $\phi \to \phi/2$. Here, $\beta = 1/k_B T$, $u = n_0 V$, while K is the usual Luttinger liquid parameter. For bosons interacting via contact potentials, K may be expressed in terms of γ; for large γ, $K \approx (1 + 2/\gamma)^2$, while for smaller interaction strengths γ it is given by $K \approx \sqrt{\gamma - \gamma^{3/2}/(2\pi)}$. We have also only kept the most relevant (least quickly oscillating in space) terms and written $Q = 2\pi (n_0 - 2/\lambda)$ as the deviation of the average density from its commensurate value.

In the zero-temperature, $\beta \to \infty$ limit, Eq. (6.6) is formally equivalent to the classical Pokrovsky-Talapov model studied in Ref. [105]. It is also related to previous work on quantum Hall bilayer systems [106, 107, 108, 109, 110], with the important difference that the boundary conditions in the present case are $\int dx \, \partial_x \phi = 0$, while in Refs. [107, 65, 105] (amongst numerous others), there is no such restriction on ϕ. This is crucial to the position of the commensurate-incommensurate transition, and is due to the fact that we are working at fixed particle number.

Since kinks correspond to excess particles above the commensurate density (see Fig. 6.1), fixing the particle density *must* fix the number density of kinks uniquely. But from its definition, Q is directly proportional to this excess particle density, so that *the kink density must be proportional to Q itself.* This immediately implies that $Q_c = 0$, at least at zero temperature. Mathematically, this is a consequence of the boundary condition at the edges of the system, which implies that the commensurate phase cannot exist unless $Q = 0$. For any $Q > 0$, a finite kink density appears, representing the excess particles, which are bosons. Note that, as far as the effective description of these kinks as particles is concerned, there is no lattice; the lattice only comes in in the derivation of the effective mass and
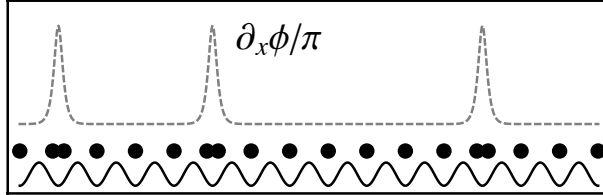
interactions between the kinks.

Figure 6.1: $Q > 0$; the dashed line is $\partial_x \phi$, the solid line is the periodic potential, and the corresponding particle positions are indicated. Notice how kinks (indicated by localized deviations from a straight line for $\partial_x \phi$) correspond to particles in excess of the commensurate particle density.

6.3 Kink-kink interactions

By taking into account the effects of quantum fluctuations, we shall now show that the bosonic particles represented by the kinks in the ϕ field may be mapped to a Calogero-Sutherland model (CSM), the various phases of which have been studied thoroughly. This will allow us to predict the behaviour of the system for finite Q.

The full analytical expression for the bare interaction between two kinks in a sine-Gordon model is given in Ref. [66]; its limiting forms are

$$V_{\text{bare}}(r) \rightarrow \begin{cases} \frac{8}{\pi\xi}\exp(-x/\xi), & r \gg \xi \\ \pi/(2r), & r \ll \xi. \end{cases} \tag{6.7}$$

The effective width of the kinks is $\xi = 1/\sqrt{2\pi K n_0 V}$, so that this potential amounts to an impenetrable core plus a finite-range repulsion. Their effective mass is [111, 107]

$$\sigma = \frac{2\Gamma(\eta/2)}{\sqrt{\pi}\Gamma((\eta+1)/2)} \left(\pi u \frac{\Gamma\left(\frac{1}{\eta+1}\right)}{\Gamma\left(\frac{\eta}{\eta+1}\right)}\right)^{1/2(\eta+1)} \tag{6.8}$$

with $\eta = 1/(2K^{-1}-1)$ and Γ is the Γ function. The mass vanishes whenever either $V \to 0$ or $K \to 2$, corresponding to a critical $\gamma_c \approx 3.5$, as observed experimentally in Ref. [62].

To study the system of interacting kinks, we employ the statistical density matrix in imaginary time and position representation [112, 113]. This is given by

$$\rho(R, R; \beta) = \int \prod_j \mathbb{D}x_j \exp(-S[\{x_n\}]/\hbar) \qquad (6.9)$$

where $\{x_n(\tau)\}$ denotes the set of positions of the particles at time τ, $R = \{r_1, r_2, \ldots, r_N\}$ denotes the set of positions of the particles at $\tau = 0$ and $\tau = \beta$ (see below) while $\mathbb{D}x_j$ denotes functional integration over x_j; finally,

$$S[\{x_n\}] = \frac{1}{2} \int d\tau \left[-\sigma \sum_n (\partial_\tau x_n)^2 + \sum_{n,m} V(x_n - x_m) \right]. \qquad (6.10)$$

In Eq. (6.10), the integral runs from zero to β and there is an ultraviolet cutoff $\Lambda_\tau = 2\pi/\Delta\tau$ with $\Delta\tau$ a discretisation step size [112]. Note that Eq. (6.9) and Eq. (6.10) describe the ρ appropriate for distinguishable particles; for bosonic particles, one symmetrises in the end, so that $\rho_B(R, R'; \beta) = \sum_P \rho(R, PR'; \beta)$, with P labelling the permutation.

We begin by estimating the temperature dependence of the critical incommensurability Q_d above which exchange effects become important. The worldlines of the particles are of length β in the time-like direction, and the "width" of the path in the space-time direction will be $w \propto \sqrt{\hbar^2\beta/\sigma}$. If the average inter-kink distance, proportional to Q^{-1}, is larger than this, quantum effects are not important; the condition for the statistics to be important is therefore $Q\sqrt{\hbar^2\beta/\sigma} > 1$, up to a numerical factor. This defines a critical $Q_d \propto \sqrt{k_B T\sigma/\hbar^2}$. Below this Q_d, the kinks behave like free bosons; above it, the system is in a degenerate state, and we expect the effects described below to be evident. Furthermore, since σ vanishes on the lines $V = 0$ and $K = 2$, Q_d also vanishes there.
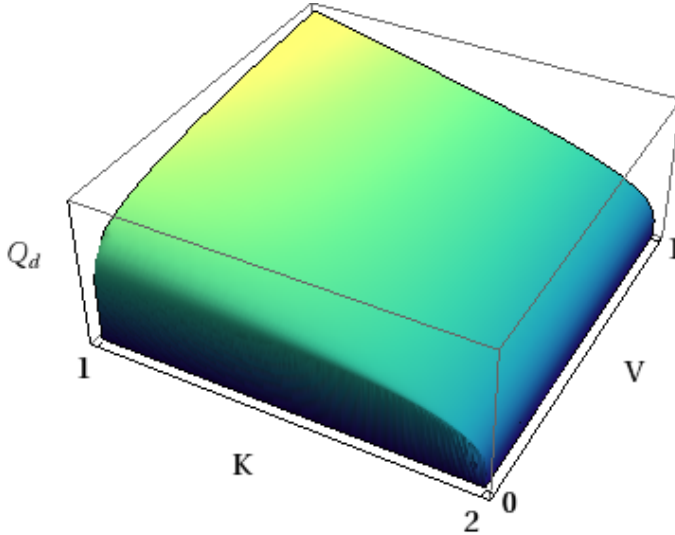
Figure 6.2: Finite T behaviour of Q_d, the deviation of the filling factor from unity at which the quasiparticles reach degeneracy; this is at an arbitrary but finite T.

6.3.1   Renormalisation group arguments

Next, we concentrate on the $T = 0$ or $\beta \to \infty$ limit, corresponding to infinitely long strings; in this limit, the degeneracy condition is always satisfied. We shall employ a renormalization group (RG) technique applied directly to the density matrix of Eq. (6.9). Details of this will be presented elsewhere [114]; here, we shall only outline the derivation and describe our conclusions.

As usual, we split the x_i into two parts, one composed of Fourier modes in a thin shell close to the cutoff, $\Lambda_\tau/b < q < \Lambda_\tau$ and the other with $q < \Lambda_\tau/b$, with $b = \exp(\epsilon)$ and ϵ small. It is then possible to extend the Wegner-Houghton approach [115, 116] to the many-body case, obtaining

the flow equation for the potential

$$\partial_\epsilon V = V + \frac{1}{2}x\partial_x V + \hbar\Lambda_\tau \log\left(\frac{1}{2}\sigma\Lambda_\tau^2 + \partial_{x,x}V\right). \tag{6.11}$$

The first two terms on the right hand side are obtained by rescaling both x_i and τ so as to restore the cutoff and keep the effective mass constant; they are therefore independent of the precise RG scheme employed and are responsible for the functional form of the fixed points. The last term is the fluctuation correction and fixes the proportionality constant for the fixed point potentials. Finally, notice that the coarse-graining is done in the τ direction; thus, information on lengthscales comparable to the kink density is still present in the fixed point potentials.

The physics of the system is determined by the fixed point potentials of Eq. (6.11). For bare (initial) potentials that diverge at the origin, these may be determined numerically; for $x \gg \hbar/\Lambda_\tau\sigma$, their behaviour is

$$V_{fp} = \frac{\hbar^2}{2\sigma}\frac{\lambda(\lambda-1)}{x^2}, \tag{6.12}$$

where we have written the coefficient of x^{-2} as $\hbar^2\lambda(\lambda-1)/2\sigma$ in order to make contact with the conventional notation in the literature (see below). We are thus dealing with a system of bosons interacting via an inverse square power law; this is the celebrated Calogero-Sutherland model [102], the ground-state wavefunction and low-energy spectrum of which are known. We concentrate here on its ground-state properties, which have been studied using numerical techniques [117]. The authors of Ref. [117] find (quasi-)long-range off-diagonal order for $0 < \lambda < 2$, while they find (quasi-)long-range diagonal order for $\lambda > 1$. The system is thus in a condensed, SF state for $0 < \lambda < 1$, in a SS state, characterised by the simultaneous presence of diagonal and off-diagonal long-range order for $1 < \lambda < 2$, and in a crystalline, MI state characterised by strong diagonal correlations for $2 < \lambda$. Therefore, the phase in which the system is for incommensurate densities ($Q \neq 0$) depends on the range in which the λ corresponding to the potential in Eq. (6.7) lies.

6.3.2 Phase diagram

To map out the phase diagram, we note that local analysis of the fixed point ordinary differential equation, Eq. (6.11) with the left hand side set to 0, indicates that the fixed point potentials, V_{fp}, have the property that $\partial V_{fp}/\partial \sigma > 0$ (for all x). An increase in σ therefore results in an increase in λ of Eq. (6.12). In addition, at $K = 1$ and $V = 0$ (hard-core free bosons), $\lambda = 1$ [118]. Based on these two pieces of information, and the expression for σ given in Eq. (6.8), we propose the phase diagram in Fig. 6.3 for $T = 0$. Starting from the point $K = 1$, $V = 0$, an increase of V causes a rapid increase of σ, which corresponds to an increase in λ so that $\lambda > 1$ which corresponds to SS. As V is further increased, λ reaches the value $\lambda = 2$ at $V = V_{c,m}$, at which point phase coherence is lost, the structure factor displays a sharp peak [117], and the system is in the MI state. This MI state is unusual in that the filling factor is not an integer; it corresponds to the kinks forming a lattice, and is not directly related to the underlying lattice. On the other hand, starting from any point on the $K = 1$ line and increasing K corresponds to decreasing σ, thus decreasing λ from its value at $K = 1$. As a result, the line $V_{c,m}$ curves upwards as K increases. Starting from $V_{c,0}(K = 1) = 0$ and increasing K, λ must decrease below 1 so that the diagonal order is suppressed; thus, the line $V_{c,0}$ separating the SF from the SS region also curves upwards. As $K \to 2$, or $\gamma \to 3.5$, the effective mass of Eq. (6.8) vanishes for any V; this results in a rapid decrease of λ, so that both lines curve upwards sharply.

It is important to note that the presence of the SS phase represents an order out of disorder effect: quantum fluctuations, which at first sight one would expect disorder the system, result in a strengthening of the repulsion which in turn causes the system to order.

Let us briefly discuss the differences between the phases just described in terms of experimentally accessible quantities. The main distinguishing features of these phases are the diagonal and off-diagonal correlations [117]. Off-diagonal long-range order may be observed using time-of-flight measurements, which therefore allow to distinguish the SF and SS phase-coherent phases from the MI phase; in the latter phase correlations drop quickly and
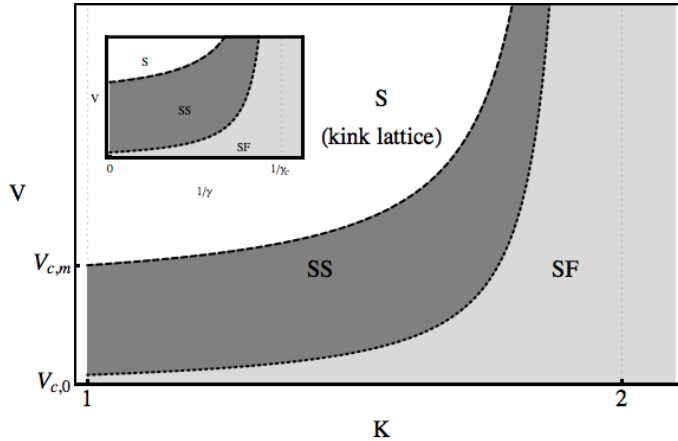
Figure 6.3: $T = 0$ phase diagram for a filling factor slightly above unit filling. SF, SS and S indicate superfluid, supersolid and solid (Mott insulating) phases, respectively.

the time-of-flight image is smeared. On the other hand, techniques for measuring density variations would distinguish between the SS and MI phases on one hand and the SF phase on the other; single-site addressability is possible [119, 120, 121], which may alllow to detect density modulations.

6.4   Conclusions

In summary, we have shown that the incommensurability-induced Mott insulator-superfluid transition occurs for arbitrarily small incommensurability, in contradiction to an earlier result in the literature [64]. We have also studied the system of bosonic quasiparticles which appears as soon as commensurability is lost; calculating the effective interactions between them, as well as their effective mass, and using an RG transformation, we have argued that quantum fluctuations drive the interactions to change to an inverse square form (a Calogero-Sutherland model). Based on known results for the Calogero-Sutherland model, we propose a phase diagram

for the current system of strongly interacting bosons in a weak optical lattice, featuring MI, SS, and SF phases. The SS phase is notable because it emerges from a model with local interactions only, and, like the MI, has a periodicity unrelated to that of the underlying lattice.

Although the experimental setup of Ref. [62] allows, in principle, to tune the density and to investigate also the commensurate-incommensurate quantum phase transition, up to now only the commensurate regime has been studied. We hope that our work will trigger further experiments into this fascinating and largely unexplored regime.

Chapter 7

Summary and outlook

This final chapter consists of a brief summary of the research presented above, and an outlook on future research that it will hopefully inspire.

7.1   Summary

The research described in this thesis concerns current and fascinating topics such as supersolids, spontaneous time-reversal symmetry breaking, and dynamical control of ultracold atoms in optical lattices.

In chapter 3, we have seen how periodically driving a non-separable square lattice potential along its diagonal leads to a modification of both the single-particle spectrum and the Mott insulator-superfluid phase boundary. The minimum of the single-particle spectrum, which determines the momentum state where the bosons condense, is split up into two inequivalent ones, which migrate from the center to the corner of the Brillouin zone as the driving parameter is ramped up. The critical interaction strength for the MI-SF phase transition drops to almost zero, and increases again as the BEC momentum reaches the corner of the Brillouin zone, following a trajectory that can be explained by considering how various hopping matrix elements are renormalised by Bessel functions (cf. [17, 19]).

In chapter 4, a kinetically frustrated single-species Fermi gas with long-

range interactions in a triangular lattice was shown to spontaneously break both time-reversal and translational symmetry, under suitable conditions specified by filling factor, temperature, and nearest-neighbour interaction strength. An extensive study of the mean-field free energy revealed the physical mechanisms responsible for breaking the various symmetries, as well as the interactions between these mechanisms. For low densities, a phase was discovered where the system features staggered currents running around the elementary plaquettes of the lattice, analogous to a recent bosonic result [14, 10]. At filling factors around 1/4, the system develops a density wave. For sufficiently strong interactions, the density wave is complemented by a pattern of currents that is confined to the low-density sites (different from the staggered currents at low densities), thus leading to a combined time-reversal and translational symmetry-broken phase. Exact diagonalisation studies were found to corroborate the mean-field results.

In chapter 5, a mean-field study of a bosonic lattice model with nearest-neighbour interactions and a staggered gauge field revealed a variety of phases, including a supersolid, a staggered-vortex superfluid, and a staggered-vortex supersolid. By adjusting the Bogolyubov approximation to a translational-symmetry-broken state with a four-site unit cell, we found that the phase distribution around the elementary plaquette was influenced by the density modulation; in other words, the currents induced by the staggered gauge field respond to the local density as well. Predictions for time-of-flight experiments were included, indicating signature momentum distributions for the various predicted phases.

In chapter 6, we have seen how, in a 1D Bose gas with strong local interactions, incommensurability between the lattice potential and particle density immediately induces the transition from a Mott insulator to a superfluid, and can lead to translational symmetry-broken phase even in spite of the absence of long-range interactions in the original Hamiltonian. Without special features in the interactions that favour breaking the lattice symmetry, a density wave and even a supersolid phase nonetheless emerge, whose periodicities are unrelated to that of the underlying lattice. The physical mechanism behind this unexpected result is the effective interaction between the quasiparticles that are automatically present in the model

if the density is incommensurate with the lattice. Renormalisation group arguments show that quantum fluctuations lead to a long-range quasiparticle interaction proportional to the inverse distance squared, revealing the well-known Calogero-Sutherland model (CSM) as an effective description of the quasiparticle system. Known results for the CSM allowed us to propose a phase diagram for the original system of a strongly, but locally interacting bosonic gas in a weak optical lattice.

The four above-mentioned research projects, although each within the general topic of ultracold atomic gases in optical lattices with long-range interactions and/or periodic driving, are a relatively diverse collective. They combine bosonic and fermionic gases, weak and strong interactions, perturbative and mean-field approximations, effective field theories and exact diagonalisations. The main overall conclusion is that long-range interactions and high-frequency periodic driving lead to a very diverse range of fascinating phenomena in ultracold lattice gases.

7.2 Outlook

The research presented in chapters 3-6 will hopefully stimulate both experimental and theoretical research on the systems that were proposed to realise these phases. A variety of follow-up questions arises regarding the quantum phases and phase transitions discovered, some of which we will briefly sketch here.

An example of an experimental follow-up research project would be an experimental test of the predicted phases in the kinetically frustrated triangular lattice (chapter 4). The technically most accessible route would be to impose a triangular lattice (which has been generated, see *e.g.* [9, 10] - the shaking in Ref. [10] is not even required) on a dipolar fermionic gas, such as the one realised in Ref. [122], with a filling factor just below unity. In such a set-up, the holes experiece kinetic frustration, and inherit the long-range interactions from the fermionic particles. Given the pace at which these areas of research develop, such an experiment is certainly conceivable in the relatively near future.

Another prediction that would merit testing is the supersolid phase in the 1D strongly interacting incommensurable Bose gas in a weak optical lattice. Experiments on strongly interacting 1D Bose gases have been performed at commensurability (see Ref. [62]), implying that the same set-up could be used to test the density-wave predictions. In a recent publication, a high degree of control over the filling factors has been demonstrated (see Ref. [123]), bringing the possibility to test a commensurability-driven transition within experimental reach.

Apart from experimental follow-up research, numerous avenues for theoretical investigation also present themselves. One particularly interesting direction is suggested by the observation that many of the effects discussed in this thesis occur in regimes characterised by weak interactions, leaving the fascinating physics of strongly correlated systems unexplored. The project presented in chapter 5 has already been followed up elsewhere with an investigation into the strongly-interacting regime [124]. Investigating the hard-core limit of the model presented in chapter 3 is likely to reveal fascinating frustrated spin models. Starting from the results of chapter 4, further research on fermions in shaken lattices is expected to be a very fertile area, as exemplified by Ref. [16]. The effects of periodic driving on the system described in chapter 6 constitute another area of research with potentially very interesting results.

The specific projects mentioned above are only examples, and by no means a complete overview of the follow-up questions that could be addressed. We may conclude that the research in this thesis provides many starting points for interesting new projects.

Appendix A

Calculational details for kinetically frustrated spinless fermions

A.1 Density wave

Returning to Eq. (4.37), the quantities to be investigated are the averages $\langle c_{\mathbf{k}\pm\mathbf{Q}}^{\dagger} c_{\mathbf{k}} \rangle$ where $\mathbf{Q}$ is one of the three nesting vectors defined in section 4.3.1. Those vectors vectors happen to satisfy the condition that $2\mathbf{Q}_j$ is always a reciprocal lattice vector, such that $\mathbf{Q}_j = -\mathbf{Q}_j$ under reciprocal lattice symmetry. Hence, the two $\omega_{\mathbf{k}}^{\pm\mathbf{Q}}$-terms from Eq. (4.37) are in fact equivalent, and we only obtain one.

Order parameter

Defining

$$\rho_{\mathbf{Q}_j}^{\mathbf{a}} = \sum_{\mathbf{k}\in\mathrm{BZ}_1} \left\langle c_{\mathbf{k}+\mathbf{Q}_j}^{\dagger} c_{\mathbf{k}} \right\rangle e^{i\mathbf{k}\cdot\mathbf{a}}, \tag{A.1}$$

and formulating the order parameter equation (4.38) in momentum space, we find

$$\rho_j = \sum_{\mathbf{k} \in \mathrm{BZ}_1} \left\langle c^\dagger_{\mathbf{k}+\mathbf{Q}_j} c_{\mathbf{k}} \right\rangle = \rho^0_{\mathbf{Q}_j}, \tag{A.2}$$

and similarly, the total density $N = \rho^0_0$, and the current $\mathcal{J}_j = 2 \operatorname{Im} \rho^{\mathbf{a}_j}_0$. For later use, we define

$$\mathcal{J}_{j,l} = 2 J_j \operatorname{Im} \rho^{\mathbf{e}_j}_{\mathbf{Q}_l} \tag{A.3a}$$

$$D_{j,l} = 2 J_j \operatorname{Re} \rho^{\mathbf{e}_j}_{\mathbf{Q}_l} \tag{A.3b}$$

A.1.1 Mean-field Hamiltonian

The mean-field Hamiltonian is given by

$$
\begin{aligned}
H_{\mathrm{MF}} = & \sum_{\mathbf{k}} \xi_{\mathbf{k}} c^\dagger_{\mathbf{k}} c_{\mathbf{k}} \\
& + \sum_{\mathbf{k},\mathbf{p},\mathbf{q}} V(\mathbf{k}) \Big(\left\langle c^\dagger_{\mathbf{p}} c_{\mathbf{p}+\mathbf{k}} \right\rangle c^\dagger_{\mathbf{q}} c_{\mathbf{q}-\mathbf{k}} + \left\langle c^\dagger_{\mathbf{q}} c_{\mathbf{q}-\mathbf{k}} \right\rangle c^\dagger_{\mathbf{p}} c_{\mathbf{p}+\mathbf{k}} \\
& \qquad\qquad - \left\langle c^\dagger_{\mathbf{p}} c_{\mathbf{q}-\mathbf{k}} \right\rangle c^\dagger_{\mathbf{q}} c_{\mathbf{p}+\mathbf{k}} - \left\langle c^\dagger_{\mathbf{q}} c_{\mathbf{p}+\mathbf{k}} \right\rangle c^\dagger_{\mathbf{p}} c_{\mathbf{q}-\mathbf{k}} \\
& \qquad\qquad - \left\langle c^\dagger_{\mathbf{p}} c_{\mathbf{p}+\mathbf{k}} \right\rangle \left\langle c^\dagger_{\mathbf{q}} c_{\mathbf{q}-\mathbf{k}} \right\rangle + \left\langle c^\dagger_{\mathbf{p}} c_{\mathbf{q}-\mathbf{k}} \right\rangle \left\langle c^\dagger_{\mathbf{q}} c_{\mathbf{p}+\mathbf{k}} \right\rangle \Big)
\end{aligned}
\tag{A.4}
$$

(the subscript $_{\mathrm{MF}}$ will be omitted from here on, since the entire calculation takes place within the mean-field approximation). Inserting Eq. (4.37) and investigating the term for $\mathbf{Q}_j = \mathbf{Q}$ yields

$$
\begin{aligned}
& \sum_{\mathbf{k},\mathbf{p},\mathbf{q}} V(\mathbf{k}) \Big(\delta_{-\mathbf{k},\mathbf{Q}} n^{\mathbf{Q}}_{\mathbf{p}+\mathbf{k}} c^\dagger_{\mathbf{q}} c_{\mathbf{q}-\mathbf{k}} + \delta_{\mathbf{k},\mathbf{Q}} n^{\mathbf{Q}}_{\mathbf{q}-\mathbf{k}} c^\dagger_{\mathbf{p}} c_{\mathbf{p}+\mathbf{k}} \\
& \qquad\qquad - \delta_{\mathbf{p}-\mathbf{q}+\mathbf{k},\mathbf{Q}} n^{\mathbf{Q}}_{\mathbf{q}-\mathbf{k}} c^\dagger_{\mathbf{q}} c_{\mathbf{p}+\mathbf{k}} - \delta_{\mathbf{q}-\mathbf{p}-\mathbf{k},\mathbf{Q}} n^{\mathbf{Q}}_{\mathbf{p}+\mathbf{k}} c^\dagger_{\mathbf{p}} c_{\mathbf{q}-\mathbf{k}} \Big) \\
= & \; 2 \sum_{\mathbf{k},\mathbf{p}} \Big[V(\mathbf{Q}) n^{\mathbf{Q}}_{\mathbf{p}-\mathbf{Q}} - V(\mathbf{Q}-\mathbf{p}+\mathbf{k}) n^{\mathbf{Q}}_{\mathbf{p}-\mathbf{Q}} \Big] c^\dagger_{\mathbf{k}} c_{\mathbf{k}+\mathbf{Q}} \\
= & -2 \sum_{\mathbf{k},\mathbf{p}} \Big[V(\mathbf{k}-\mathbf{p}-\mathbf{Q}) - V(\mathbf{Q}) \Big] n^{\mathbf{Q}}_{\mathbf{p}} c^\dagger_{\mathbf{k}-\mathbf{Q}} c_{\mathbf{k}} = \sum_{\mathbf{k}} \omega^{\mathbf{Q}}_{\mathbf{k}} c^\dagger_{\mathbf{k}-\mathbf{Q}} c_{\mathbf{k}},
\end{aligned}
\tag{A.5}
$$

where

$$\omega_{\mathbf{k}}^{\mathbf{Q}_j} = 2V(\mathbf{Q}_j) \sum_{\mathbf{p}\in\mathrm{BZ}_1} \left\langle c_{\mathbf{p}+\mathbf{Q}_j}^\dagger c_{\mathbf{p}} \right\rangle - 2 \sum_{\mathbf{p}\in\mathrm{BZ}_1} V(\mathbf{k}-\mathbf{p}+\mathbf{Q}) \left\langle c_{\mathbf{p}+\mathbf{Q}_j}^\dagger c_{\mathbf{p}} \right\rangle.$$

(A.6)

With the help of Eq. (A.1), we can rewrite $\omega_{\mathbf{k}}^{\mathbf{Q}_j}$ as

$$\omega_{\mathbf{k}}^{\mathbf{Q}_j} = 2V(\mathbf{Q}_j)\rho_{\mathbf{Q}_j}^0 - U \sum_l \left(\rho_{\mathbf{Q}_j}^{\mathbf{e}_l} e^{-i(\mathbf{k}-\mathbf{Q}_j)\cdot\mathbf{e}_l} + \rho_{\mathbf{Q}_j}^{-\mathbf{e}_l} e^{i(\mathbf{k}-\mathbf{Q}_j)\cdot\mathbf{e}_l} \right), \quad \text{(A.7)}$$

where $\mathbf{a}$ are the displacement vectors. Let us, for later use, cast it in terms of ρ_j and the six other parameters defined in Eq. (A.3):

$$\begin{aligned}
\omega_{\mathbf{k}}^{\mathbf{Q}_j} &= 2V(\mathbf{Q}_j)\rho_j - U \sum_l \left(\rho_{\mathbf{Q}_j}^{\mathbf{e}_j} e^{-i(\mathbf{k}-\mathbf{Q}_j)\cdot\mathbf{e}_l} + \rho_{\mathbf{Q}_j}^{-\mathbf{a}_l} e^{i(\mathbf{k}-\mathbf{Q}_j)\cdot\mathbf{e}_l} \right) \\
&= 2V(\mathbf{Q}_j)\rho_j - U \sum_l \Big[(D_{j,l} + i\mathcal{J}_{j,l}) e^{-i(\mathbf{k}-\mathbf{Q}_j)\cdot\mathbf{e}_l} \\
&\qquad\qquad\qquad\qquad + (D_{j,l} - i\mathcal{J}_{j,l}) e^{i(\mathbf{k}-2\mathbf{Q})_j\cdot\mathbf{e}_l} \Big] \\
&= 2V(\mathbf{Q}_j)\rho_j - U \sum_l \Big[D_{j,l} \big(e^{-i\mathbf{k}\cdot\mathbf{e}_l} e^{i\mathbf{Q}_j\cdot\mathbf{e}_l} + e^{i\mathbf{k}\cdot\mathbf{e}_l} \big) \\
&\qquad\qquad\qquad\qquad + i\mathcal{J}_{j,l} \big(e^{-i\mathbf{k}\cdot\mathbf{e}_l} e^{i\mathbf{Q}_j\cdot\mathbf{e}_l} - e^{i\mathbf{k}\cdot\mathbf{e}_l} \big) \Big].
\end{aligned}$$

(A.8)

We have already made use of the fact that $2\mathbf{Q}\cdot\mathbf{a} = 0$ under the reciprocal lattice symmetry for any of the nesting vectors $\mathbf{Q}$ and any nn (or other) lattice vector $\mathbf{a}$. However, we also know that for $\mathbf{Q} \parallel \mathbf{a}$, the inner product $\mathbf{Q}\cdot\mathbf{a} = 0$, and that in the other two cases, $\mathbf{Q}\cdot\mathbf{a} = \pi$.

$$\begin{aligned}
\omega_{\mathbf{k}}^{\mathbf{Q}_j} &= 2V(\mathbf{Q}_j)\rho_j - 2U \Big[D_{j,j} \cos(\mathbf{k}\cdot\mathbf{e}_j) + \mathcal{J}_{j,j} \sin(\mathbf{k}\cdot\mathbf{e}_j) \Big] \\
&\quad - 2iU \sum_{l\neq j} \Big[D_{j,l} \sin(\mathbf{k}\cdot\mathbf{e}_l) - \mathcal{J}_{j,l} \cos(\mathbf{k}\cdot\mathbf{e}_l) \Big].
\end{aligned}$$

(A.9)

The total mean-field Hamiltonian can now be cast into the form

$$H = \sum_{\mathbf{k}} \left[\omega_{\mathbf{k}} c_{\mathbf{k}}^{\dagger} c_{\mathbf{k}} + \sum_{j} \left(\omega_{\mathbf{k}}^{\mathbf{Q}_j} c_{\mathbf{k}-\mathbf{Q}_j}^{\dagger} c_{\mathbf{k}} + \omega_{\mathbf{k}}^{-\mathbf{Q}_j} c_{\mathbf{k}+\mathbf{Q}_j}^{\dagger} c_{\mathbf{k}} \right) \right] + \text{constant}$$

$$= \sum_{\mathbf{k}} \left[\omega_{\mathbf{k}} \hat{n}_{\mathbf{k}} + \sum_{j} \left(\omega_{\mathbf{k}}^{\mathbf{Q}_j} \hat{n}_{\mathbf{k}}^{-\mathbf{Q}_j} + \omega_{\mathbf{k}}^{-\mathbf{Q}_j} \hat{n}_{\mathbf{k}}^{\mathbf{Q}_j} \right) \right] + \text{constant}. \qquad (A.10)$$

Although the last line shows a physically intuitive form for the Hamiltonian, it is not diagonal, which we need to calculate the free energy corresponding to this mean-field approximation, given by

$$F = -\frac{1}{\beta} \ln Z. \qquad (A.11)$$

The constant term in H shows up unchanged in the free energy, but to calculate the contribution from the parts that are quadratic in the $c^{(\dagger)}$-operators, we need the eigenstates of the Hamiltonian. First, let us rewrite the constant term:

$$C = \sum_{\mathbf{k},\mathbf{p},\mathbf{q}} V(\mathbf{k}) \left(- \left\langle c_{\mathbf{p}}^{\dagger} c_{\mathbf{p}+\mathbf{k}} \right\rangle \left\langle c_{\mathbf{q}}^{\dagger} c_{\mathbf{q}-\mathbf{k}} \right\rangle + \left\langle c_{\mathbf{p}}^{\dagger} c_{\mathbf{q}-\mathbf{k}} \right\rangle \left\langle c_{\mathbf{q}}^{\dagger} c_{\mathbf{p}+\mathbf{k}} \right\rangle \right) \qquad (A.12)$$

$$= - N^2 V(0) - \sum_{j} \rho_j^2 V(\mathbf{Q}_j) + \frac{U}{4} \sum_{j} \left[\mathcal{J}_j^2 + D_j^2 + \sum_{l} \left(\mathcal{J}_{j,l}^2 + D_{j,l}^2 \right) \right].$$

A.1.2 Partition function / Green's function method

Now we turn to diagonalising the mean-field Hamiltonian from Eq. (A.10). One approach would be to write it in matrix form such that all terms related to each other by a momentum shift of one of the $\mathbf{Q}_j$ are in the same matrix. This results in a 4×4-matrix, of which the eigenvalues are unfortunately not easily obtainable in tractable form by analytical calculations. To get around this problem, we will use perturbation theory, treating the DW-related terms in the Hamiltonian as a perturbation. To take the temperature dependence of the free energy into account, we will use the imaginary-time formalism. We will base the following derivations

on Ref. [125]; the formalism can also be found in most other textbooks on statistical field theory.

Green's function method

We start by a Legendre transform from Hamiltonian to action, replacing the operators $c_{\mathbf{k}}$ by Grassmann fields $\phi_{\mathbf{k}}(\tau)$ that depend on imaginary time τ. For the details and the reasoning that leads to this point, see e.g. Ref. [125], chapter 7. The action obtained this way from the mean-field Hamiltonian in Eq. (A.10) reads:

$$
S[\phi, \phi^*] = \int_0^{\hbar\beta} d\tau \sum_{\mathbf{k}\in BZ_1} \left[\phi_{\mathbf{k}}^*(\tau)\left(\frac{\partial}{\partial\tau} + \omega_{\mathbf{k}}\right)\phi_{\mathbf{k}}(\tau) + \sum_j \omega_{\mathbf{k}}^{\mathbf{Q}_j}\phi_{\mathbf{k}}^*(\tau)\phi_{\mathbf{k}+\mathbf{Q}_j}(\tau) \right]
$$
$$
+ \hbar\beta C. \tag{A.13}
$$

Next, we perform a Fourier transform with respect to imaginary time τ,

$$
\phi(\tau) = \frac{1}{\sqrt{\hbar\beta}} \sum_{n=-\infty}^{\infty} \tilde{\phi}_n e^{-i\omega_n\tau}, \tag{A.14a}
$$

$$
\omega_n = 2\pi(2n+1)/\hbar\beta, \tag{A.14b}
$$

$$
S[\phi, \phi^*] = \sum_{\mathbf{k},n} \left[\phi_{\mathbf{k},n}^*(-i\hbar\omega_n + \omega_{\mathbf{k}})\phi_{\mathbf{k},n} + \sum_j \omega_{\mathbf{k}}^{\mathbf{Q}_j}\phi_{\mathbf{k},n}^*\phi_{\mathbf{k}+\mathbf{Q}_j,n} \right] + \hbar\beta C
$$
$$
= S_0[\phi, \phi^*] + S_W[\phi, \phi^*] + \hbar\beta C, \tag{A.14c}
$$

after the partition function reads

$$
Z = \int \mathcal{D}\phi\mathcal{D}\phi^* \, e^{-S[\phi,\phi^*]/\hbar} = \int \mathcal{D}\phi\mathcal{D}\phi^* \, e^{-S_0[\phi,\phi^*]/\hbar} e^{-S_W[\phi,\phi^*]/\hbar} e^{-\beta C}. \tag{A.15}
$$

We can write the spatially homogeneous part as follows:

$$
Z_0 = \int \mathcal{D}\phi\mathcal{D}\phi^* \, \exp\left\{ -\frac{1}{\hbar}\sum_{\mathbf{k},\mathbf{k}'}\sum_{n,n'} \phi_{\mathbf{k},n}^* G_{\mathbf{k},\mathbf{k}',n,n'}^{-1}\phi_{\mathbf{k}',n'} \right\}, \tag{A.16}
$$

where G is a diagonal matrix in both Matsubara frequency space and momentum space, mathematically speaking a Green's function:

$$(-i\hbar\omega_n + \omega_{\mathbf{k}})G_{\mathbf{k},\mathbf{k}',n,n'} = -\hbar\delta_{\mathbf{k},\mathbf{k}'}\delta_{n,n'}. \tag{A.17}$$

In the quadratic and diagonal case, it is rather easy to find the expression for G: we simply have to multiply the required Kronecker deltas with the appropriate coefficient:

$$G_{\mathbf{k},\mathbf{k}',n,n'} = G_{\mathbf{k},n}\delta_{\mathbf{k},\mathbf{k}'}\delta_{n,n'} = \frac{-\hbar}{-i\hbar\omega_n + \omega_{\mathbf{k}}}\delta_{\mathbf{k},\mathbf{k}'}\delta_{n,n'}. \tag{A.18}$$

Inserting this last identity into the equation for Z_0 above does indeed give the result we expected; all of this is rather trivial. The point is that now, we have the whole problem formulated in terms of fields, path integrals, and Green's functions.

Spatially homogeneous part

Now, let us first consider what this means for the staggered currents. Setting $\omega_{\mathbf{k}}^{\mathbf{Q}_j} = 0$, we also have $S_W = 0$, and the free energy yields:

$$\begin{aligned}
F &= -\frac{1}{\beta}\ln Z_0 + C = -\frac{1}{\beta}\ln\int\mathcal{D}\phi\mathcal{D}\phi^*\,e^{-S_0[\phi,\phi^*]/\hbar} + C \\
&= \sum_{\mathbf{k}\in\mathrm{BZ}_1}\ln(1 + e^{-\beta\omega_{\mathbf{k}}}) + C.
\end{aligned} \tag{A.19}$$

We had found this before, so performing the Ginzburg-Landau expansion in the order parameters for the time-reversal symmetry breaking phase transition will not yield any different results from what we already had.

Perturbation theory

Now for the density wave. Instead of setting $S_W = 0$ in Eq. (A.15), we treat it perturbatively by expanding the exponential:

$$Z = e^{-\beta C}\int\mathcal{D}\phi\mathcal{D}\phi^*\,e^{-S_0[\phi,\phi^*]/\hbar}\sum_{n=0}^{\infty}\frac{(-S_W)^n}{\hbar^n n!}. \tag{A.20}$$

This identity for the partition function can be rewritten as

$$Z = e^{-\beta C} Z_0 \sum_{n=0}^{\infty} \frac{(-1)^n \langle S_W^n \rangle_0}{\hbar^n n!}. \tag{A.21}$$

Now we can apply Wick's theorem to calculate the averages. We will go up to fourth order (i.e. to $n = 4$ in Eq. (A.21)), because we are interested in terms of up to order four for the Ginzburg-Landau expansion. For $\langle S_W \rangle_0$, we find

$$
\begin{aligned}
\langle S_W \rangle_0 &= \sum_{j} \sum_{\mathbf{k},n} \omega_{\mathbf{k}}^{\mathbf{Q}_j} \left\langle \phi_{\mathbf{k},n}^* \phi_{\mathbf{k}+\mathbf{Q}_j,n} \right\rangle \\
&= \sum_{j} \sum_{\mathbf{k},n} \omega_{\mathbf{k}}^{\mathbf{Q}_j} G_{\mathbf{k},\mathbf{k}+\mathbf{Q}_j,n,n} = 0
\end{aligned}
\tag{A.22}
$$

since $G_{\mathbf{k},\mathbf{k}',n,n'} \propto \delta_{\mathbf{k},\mathbf{k}'}\delta_{n,n'}$ as can be seen in Eq. (A.18). (See Ref. [125], chapter 8 for the details of how to evaluate the quadratic average.) For the second-order term, we find

$$
\begin{aligned}
\langle S_W^2 \rangle_0 &= \sum_{j,j'} \sum_{\mathbf{k},n} \sum_{\mathbf{k}',n'} \omega_{\mathbf{k}}^{\mathbf{Q}_j} \omega_{\mathbf{k}'}^{\mathbf{Q}_{j'}} \left\langle \phi_{\mathbf{k},n}^* \phi_{\mathbf{k}+\mathbf{Q}_j,n} \phi_{\mathbf{k}',n'}^* \phi_{\mathbf{k}'+\mathbf{Q}_{j'}',n'} \right\rangle_0 \\
&= -\sum_{j,j'} \sum_{\mathbf{k},n} \sum_{\mathbf{k}',n'} \omega_{\mathbf{k}}^{\mathbf{Q}_j} \omega_{\mathbf{k}'}^{\mathbf{Q}_{j'}} \left\langle \phi_{\mathbf{k},n}^* \phi_{\mathbf{k}'+\mathbf{Q}_{j'}',n'} \right\rangle_0 \left\langle \phi_{\mathbf{k}',n'}^* \phi_{\mathbf{k}+\mathbf{Q}_j,n} \right\rangle_0 \\
&= -\sum_{j,\mathbf{k}} \omega_{\mathbf{k}}^{\mathbf{Q}_j} \omega_{\mathbf{k}+\mathbf{Q}_j}^{\mathbf{Q}_j} \sum_{n} G_{\mathbf{k},n} G_{\mathbf{k}+\mathbf{Q}_j,n} \\
&= -\sum_{j,\mathbf{k}} |\omega_{\mathbf{k}}^{\mathbf{Q}_j}|^2 \Delta_{\mathbf{k},j},
\end{aligned}
\tag{A.23}
$$

where we have defined

$$\Delta_{\mathbf{k},j} = \sum_{n} G_{\mathbf{k},n} G_{\mathbf{k}+\mathbf{Q}_j,n} = \frac{\tanh(\beta\omega_{\mathbf{k}+\mathbf{Q}_j}/2) - \tanh(\beta\omega_{\mathbf{k}}/2)}{\omega_{\mathbf{k}} - \omega_{\mathbf{k}+\mathbf{Q}_j}}. \tag{A.24}$$

In the first step, we have omitted terms that would yield zero by virtue of the result for $\langle S_W \rangle_0$, while in the last step, we made use of the fact that

$(\omega_{\mathbf{k}}^{\mathbf{Q}})^* = \omega_{\mathbf{k}+\mathbf{Q}}^{\mathbf{Q}}$. For the third-order term, we find

$$
\begin{aligned}
\langle S_W^3 \rangle_0 &= \sum_{j,j',j''} \sum_{\mathbf{k},n} \sum_{\mathbf{k}',n'} \sum_{\mathbf{k}'',n''} \omega_{\mathbf{k}}^{\mathbf{Q}_j} \omega_{\mathbf{k}'}^{\mathbf{Q}_{j'}} \omega_{\mathbf{k}''}^{\mathbf{Q}_{j''}} \times \\
&\quad \times \left\langle \phi_{\mathbf{k},n}^* \phi_{\mathbf{k}+\mathbf{Q}_j,n} \phi_{\mathbf{k}',n'}^* \phi_{\mathbf{k}'+\mathbf{Q}_j',n'} \phi_{\mathbf{k}'',n''}^* \phi_{\mathbf{k}''+\mathbf{Q}_j'',n''} \right\rangle_0 \\
&= \sum_{j,j',j''} \sum_{\mathbf{k},n} \sum_{\mathbf{k}',n'} \sum_{\mathbf{k}'',n''} \omega_{\mathbf{k}}^{\mathbf{Q}_j} \omega_{\mathbf{k}'}^{\mathbf{Q}_{j'}} \omega_{\mathbf{k}''}^{\mathbf{Q}_{j''}} \times \\
&\quad \times \Big(G_{\mathbf{k},\mathbf{k}'+\mathbf{Q}',n,n'} G_{\mathbf{k}',\mathbf{k}''+\mathbf{Q}'',n',n''} G_{\mathbf{k}'',\mathbf{k}+\mathbf{Q},n'',n} \\
&\qquad + G_{\mathbf{k},\mathbf{k}''+\mathbf{Q}'',n,n''} G_{\mathbf{k}'',\mathbf{k}'+\mathbf{Q}',n'',n'} G_{\mathbf{k}',\mathbf{k}+\mathbf{Q},n',n} \Big) \\
&= 2 \sum_{j \neq k \neq l} \sum_{\mathbf{k},n} \omega_{\mathbf{k}}^{\mathbf{Q}_j} \omega_{\mathbf{k}+\mathbf{Q}_j}^{\mathbf{Q}_k} \omega_{\mathbf{k}+\mathbf{Q}_k}^{\mathbf{Q}_l} G_{\mathbf{k}+\mathbf{Q}_j,n} G_{\mathbf{k}+\mathbf{Q}_l,n} G_{\mathbf{k}+\mathbf{Q}_k,n} \\
&= 12 \sum_{\mathbf{k}} \omega_{\mathbf{k}}^{\mathbf{Q}_1} \omega_{\mathbf{k}+\mathbf{Q}_1}^{\mathbf{Q}_2} \omega_{\mathbf{k}+\mathbf{Q}_2}^{\mathbf{Q}_3} \Xi_{\mathbf{k}},
\end{aligned}
\tag{A.25}
$$

where we have again omitted terms that would yield zero after the first step, and analytically performed the sum over the Matsubara frequencies:

$$
\begin{aligned}
\Xi_{\mathbf{k}} &= \sum_n G_{\mathbf{k}+\mathbf{Q}_j,n} G_{\mathbf{k}+\mathbf{Q}_l,n} G_{\mathbf{k}+\mathbf{Q}_k,n} \\
&= 3 \frac{-\tanh(\beta \omega_{\mathbf{k}}/2)}{(\omega_{\mathbf{k}} - \omega_{\mathbf{k}+\mathbf{Q}_j})(\omega_{\mathbf{k}} - \omega_{\mathbf{k}+\mathbf{Q}_l})}.
\end{aligned}
\tag{A.26}
$$

A.1.3 Expansion of F

We can now perform a Ginzburg-Landau expansion of the free energy in the order parameters. Since ρ_j is real, only the real part of $\omega_{\mathbf{k}}^{\mathbf{Q}}$ turns out to matter for the second-order terms. Furthermore, we note that $\Delta_{\mathbf{k}} = \Delta_{-\mathbf{k}}$, and that hence, only the even part of $(\operatorname{Re} \omega_{\mathbf{k}}^{\mathbf{Q}})^2$ survives. Consulting Eq. (A.9), we find that only $D_{j,j}$ couples to ρ_j. Hence, to second order, the

GL expansion takes the form

$$F \approx F_0 + \sum_j \begin{bmatrix} \rho_j & D_j \end{bmatrix} \begin{bmatrix} \alpha_{\mathrm{DW}}^{\rho} & \gamma_{\mathrm{DW}} \\ \gamma_{\mathrm{DW}} & \alpha_{\mathrm{DW}}^{D} \end{bmatrix} \begin{bmatrix} \rho_j \\ \tilde{D}_j \end{bmatrix} \tag{A.27}$$

$$+ \Gamma^{\rho} \rho_1 \rho_2 \rho_3 + \text{other 3rd and higher order terms.}$$

The quadratic terms have contributions from both the perturbations and the constant C:

$$\alpha_{\mathrm{DW}}^{\rho} = -V(\mathbf{Q}_j) \left[1 - 2V(\mathbf{Q}_j) \sum_{\mathbf{k}} \frac{\tanh(\beta\omega_{\mathbf{k}+\mathbf{Q}_j}/2) - \tanh(\beta\omega_{\mathbf{k}}/2)}{\omega_{\mathbf{k}} - \omega_{\mathbf{k}+\mathbf{Q}_j}} \right]$$

$$\alpha_{\mathrm{DW}}^{D} = -U \left[1 - 2U \sum_{\mathbf{k}} \cos^2(\mathbf{k} \cdot \mathbf{e}_j) \frac{\tanh(\beta\omega_{\mathbf{k}+\mathbf{Q}_j}/2) - \tanh(\beta\omega_{\mathbf{k}}/2)}{\omega_{\mathbf{k}} - \omega_{\mathbf{k}+\mathbf{Q}_j}} \right] \tag{A.28}$$

Since C only has terms quadratic in ρ_j, it does not contribute to any of the higher-order terms in the GL expansion. For the trilinear term, we find

$$\Gamma^{\rho} = 12V(\mathbf{Q}_1)V(\mathbf{Q}_2)V(\mathbf{Q}_3) \sum_{\mathbf{k}} \frac{-\tanh(\beta\omega_{\mathbf{k}}/2)}{(\omega_{\mathbf{k}} - \omega_{\mathbf{k}+\mathbf{Q}_j})(\omega_{\mathbf{k}} - \omega_{\mathbf{k}+\mathbf{Q}_l})}. \tag{A.29}$$

The other third-order terms feature between one and three cosines multiplying the summand of Γ^{ρ}, and are all significantly smaller than Γ^{ρ} itself.

A.1.4 Interaction between SC and DW

We know that all terms of first order in one of the order parameters vanish (except for the three-way interaction term between the three DWs), so the first term of interest is the one that is of second order in both the SC and DW order parameters. This is obtained by expanding the second-order DW term in terms of $\mathcal{J}$. The first derivative gives:

$$\frac{\partial \alpha_{\mathrm{DW}}}{\partial \mathcal{J}_l} = 2V^2(\mathbf{Q}_j) \sum_{\mathbf{k}} \frac{\partial}{\partial \mathcal{J}_l} \frac{\tanh(\beta\omega_{\mathbf{k}+\mathbf{Q}_j}/2) - \tanh(\beta\omega_{\mathbf{k}}/2)}{\omega_{\mathbf{k}} - \omega_{\mathbf{k}-\mathbf{Q}_j}}, \tag{A.30}$$

which vanishes at $\mathcal{J} = 0$. Let us consider the second derivative:

$$
\begin{aligned}
\frac{\partial^2 \alpha_{\mathrm{DW}}^j}{\partial \mathcal{J}_j^2} &= V^2(\mathbf{Q}_j) \frac{(U\beta)^2 \sin^2(\mathbf{k} \cdot \mathbf{e}_j)}{\omega_{\mathbf{k}} - \omega_{\mathbf{k}+\mathbf{Q}_j}} \left(\frac{x_{\mathbf{k}+\mathbf{Q}_j}}{y_{\mathbf{k}+\mathbf{Q}_j}^2} - \frac{x_{\mathbf{k}}}{y_{\mathbf{k}}^2} \right) \\
\frac{\partial^2 \alpha_{\mathrm{DW}}^j}{\partial \mathcal{J}_l^2} &= V^2(\mathbf{Q}_j) \frac{(U\beta)^2 \sin^2(\mathbf{k} \cdot \mathbf{e}_l)}{\omega_{\mathbf{k}} - \omega_{\mathbf{k}+\mathbf{Q}_j}} \left(\frac{x_{\mathbf{k}+\mathbf{Q}_j}}{y_{\mathbf{k}+\mathbf{Q}_j}^2} - \frac{x_{\mathbf{k}}}{y_{\mathbf{k}}^2} \right) \\
&\quad - 4V^2(\mathbf{Q}_j) \frac{\beta U^2 \sin^2(\mathbf{k} \cdot \mathbf{e}_l)}{(\omega_{\mathbf{k}} - \omega_{\mathbf{k}+\mathbf{Q}_j})^2} \left(\frac{1}{y_{\mathbf{k}}^2} + \frac{1}{y_{\mathbf{k}+\mathbf{Q}_j}^2} \right) \\
&\quad + 8V^2(\mathbf{Q}_j) \frac{U^2 \sin^2(\mathbf{k} \cdot \mathbf{e}_l)}{(\omega_{\mathbf{k}} - \omega_{\mathbf{k}+\mathbf{Q}_j})^3} (x_{\mathbf{k}} - x_{\mathbf{k}+\mathbf{Q}_j}),
\end{aligned} \tag{A.31}
$$

where

$$
\begin{aligned}
x_{\mathbf{k}} &= \tanh(\beta \omega_{\mathbf{k}}/2) \\
y_{\mathbf{k}} &= \cosh(\beta \omega_{\mathbf{k}}/2).
\end{aligned} \tag{A.32}
$$

The combined effect of these terms is a repulsion between the density wave and the staggered currents. Taking into account the term quadratic in both $D_{j,j}$ and $\mathcal{J}_{j/l}$ does not change the nature of this interaction.

A.2 Modulated currents

To calculate the phase boundaries of the modulated currents, we go back to the evaluation of $\omega_{\mathbf{k}}^{\mathbf{Q}_j}$, and consider the parameters $\mathcal{J}_{j,l}$. Writing out the whole $|\omega_{\mathbf{k}}^{\mathbf{Q}_j}|^2$-term, we obtain

$$
\sum_{\mathbf{k}} |\omega_{\mathbf{k}}^{\mathbf{Q}_j}|^2 \Delta_{\mathbf{k}} = \sum_{n,n'} V_n^T (A_j)_{nn'} V_{n'}, \tag{A.33}
$$

where

$$
V^T = \begin{bmatrix} \rho_j & D_{j,j} & D_{j,j'} & D_{j,j''} & \mathcal{J}_{j,j} & \mathcal{J}_{j,j'} & \mathcal{J}_{j,j''} \end{bmatrix} \tag{A.34}
$$

and A_j is a 7×7 matrix, which due to the considerations above takes the form

$$
A_j =
\begin{bmatrix}
\alpha_{\rho\rho} & \alpha_{\rho D}^{\,j} & & & \alpha_{\rho\mathcal{J}}^{\,j} & & \\
\alpha_{D\rho}^{\,j} & \alpha_{DD}^{\,jj} & & & \alpha_{D\mathcal{J}}^{\,jj} & & \\
& & \alpha_{DD}^{j'j'} & \alpha_{DD}^{j'j''} & & \alpha_{D\mathcal{J}}^{j'j'} & \alpha_{D\mathcal{J}}^{j'j''} \\
& & \alpha_{DD}^{j''j'} & \alpha_{DD}^{j''j''} & & \alpha_{D\mathcal{J}}^{j''j'} & \alpha_{D\mathcal{J}}^{j''j''} \\
\alpha_{\mathcal{J}\rho}^{\,j} & \alpha_{\mathcal{J}D}^{\,jj} & & & \alpha_{\mathcal{J}\mathcal{J}}^{\,jj} & & \\
& & \alpha_{\mathcal{J}D}^{j'j'} & \alpha_{\mathcal{J}D}^{j''j'} & & \alpha_{\mathcal{J}\mathcal{J}}^{j'j'} & \alpha_{\mathcal{J}\mathcal{J}}^{j'j''} \\
& & \alpha_{\mathcal{J}D}^{j''j'} & \alpha_{\mathcal{J}D}^{j''j''} & & \alpha_{\mathcal{J}\mathcal{J}}^{j''j'} & \alpha_{\mathcal{J}\mathcal{J}}^{j''j''}
\end{bmatrix}.
\tag{A.35}
$$

This matrix is real and symmetric. Further symmetry considerations allow us to reduce the number of different matrix elements to 12:

$$
\begin{aligned}
&\alpha_{\rho\mathcal{J}}^{\,j} = \alpha_{\mathcal{J}\rho}^{\,j}; \quad \alpha_{\rho D}^{\,j} = \alpha_{D\rho}^{\,j}; \quad \alpha_{\mathcal{J}D}^{jj} = \alpha_{D\mathcal{J}}^{jj}; \\
&\alpha_{\mathcal{J}\mathcal{J}}^{j'j'} = \alpha_{\mathcal{J}\mathcal{J}}^{j''j''}; \quad \alpha_{DD}^{j'j'} = \alpha_{DD}^{j''j''}; \quad \alpha_{\mathcal{J}D}^{j'j'} = \alpha_{D\mathcal{J}}^{j'j'} = \alpha_{\mathcal{J}D}^{j''j''} = \alpha_{D\mathcal{J}}^{j''j''}; \quad \text{(A.36)} \\
&\alpha_{\mathcal{J}D}^{j'j''} = \alpha_{D\mathcal{J}}^{j'j''}; \quad \alpha_{..}^{j''j'} = \alpha_{..}^{j'j''}.
\end{aligned}
$$

We have the following identities for the matrix elements of A_j:

$$
\alpha_{\rho\rho} = - \left[2V(\mathbf{Q})\right]^2 \sum_{\mathbf{k}} \Delta_{\mathbf{k}}
$$

$$
\alpha_{\rho\mathcal{J}}^{\,j} = 2V(\mathbf{Q})U \sum_{\mathbf{k}} \sin(\mathbf{k}\cdot\mathbf{e}_j)\Delta_{\mathbf{k}}; \qquad \alpha_{\rho D}^{\,j} = 2V(\mathbf{Q})U \sum_{\mathbf{k}} \cos(\mathbf{k}\cdot\mathbf{e}_j)\Delta_{\mathbf{k}}
$$

$$
\alpha_{\mathcal{J}\mathcal{J}}^{jj} = - 4U^2 \sum_{\mathbf{k}} \sin^2(\mathbf{k}\cdot\mathbf{e}_j)\Delta_{\mathbf{k}}; \qquad \alpha_{DD}^{jj} = -4U^2 \sum_{\mathbf{k}} \cos^2(\mathbf{k}\cdot\mathbf{e}_j)\Delta_{\mathbf{k}}
$$

$$
\alpha_{\mathcal{J}D}^{jj} = - 4U^2 \sum_{\mathbf{k}} \sin(\mathbf{k}\cdot\mathbf{e}_j)\cos(\mathbf{k}\cdot\mathbf{e}_j)\Delta_{\mathbf{k}}
\tag{A.37}
$$

$$
\alpha_{\mathcal{J}\mathcal{J}}^{j'j'} = - 4U^2 \sum_{\mathbf{k}} \sin^2(\mathbf{k}\cdot\mathbf{e}_{j'})\Delta_{\mathbf{k}}; \qquad \alpha_{DD}^{j'j'} = -4U^2 \sum_{\mathbf{k}} \cos^2(\mathbf{k}\cdot\mathbf{e}_{j'})\Delta_{\mathbf{k}}
$$

$$
\alpha_{\mathcal{J}D}^{j'j'} = - 4U^2 \sum_{\mathbf{k}} \sin(\mathbf{k}\cdot\mathbf{e}_{j'})\cos(\mathbf{k}\cdot\mathbf{e}_{j'})\Delta_{\mathbf{k}}
$$

$$\alpha^{j'j''}_{\mathcal{J}\mathcal{J}} = -4U^2 \sum_{\mathbf{k}} \sin(\mathbf{k} \cdot \mathbf{e}_{j'}) \sin(\mathbf{k} \cdot \mathbf{e}_{j''}) \Delta_{\mathbf{k}}$$

$$\alpha^{j'j''}_{DD} = -4U^2 \sum_{\mathbf{k}} \cos(\mathbf{k} \cdot \mathbf{e}_{j'}) \cos(\mathbf{k} \cdot \mathbf{e}_{j''}) \Delta_{\mathbf{k}}$$

$$\alpha^{j'j''}_{\mathcal{J}D} = -4U^2 \sum_{\mathbf{k}} \sin(\mathbf{k} \cdot \mathbf{e}_{j'}) \cos(\mathbf{k} \cdot \mathbf{e}_{j''}) \Delta_{\mathbf{k}}.$$

Observing that $\Delta_{\mathbf{k}} = \Delta_{-\mathbf{k}}$, we can eliminate more coefficients: the matrix is given by

$$A_j = \begin{bmatrix} \alpha_{\rho\rho} & \alpha^1_{\rho D} & & & & & & \\ \alpha^1_{D\rho} & \alpha^{jj}_{DD} & & & & & & \\ & & \alpha^{j'j'}_{DD} & \alpha^{j'j''}_{DD} & & & & \\ & & \alpha^{j''j'}_{DD} & \alpha^{j''j''}_{DD} & & & & \\ & & & & \alpha^{jj}_{\mathcal{J}\mathcal{J}} & & & \\ & & & & & \alpha^{j'j'}_{\mathcal{J}\mathcal{J}} & \alpha^{j'j''}_{\mathcal{J}\mathcal{J}} \\ & & & & & \alpha^{j''j'}_{\mathcal{J}\mathcal{J}} & \alpha^{j''j''}_{\mathcal{J}\mathcal{J}} \end{bmatrix} \tag{A.38}$$

Clearly, the currents along the modulation direction appear by themselves. The self-energy terms $D_{j,j'}$ and $D_{j,j''}$ only couple to each other and are hence irrelevant at second order. The self-energy term $D_{j,j}$ is relevant for the static density wave, as discussed in the previous section. Finally, the currents that are not parallel to the modulation direction couple to each other, and will always appear in equal magnitude.

A.3 Exact diagonalisations

A.3.1 State labelling

On a lattice of M sites, with n particles, there are ${}_M C_n$ different Fock states, each corresponding to n out of the M sites being occupied. If the particle number were not fixed, one could just treat the list of occupation numbers as an M-digit binary number. For a fixed number of particles, however, the number of states can be much lower than 2^M. One way to

number these states would be to sort them by occupied sites, such that the state with the first n sites occupied gets label 1, the state with the first $n-1$ sites and site $n+1$ occupied gets label 2, etc. This way, the first $_{M-1}C_{n-1}$ states all have site 1 occupied, and the first $_{M-2}C_{n-2}$ states all have sites 1 and 2 occupied, etc. To obtain a state number from a configuration (a list of occupation numbers), one has to start by numbering all sites, in principle in an arbitrary way. We choose the numbering strategy depicted in fig. A.1, where we start with the leftmost site of the lowest row, move through the row to the right, move one row up, etc. Our basis states can therefore be represented as vectors, with one component for every site. Now there still is a choice to be made concerning relative signs of different states; we resolve this by ordering the creation operators by site number. A 3-particle, 8-site state where the 1st, 4th, and 6th sites are occupied is then defined as

$$|1,0,0,1,0,1,0,0\rangle = c_6^\dagger c_4^\dagger c_1^\dagger |\text{vac}\rangle\,, \tag{A.39a}$$

while

$$c_4^\dagger c_6^\dagger c_1^\dagger |\text{vac}\rangle = -\,|1,0,0,1,0,1,0,0\rangle \tag{A.39b}$$

due to the fermionic anticommutation relation. Having numbered the sites, one has to go through the following algorithm: Start with n at the total number of particles, and m at 1. Then,

- for $i = [1{:}M]$

    – if site i is empty, $m \to m +_{M-i} C_{n-1}$
    – if site i is occupied, $n \to n-1$
    – if $n = 0$, stop

In this algorithm, there are two counters: n runs through all particles, and i through all sites. If the first site is empty, the state is not one of the first $_{M-1}C_{n-1}$, so the state number m is increased by $_{M-1}C_{n-1}$, and the problem is reduced to finding the number of a n-particle state on $M-1$ sites. If the first site is occupied, the state is one of the first $_{M-1}C_{n-1}$,

and the question becomes finding the number of a $(n-1)$-particle state on $M-1$ sites. Thus, going through all sites, one ends up with the number of the state.

To obtain a configuration from a state number, start with n at 1 and m at the state number, and go through the following algorithm:

- for $i = [1{:}M]$

    - if $m >_{M-i} C_{n-1}$, i is empty, $m \to m -_{M-i} C_{n-1}$
    - if $m \leq_{M-i} C_{n-1}$, i is occupied, $n \to n - 1$

Here, per site, the algorithm checks if the number is higher than all states that have that site occupied. If it is, the site is labelled empty, and the problem is reduced to finding the remainder of the state, by subtracting $_{M-i}C_{n-1}$ from the state number. If the state number is not higher than all states that have that site occupied, the site is labelled occupied, and n, the number of particles that still have to be located, is reduced by 1.
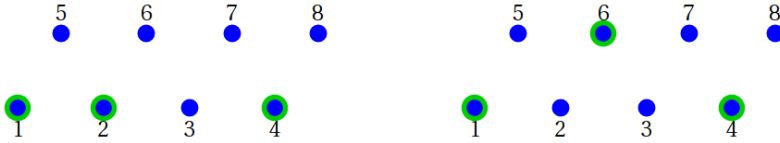

Figure A.1: Left: the 3-particle state with label 2 on a 4×2 lattice; green circled sites are occupied. Right: the 3-particle state with label 13 on the same lattice. The numbering of the sites is indicated in the figure.

A.3.2 Code structure

The following functions are used:

- label2state: takes a state label, system size (total number of sites), and particle number, and returns occupation vector

- state2label: inverts the above operation

- Hmatrix_int: generates the interaction term in the Hamiltonian

- Hmatrix_hop: generates a hopping term, depending on the hopping direction supplied

- int_occ: calculates number of occupied sites between two given sites (see numbering strategy, fig. A.1) - required to determine fermionic minus signs

Hmatrix_int has an easy task: it only contributes to the diagonal of the full Hamiltonian. It runs over all states and calculates the interaction energy associated with each state (using label2state). Hmatrix_hop runs over all states, for each state (using label2state) over all sites, checks if the site is occupied, if so checks if the adjacent site in the hopping direction is empty, and if that is the case too, calculates the label of the new state (with state2label) and the sign of the matrix element (with int_occ). The sign is determined with the help of the ordering convention chosen in Eq. (A.39): for example, the matrix element linking the 8-site, 3-particle state $|1, 0, 0, 1, 0, 1, 0, 0\rangle$ (label 13, fig. A.1, right panel) to $|1, 1, 0, 1, 0, 0, 0, 0\rangle$ (label 2, fig. A.1, left panel) is given by

$$
\begin{aligned}
&\langle 1, 0, 0, 1, 0, 1, 0, 0|\, J_3 c_6^\dagger c_2\, |1, 1, 0, 1, 0, 0, 0, 0\rangle \\
&= J_3 \,\langle \mathrm{vac}|\, c_1 c_4 c_6 c_6^\dagger c_2 c_4^\dagger c_2^\dagger c_1^\dagger\, |\mathrm{vac}\rangle \\
&= - J_3 \,\langle \mathrm{vac}|\, c_1 c_4 c_4^\dagger c_2 c_2^\dagger c_1^\dagger\, |\mathrm{vac}\rangle = -J_3.
\end{aligned} \tag{A.40}
$$

It turns out that the sign of the matrix element is determined by the parity of the number of occupied sites between the two sites connected by the hopping term. In the above example, there is one occupied site between sites 1 and 6 (namely site 4), and therefore the sign is $(-1)^1 = -1$.

The total hopping Hamiltonian is generated by three calls of Hmatrix_hop, one for each principal lattice direction, and then adding these to their transposes. The full Hamiltonian is a sparse matrix, calculated by adding the result of Hmatrix_int, multiplied by the relevant interaction

strength, to the total hopping Hamiltonian. This full Hamiltonian is then fed to `eigs`, the Matlab implementation of the Lanczös algorithm.

Check

The code has been checked for systems where the full Hamiltonian is easy to obtain by hand: small systems, and larger non-interacting ones. First, whether the Hamiltonian that is generated is indeed as it should be. Second, whether the eigenstates corresponding to those Hamiltonians are indeed as they should be: their decomposition in configuration-space Fock states, their energies (which, in the non-interacting case, can be calculated easily in momentum space). All checks returned satisfactory results.

A.3.3 Small-system states with absolute minimal energy

In a system of 2 particles on a 4×2 lattice with periodic boundary conditions, there are 8 real-space basis states that completely avoid interaction energy. They are listed in table A.1.

$\lvert 2 \rangle = \lvert 1, 0, 1, 0, 0, 0, 0, 0 \rangle$	$\lvert 9 \rangle = \lvert 0, 1, 0, 1, 0, 0, 0, 0 \rangle$
$\lvert 6 \rangle = \lvert 1, 0, 0, 0, 0, 0, 1, 0 \rangle$	$\lvert 13 \rangle = \lvert 0, 1, 0, 0, 0, 0, 0, 1 \rangle$
$\lvert 15 \rangle = \lvert 0, 0, 1, 0, 1, 0, 0, 0 \rangle$	$\lvert 20 \rangle = \lvert 0, 0, 0, 1, 0, 1, 0, 0 \rangle$
$\lvert 24 \rangle = \lvert 0, 0, 0, 0, 1, 0, 1, 0 \rangle$	$\lvert 27 \rangle = \lvert 0, 0, 0, 0, 0, 0, 1, 0, 1 \rangle$

Table A.1: The 8 2-particle states in a 4×2 lattice with periodic boundary conditions that avoid all interaction energy, expressed in the real-space basis introduced in section A.3.1.

It turns out that the states $\lvert 2 \rangle - \lvert 6 \rangle + \lvert 15 \rangle + \lvert 24 \rangle$ and $\lvert 9 \rangle - \lvert 13 \rangle + \lvert 20 \rangle + \lvert 27 \rangle$, which are both completely built up out of states that have zero interaction energy, also minimise the kinetic terms. The fact that states with higher kinetic energy are not mixed into these states even at finite interactions originates in the degeneracy of lowest-energy kinetic eigenstates, as well as the fact that all of those states lie on the Fermi surface, as shown in fig. A.2.
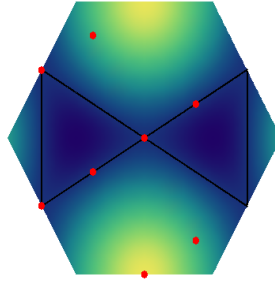
Figure A.2: The allowed quasimomenta and the bowtie-shaped Fermi surface for the 4×2 lattice.

Acknowledgements

Although only one name appears on the cover of this thesis, there were many people who, directly or indirectly, contributed to its present existence. Here, I would like to take the opportunity to thank them:

My thesis advisors, Maciej Lewenstein and André Eckardt, for their advice and support, fruitful collaboration, the invitation to come to Barcelona, and providing me with an academic home.

Achilleas Lazarides, my mentor from Utrecht, for his refreshingly cynical comments, continued encouragement to not give up on physics, and inspiration to be a good researcher. I am looking forward to our continued collaboration!

My collaborators Om, Philipp, Alessio, and Marco, for pleasant collaborations and discussions, on physics and other themes.

My office mates from Utrecht and Barcelona, Jasper, Samo, Luca, Marcelo, Ulrich, and Jordi, for making the whole process a much more enjoyable experience. Jordi, for the Spanish translation of the abstract.

The place of honour on this list, the last one, is reserved for my beloved wife, Katja. Her support was more essential than any other, she helped me find the motivation and energy to continue.

Bibliography

[1] I. Bloch, J. Dalibard, and W. Zwerger, Rev. Mod. Phys. **80**, 885 (2008).

[2] M. Lewenstein, A. Sanpera, and V. Ahufinger, *Ultracold Atoms in Optical Lattices: Simulating quantum many-body systems* (Oxford University Press, Oxford, United Kingdom, 2012).

[3] M. H. Anderson, J. R. Ensher, M. R. Matthews, C. E. Wieman, and E. A. Cornell, Science **269**, 198 (1995).

[4] C.C. Bradley, C.A. Sackett, J.J. Tollett, and R.G. Hulet, Phys. Rev. Lett. **75**, 1687 (1995).

[5] K.B. Davis, M.-O. Mewes, M.R. Andrews, N.J. van Druten, D.S. Durfee, D.M. Kurn, and W. Ketterle, Phys. Rev. Lett. **75**, 3969 (1995).

[6] B. DeMarco and D.D. Jin, Science **285**, 1703 (1999).

[7] M. Greiner, Ph.D. thesis, Ludwig Maximilian University of Munich, 2003.

[8] M. Greiner, O. Mandel, T. Esslinger, T.W. Hänsch, and I. Bloch, Nature **415**, 39 (2002).

[9] P. Soltan-Panahi, J. Struck, P. Hauke, A. Bick, W. Plenkers, G. Meineke, C. Becker, P. Windpassinger, M. Lewenstein, and K. Sengstock, Nature Physics **7**, 434 (2011).

[10] J. Struck, C. Ölschläger, R. Le Targat, P. Soltan-Panahi, A. Eckardt, M. Lewenstein, P. Windpassinger, and K. Sengstock, Science **425**, 996 (2011).

[11] G.-B. Jo, J. Guzman, C.K. Thomas, P. Hosur, A. Vishwanath, and D.M. Stamper-Kurn, Phys. Rev. Lett. **108**, 045305 (2012).

[12] J.F.S. Brachmann, W.S. Bakr, J. Gillen, A. Peng, and M. Greiner, arXiv:1102.3373.

[13] E. Arimondo, D. Ciampini, A. Eckardt, M. Holthaus, and O. Morsch, arXiv:1203.1259.

[14] A. Eckardt, P. Hauke, P. Soltan-Panahi, C. Becker, K. Sengstock, and M. Lewenstein, EPL **89**, 10010 (2010).

[15] A. Hemmerich and C. Morais Smith, Phys. Rev. Lett **99**, 113002 (2007).

[16] P. Hauke, O. Tieleman, A. Celi, C. Ölschläger, J. Simonet, J. Struck, M. Weinberg, P. Windpassinger, K. Sengstock, M. Lewenstein, and A. Eckardt, arXiv:1205.1398.

[17] A. Eckardt, C. Weiss, and M. Holthaus, Phys. Rev. Lett. **95**, 260404 (2005).

[18] A. Hemmerich, Phys. Rev. A **81**, 063626 (2010).

[19] H. Lignier, C. Sias, D. Ciampini, Y. Singh, A. Zenesini, O. Morsch, and E. Arimondo, Phys. Rev. Lett. **99**, 220403 (2007).

[20] J. H. Shirley, Phys. Rev. **138**, B979 (1965).

[21] H. Sambe, Phys. Rev. A **7**, 2203 (1973).

[22] K. Drese and M. Holthaus, Phys. Rev. Lett. **78**, 29322935 (1997).

[23] M. P. A. Fisher, P. B. Weichman, G. Grinstein, and D. S. Fisher, Phys. Rev. B **40**, 546 (1989).

[24] D. van Oosten, P. van der Straten, and H. T. C. Stoof, Phys. Rev. A **63**, 0536601 (2001).

[25] A. Zenesini, H. Lignier, D. Ciampini, O. Morsch, and E. Arimondo, Phys. Rev. Lett **102**, 100403 (2009).

[26] A. Eckardt, M. Holthaus, H. Lignier, A. Zenesini, D. Ciampini, O. Morsch, and E. Arimondo, Phys. Rev. A **79**, 013611 (2009).

[27] A. Eckardt and M. Holthaus, EPL **80**, 550004 (2007).

[28] M. di Liberto, O. Tieleman, V. Branchina, and C. Morais Smith, Phys. Rev. A **84**, 013607 (2011).

[29] Lih-King Lim, C. Morais Smith, and A. Hemmerich, Phys. Rev. Lett. **100**, 130402 (2008).

[30] Lih-King Lim, A. Hemmerich, and C. Morais Smith, Phys. Rev. A **81**, 023404 (2010).

[31] J. Struck, C. Ölschläger, M. Weinberg, P. Hauke, J. Simonet, A. Eckardt, M. Lewenstein, K. Sengstock, and P. Windpassinger, Phys. Rev. Lett. **108**, 225304 (2012).

[32] T. Lahaye, C. Menotti, L. Santos, M. Lewenstein, and T. Pfau, Rep. Prog. Phys. **72**, 126401 (2009).

[33] C. Trefzger, C. Menotti, B. Capogrosso-Sansone, and M. Lewenstein, J. Phys. B **44**, 193001 (2011).

[34] M. Lu, N.Q. Burdick, and B.L. Lev, arXiv:1202:4444.

[35] K. K. Ni, S. Ospelkaus, D. Wang, G. Quemener, B. Neyenhuis, M. H. G. de Miranda, J. L. Bohn, J. Ye, and D. S. Jin, Nature **464**, 13241328 (2010).

[36] T. Pohl, H.R. Sadeghpour, and P. Schmelcher, Phys. Rep. **484**, 181 (2009).

[37] A. Eckardt and M. Lewenstein, Phys. Rev. A **82**, 011606(R) (2010).

[38] M.J. Bijlsma, B.A. Heringa, and H.T.C. Stoof, Phys. Rev. A **61**, 053601 (2000).

[39] Lih-King Lim, A. Lazarides, A. Hemmerich, and C. Morais Smith, Phys. Rev. A **82**, 013616 (2010).

[40] A. Lazarides, O. Tieleman, and C. Morais Smith, Phys. Rev. A **84**, 023620 (2011).

[41] T. Sowiński, O. Dutta, P. Hauke, L. Tagliacozzo, and M. Lewenstein, Phys. Rev. Lett. **108**, 115301 (2012).

[42] O. Dutta, T. Sówinski, and M. Lewenstein, arXiv:1202:4158.

[43] B. Capogrosso-Sansone, C. Trefzger, M. Lewenstein, and and G. Pupillo P. Zoller, Phys. Rev. Lett. **104**, 125301 (2010).

[44] G.V. Chester, Phys. Rev. A **2**, 256 (1970).

[45] A. Griesmayer, J. Werner, S. Hensler, J. Stuhler, and T. Pfau, Phys. Rev. Lett. **94**, 160401 (2005).

[46] M. Lu, N.Q. Burdick, S.H. Youn, and B.L. Lev, Phys. Rev. Lett. **107**, 190401 (2011).

[47] J.G. Danzl, M.J. Mark, E. Haller, M. Gustavsson, R. Hart, J. Aldegunde, J.M. Hutson, and H.-C. Nägerl, Nature Physics **6**, 265 (2010).

[48] J.G. Danzl, E. Haller, M. Gustavsson, M.J. Mark, R. Hart, N. Bouloufa, O. Dulieu, H. Ritsch, and H.-C. Nägerl, Science **321**, 1026 (2008).

[49] S. Müller, J. Billy, E.A.L. Henn, H. Kadau, A. Griesmaier, M. Jona-Lasinio, L. Santos, and T. Pfau, Phys. Rev. A **84**, 053601 (2011).

[50] B. Pasquiou, G. Bismut, E. Maréchal, P. Pedri, L. Vernac, O. Gorceix, and B. Laburthe-Tolra, Phys. Rev. Lett. **106**, 015301 (2011).

[51] M. Fattori, G. Roati, B. Deissler, C. D'Errico, M. Zaccanti, M. Jona-Lasinio, L. Santos, M. Inguscio, and G. Modugno, Phys. Rev. Lett. **101**, 190405 (2008).

[52] A. Maluckov, G. Gligorić, L. Hadžievski, B.A. Malomed, and T. Pfau, Phys. Rev. Lett. **108**, 140402 (2012).

[53] K. Günter, T. Stöferle, H. Moritz, M. Köhl, and T. Esslinger, Phys. Rev. Lett. **96**, 180402 (2006).

[54] S. Ospelkaus, C. Ospelkaus, O. Wille, M. Succo, P. Ernst, K. Sengstock, and K. Bongs, Phys. Rev. Lett. **96**, 180403 (2006).

[55] K. Góral, L. Santos, and M. Lewenstein, Phys. Rev. Lett. **88**, 170406 (2002).

[56] I. Danshita and C.A.R. Sá de Melo, Phys. Rev. Lett. **103**, 225301 (2009).

[57] O. Tieleman, A. Lazarides, and C. Morais Smith, Phys. Rev. A **83**, 013627 (2011).

[58] L. He and W. Hofstetter, Phys. Rev. A **83**, 053629 (2011).

[59] C. Trefzger, C. Menotti, and M. Lewenstein, Phys. Rev. Lett. **103**, 035304 (2009).

[60] P.P. Orth, D.L. Bergman, and K. Le Hur, Phys. Rev. A **80**, 023624 (2009).

[61] O. Tieleman, O. Dutta, M. Lewenstein, and A. Eckardt, arXiv:1210.4338.

[62] E. Haller, R. Hart, M.J. Mark, J.G. Danzl, L. Reichsllner, M. Gustavsson, M. Dalmonte, G. Pupillo, and H.-C. Nägerl, Nature **466**, 597 (2010).

[63] F.D.M. Haldane, Phys. Rev. Lett. **47**, 1840 (1981).

[64] H.-P. Büchler, J.W. Blatter, and W. Zwerger, Phys. Rev. Lett. **90**, 130401 (2003).

[65] V.L. Pokrovsky and A.L. Talapov, Phys. Rev. Lett. **42**, 65 (1979).

[66] J.K. Perring and T.H.R. Skyrme, Nuclear Physics **31**, 550 (1962).

[67] D. Jaksch, C. Bruder, J. I. Cirac, C. W. Gardiner, and P. Zoller, Phys. Rev. Lett. **81**, 3108 (1998).

[68] K. Le Hur and T.M. Rice, Annals of Physics **324**, 1452 (2009).

[69] I. B. Spielman, W. D. Phillips, and J. V. Porto, Phys. Rev. Lett. **98**, 080404 (2007).

[70] T. Stöferle, H. Moritz, M. Köhl, and T. Esslinger, Phys. Rev. Lett. **92**, 130403 (2004).

[71] W. Kohn, Phys. Rev. **115**, 809 (1959).

[72] G. Floquet, Ann. de l'École Normale Supérieure **12**, 47 (1883).

[73] M. Grifoni and P. Hänggi, Phys. Rep. **304**, 229 (1998).

[74] A. Eckardt and M. Holthaus, Phys. Rev. Lett. **101**, 245302 (2008).

[75] P. Fulde and R. A. Ferrell, Phys. Rev. **135**, A550 (1964).

[76] A. J. Larkin and Y. N. Ovchinnikov, JETP **20**, 762 (1965).

[77] A. Bianchi, R. Movshovich, C. Capan, P. G. Pagliuso, and J. L. Sarrao, Phys. Rev. Lett. **91**, 187004 (2003).

[78] H. A. Radovan, N. A. Fortune, T. P. Murphy, S. T. Hannahs, E. C. Palm, S. W. Tozer, and D. Hall, Nature **425**, 51 (2003).

[79] M. Kenzelmann, Th. Strässle, C. Niedermayer, M. Sigrist, B. Padmanabhan, M. Zolliker, A. D. Bianchi, R. Movshovich, E. D. Bauer, J. L. Sarrao, and J. D. Thompson, Science **321**, 1652 (2008).

[80] K. Kumagai, H. Shishido, T. Shibauchi, and Y. Matsuda, Phys. Rev. Lett. **106**, 137004 (2011).

[81] Y. Liao, A. S. C. Rittner, T. Paprotta, W. Li, G. B. Partridge, R. G. Hulet, and S. K. Baur, Nature **467**, 567 (2010).

[82] V. Branchina, H. Mohrbach, and J. Polonyi, Phys. Rev. D **60**, 045006 (1999).

[83] Y.-J. Lin, Jiménez-Garcia, and I. B. Spielman, Nature **471**, 83 (2011).

[84] D. van Oosten, Ph.D. thesis, Utrecht University, 2004.

[85] S. Vogt, Master's thesis, Hamburg University, 2009.

[86] N. Marzari and D. Vanderbilt, Phys. Rev. B **56**, 12847 (1997).

[87] T. D. Stanescu, B. Anderson and V. Galitski, Phys. Rev. A **78**, 023616 (2008).

[88] E. Arimondo, personal communication.

[89] E. Kim and M.H.W. Chan, Science **305**, 1941 (2004).

[90] N. Prokof'ev, Adv. Phys. **56**, 381 (2007).

[91] G. Möller and N.R. Cooper, Phys. Rev. Lett. **99**, 190409 (2007).

[92] A. Sen, P. Dutt, K. Damle, and R. Moessner, Phys. Rev. Lett. **100**, 147204 (2008).

[93] L. Pollet, J. D. Picon, H. P. Büchler, and M. Troyer, Phys. Rev. Lett. **104**, 125302 (2010).

[94] K.P. Schmidt, J. Dorier, A.M. Läuchli, and F. Mila, Phys. Rev. Lett. **100**, 090401 (2008).

[95] N.R. Cooper, Adv. Phys. **57**, 539 (2008).

[96] Y. Lin, R. L. Compton, K. J. Garcia, J. V. Porto, and I. B. Spielman, Nature **462**, 628 (2009).

[97] G. Juzeliunas, J. Ruseckas, P. Öhberg, and M. Fleischhauer, Phys. Rev. A **73**, 025602 (2006).

[98] C. Kittel, *Introduction to solid state physics, 7th ed.* (Wiley & Sons, Inc., New Jersey, 1996).

[99] B. Paredes, A. Widera, V. Murg, O. Mandel, S. Fölling, J.I. Cirac, G.V. Shlyapnikov, T.W. Hänsch, and I. Bloch, Nature **429**, 277 (2004).

[100] T. Giamarchi, *Quantum Physics in One Dimension* (Clarendon Press, Oxford, United Kingdom, 2003).

[101] R. Rajaraman, *Solitons and Instantons* (Elsevier North-Holland, Amsterdam, 1982).

[102] B. Sutherland, *Beautiful models* (World Scientific, Singapore, 2004).

[103] P. Sengupta, L. P. Pryadko, F. Alet, M. Troyer, and G. Schmid, Phys. Rev. Lett. **94**, 207202 (2005).

[104] L. Mathey, I. Danshita, and C. W. Clark, Phys. Rev. A **79**, 011602 (2009).

[105] A. Lazarides, O. Tieleman, and C. Morais Smith, Phys. Rev. B **80**, 245418 (2009).

[106] N. Read, Phys. Rev. B **52**, 1926 (1995).

[107] E. Papa and A. Tsvelik, Phys. Rev. B **66**, 155304 (2002).

[108] S. Park, K. Moon, C. Ahn, J. Yeo, C. Rim, and B. Lee, Phys. Rev. B **66**, 153318 (2002).

[109] C. B. Hanna, A.H. MacDonald, and S. M. Girvin, Phys. Rev. B **63**, 125305 (2001).

[110] O. Tieleman, A. Lazarides, D. Makogon, and C. Morais Smith, Phys. Rev. B **80**, 205315 (2009).

[111] A. B. Zamolodchikov, Int. J. Mod. Phys **10**, 1125 (1995).

[112] D. M. Ceperley, Rev. Mod. Phys. **67**, 279 (1995).

[113] R. P. Feynman and A. R. Hibbs, *Quantum Mechanics and Path Integrals* (McGraw-Hill, New York, 1965).

[114] A. Lazarides, unpublished.

[115] F. J. Wegner and A. Houghton, Phys. Rev. A **8**, 402 (1972).

[116] R. Lipowsky and M. E. Fisher, Phys. Rev. B **36**, 2126 (1987).

[117] G.E. Astrakharchik, D.M. Gangardt, Yu.E. Lozovik, and I.A. Sorokin, Phys. Rev. E **74**, 021105 (2006).

[118] M. A. Cazalilla, J. Phys. B **37**, S1 (2004).

[119] T. Gericke, P. Wuertz, D. Reitz, T. Langen, and H. Ott, Nature Physics **4**, 949 (2008).

[120] W. S. Bakr, A. Peng, M. E. Tai, R. Ma, J. Simon, J. I. Gillen, S. Flling, L. Pollet, and M. Greiner, Science **329**, 547 (2010).

[121] N. Gemelke, X. Zhang, C.-L. Hung, and C. Chin, Nature **460**, 995 (2009).

[122] C.-H. Wu, J.W. Park, P. Ahmadi, S. Will, and M.W. Zwierlein, Phys. Rev. Lett. **109**, 085301 (2012).

[123] W.S. Bakr, P.M. Preiss, M.E. Tai, R. Ma, J. Simon, and M. Greiner, Nature **480**, 500 (2011).

[124] R. Sachdeva and S. Ghosh, Phys. Rev. A **85**, 013642 (2012).

[125] H. T. C. Stoof, K. B. Gubbels, and D. B. M. Dickerscheid, *Utracold Quantum Fields* (Springer, Dordrecht, 2009).